Energy Relaxation and Hot-electron Lifetimes in Single Nanocrystals

A Thesis
Presented to
The Academic Faculty

by

Sameh Dardona

In Partial Fulfillment
of the Requirements for the Degree
Doctor of Philosophy

School of Physics
Georgia Institute of Technology
August 2006

Energy Relaxation and Hot-electron Lifetimes in Single Nanocrystals

Approved by:

Dr. Phillip First, Advisor
School of Physics
Georgia Institute of Technology

Dr. Mostafa El-Sayed
School of Chemistry and Biochemistry
Georgia Institute of Technology

Dr. Edward Conrad
School of Physics
Georgia Institute of Technology

Dr. Alexei Marchenkov
School of Physics
Georgia Institute of Technology

Dr. Walt A. De Heer
School of Physics
Georgia Institute of Technology

Date Approved June 27, 2006

To my parents : Ibrahim and Fatmeh

ACKNOWLEDGEMENTS

There are many people without whose technical and personal help and support, this work would never have been accomplished. I would like to thank my advisor, Dr. Phillip First, for granting me the great opportunity of working in his lab. I thank him for his enthusiasm and guidance throughout this work. Thanks to my committee members, Dr's. Conrad, Marchenkov, El-Sayed, and De Heer for their careful reading and constructive comments.

There are many Chemists on our campus who have continuously supplied samples during my studies, whether included in the dissertation or not. These include Ryan Price, Alex Chil, and Qusai Darquar. I have enjoyed collaborating and working with them. The service and technical support of the College of Science machine shop staff are appreciated. They were essential in rebuilding and revising some of the low temperature STM designs. I would like to thank my fellow research group Jianfei Shao, Tianbo Li, Greg Rutter, Joanna Hass, Nikhil Sharma, and Asmerom Ogbazghi. I have had great time working with them. Many thanks to Judy Melton for her careful reading of this manuscript.

Finally, I thank my family for their love and patience throughout my graduate school time. Without their love this work would not have been accomplished.

Sameh I. Dardona

Georgia Institute of Technology

July 2006

TABLE OF CONTENTS

LIST OF TABLES

LIST OF FIGURES

SUMMARY

Understanding changes in materials properties as a function of size is crucial for both fundamental science development and technological applications. Size restriction results in quantum confinement effects that modify both energy level structures and electron dynamics of solid materials. This study investigates individual quantum states in a single nanocrystal. Single electron charging effects in gold and semiconductor nanocrystals are observed. Charging effects are found to be dominant in samples, where the nanocrystals are weakly coupled to the substrate. For nanocrystals strongly coupled to the substrate, nanocrystal-substrate tunneling rate is larger than tip-nanocrystal tunneling rate. Therefore, the resulting peaks in the dI/dV spectrum are attributed to tunneling through the energy levels of the nanocrystal.

A newly developed nanocrystals BEES technique is used successfully to further explore quantized energy levels and electron dynamics in single gold nanocrystals. BEES samples were grown successfully by depositing 10 nm thick gold on silicon substrates. Nanocrystals are chemically attached to the gold substrate using a self assembled monolayer (SAM) of xyelendithiol molecules. Immobile and single isolated nanocrystals were imaged at low temperature. A BEES turn-on voltage of 0.84 V was found on nanocrystal-free region of the substrate. The BEES spectrum acquired on a single gold nanocrystal is found to be attenuated by a factor of 10 when compared with BEES acquired on the substrate. The attenuation is attributed to electron relaxation to lower energy states before tunneling out of the nanocrystal. The measured hot electron lifetimes from experimental data were found to be on the order of 16 picoseconds, which is a long time compared to lifetimes in bulk metals or large nanocrystals. The long measured lifetimes result from the molecular-like energy level structures of these small nanocrystals.

CHAPTER I

INTRODUCTION

The understanding of matter in its condensed phase results in great technological and scientific advancements. In recent years, the properties of solid materials were found to depend significantly on their size as well as their geometry. In a typical molecular solid, the intermolecular interactions are much weaker than the intermolecular bonding, so the properties of a molecular solid can be described by the sum of individual molecular contributions with small perturbations from the intermolecular forces. Such weak interaction does not extend beyond the nearest neighbor, therefore, the electronic properties of a molecular crystal are usually independent of the crystal's size. For a semiconductor crystal, electronic excitations involve a weakly bound electron-hole pair, usually localized over a length much longer than the lattice constant. As the size of the semiconductor crystal approaches this exciton Bohr diameter, both the wavefunctions of electrons and holes become confined, and the electronic properties are modified as a result. This is known as the quantum size effect, which can be observed as a blue shift in the energy bandgap and as quantization in the energy level structure [3]. It is therefore possible to tune the materials properties by slightly changing their size.

In metals, the Bohr radius is smaller than that of a semiconductor, therefore, quantum size effects appear at smaller sizes. Upon reducing metal sizes, its absorption spectra is characterized by a strong broad absorption that is absent in bulk metal. This dipole (surface plasmon) band is ascribed to a collective oscillation of the conduction electrons in response to optical excitation [4]. Further reduction of gold sizes leads to a structured absorption spectrum with a distinct absorption onset near 1.31 eV corresponding to an electronic gap between the Highest Occupied Molecular Orbital (HOMO) and the Lowest Unoccupied Molecular Orbital (LUMO) [5].

One fundamental feature of quantum effects is that the energy spectrum of a system

of particles confined to a small region is discrete or quantized with the typical spacing between energy levels increasing with decreasing system size. Such discrete spectra have for long time been a source of information about the particles forces and correlations in atomic and nuclear physics. In solid state physics, however, it has been very difficult to study the discrete spectrum of an individual sample. This difficulty is because system sizes were very large and the discrete energies could not be resolved on the energy scale determined by the temperature. This limitation had changed in the last decade due to the advances in fabrication and characterization techniques, which made it possible to fabricate and study systems of nanometer dimensions. Semiconductor devices have been used to fabricate the first quantum dot, i.e., droplets of charge confined to a very small (radius of order 50 nm) two-dimensional region. That region was small enough for the discrete levels in the conduction electron spectrum was resolved at 100 mK temperature [6, 7]. The technique used to resolve these levels is called *single electron tunneling spectroscopy*: the dot is connected to two leads through electrostatic tunnel barriers, and the current-voltage characteristics of the dot shows well-defined resonances, which are associated with tunneling through discrete states on the quantum dot.

Although tunneling spectroscopy studies of metallic nanocrystals are similar to those of semiconductor quantum dots, there are two important differences. First, metals have much higher density of states than semiconductors, hence metals require much smaller sample sizes (< 10 nm) before experimental resolution of discrete levels. Second, metal nanocrystals have much larger charging energies than quantum dots.

Recently, developed self-assembly methods for synthesizing nanometer-size structures offers an alternative to lithographic methods that are complex, costly, and resolution limited. The production of size-selected and ligand-stabilized metal and semiconductor nanocrystals using self-assembly methods is becoming common and practical. Techniques for using self-assembled nanocrystals as precursors for further self-assembly into complex and superstructures are under development [8]. The present work is aimed at investigating self-assembled Au nanocrystals with different sizes by Scanning Tunneling Spectroscopy(STS) and Ballistic Electron Emission Spectroscopy(BEES).

Nanocrystals are novel materials that have sizes slightly larger than typical organometallic molecules and smaller than the bulk solid state, with the unique feature that their properties are controlled by size and shape [9, 10]. Nanocrystals 2-20 nm in diameter contain hundreds to thousands of atoms. Moreover, because of their very small size, the charging energy associated with addition or removal of a single electron is very large and is manifested in the Single Electron Tunneling (SET) effect [10, 11, 12]. This change of properties provides a rich ground for basic scientific research that has attracted and continues to attract considerable attention. Nanocrystals are expected to play a major role in the new emerging field of nanotechnology in applications ranging from lasers and other optoelectronic devices to biological fluorescence marking. The realization of nanocrystals in these and other applications requires a thorough understanding of size-dependent electronic structure at the level of single quantum state and a basic knowledge of the dynamics of electronic excitations within a single nanocrystal.

1.1 Research Motivations

The advancement in the synthesis of size-selected nanocrystals samples using self-assembly methods has made it possible to study the property as a function of size. These nanocrystals have well-defined and stable structures. They are important in basic research since their sizes are between molecular systems and extended solids. Nanocrystals have the potential of being used in the construction of single electron transistors, switches, and sensors [9]. The realization of these applications requires rigorous understanding of the single nanocrystals properties as well as the manipulation of the single nanocrystal. Therefore, new characterization and manipulation techniques need to be developed.

Most of the current spectroscopic measurements are performed on ensemble of nanocrystals. Combined frequency- and time-resolved optical methods are extensively used to study both energy level structures and hot electron dynamics in nanocrystals. However, optical studies are usually performed on ensembles of nanocrystals, where size distributions and solvent impurities significantly affect the data interpretation. Moreover, optical measurements can only probe the dipole-allowed electronic transitions.

Scanning Tunneling Spectroscopy (STS) based techniques are powerful for studying energy level structures in single nanocrystals. STS is a complement to frequency-resolved optical methods and it has enabled for the resolution of single energy level. However, information about the electron dynamics in STS studies is limited. Time-resolve measurements on ensembles of nanocrystals is the only source of information about the electron dynamics. Given these limitations on the currently used techniques, new methods that combine both single nanocrystal addressability as well as electron dynamics investigations need to be developed for better understanding of the size-dependent properties in both metals and semiconductors. The developed techniques will complement time-resolved optical methods and will allow the investigation of energy loss mechanisms and the measurements of hot-electron lifetimes in single nanocrystals.

1.2 Research Objectives

The objectives of the proposed research are the development and implementation of Scanning Tunneling Spectroscopy (STS) related techniques in order to provide an understanding of the size-dependent electronic structure at the level of single quantum states and a basic knowledge of the dynamics of electron excitation within a single nanocrystal. Techniques used include conventional Scanning Tunneling Microscopy and Spectroscopy (STM/S) and Ballistic Electron Emission Spectroscopy (BEES). STM has been used to characterize nanocrystal samples of different sizes and shapes. Tunneling imaging is performed at different temperatures and in different environments. The environment is usually determined by nanocrystals coupling to the substrate and the STM tip. Since the measured height in STM-based imaging represents the actual nanocrystals sizes, STM height measurements are essential for correlating actual nanocrystals sizes with spectroscopic data.

STS measurements are charge addition spectroscopies. Therefore, a detailed understanding of STS spectra requires new methodologies in both the STS measurements and the sample preparation. The number of charges on a nanocrystal depend on the ratio between the tunneling-in (tip to nanocrystal for a negative tip-sample bias voltage) and tunneling-out (nanocrystal to substrate at negative bias) rates. This implies that classical

charging effects and density of states features are entangled in the STS spectra. Therefore, for energy level identification, the Coulomb charging effects should be disentangled from the one-electron density of states. Since density of states features remain constant in energy for weakly coupled tunnel barriers, the disentanglement can be performed by acquiring STS spectra at different coupling conditions of nanocrystals to the surrounding environment, that is, at different tip-nanocrystal separations and different nanocrystal-substrate coupling configurations.

Hot electron dynamics in single nanocrystals is another important theme of the proposed research. To address this issue, the BEES system, a three terminal extension to STM and STS, will be used to measure the fraction of injected electrons that are transmitted through a single nanocrystal. BEES studies of nanocrystals have two key features that are not available in other spectroscopic techniques. First, BEES current directly measures the outgoing electron current from the nanocrystal. Second, the Schottky barrier at the metal/semiconductor interface in BEES substrate provides a fixed energy reference and an energy filter for hot electrons injected into the nanocrystal. The transmitted BEES current is expected to be enhanced when the tunnel injection energy coincides with a quantum state of the nanocrystal, and it will decrease substantially when an inelastic event becomes energetically allowed within the nanocrystal.

Ultimately, BEES spectra would provide information about lifetimes and decay channels of the excited electronic states in nanocrystals. This information is perfectly complementary to STS studies and to other frequency- and time-resolved optical spectroscopies of both semiconductor and metal nanocrystals ensembles in solution and in thin films.

1.3 Thesis Overview

The thesis is divided into six chapters. The first chapter includes introductory concepts about nanoscale phenomena in metals and semiconductors with special focus on nanocrystals. It also highlights some of the main discoveries in the field and the technological applications of nanocrystals. Chapter two briefly introduces the basic principles of STM

system. It also includes some of the new design modifications introduced to our microscope for BEES measurement capabilities and demonstrates atomic resolution imaging of the microscope. The chapter ends with a detailed description of our nanocrystal sample preparation and STM imaging.

Chapter three focuses on STS of single nanocrystals. The basic concepts of tunneling spectroscopy of a single nanocrystal are introduced. A theoretical approach for the calculation of the tunneling rates and hence the current through a double-barrier tunneling junction is introduced. Experimental conditions for resolving energy levels are discussed. Experimental data for tunneling through the discrete energy levels of 8 kDa nanocrystals are shown in this chapter, as well as the effect of the tunneling junction parameters on the dI/dV peaks.

Chapter four presents BEES measurements on single nanocrystals. It starts with a brief introduction of BEES theory. Some of the experimental design considerations for BEES measurements are detailed in this chapter. These considerations include sample fabrication, sample holder design, microscope wiring, and noise reduction. BEES studies of hot electron dynamics and their interpretation are presented.

The fifth chapter includes a summary of the optical properties of nanocrystals. It introduces some of the optical measurement techniques currently used in studying nanocrystals. The results of some of those studies are summarized and compared with our STS and BEES measurements. Finally, chapter six summarizes the results and conclusions of this research. The chapter also contains a plan for future work.

CHAPTER II

TUNNELING MICROSCOPY OF NANOCRYSTALS

2.1 STM Principle of Operation

The scanning tunneling microscope was invented by Binnig and Rohrer [13] and is based on the quantum mechanical phenomenon of electron tunneling. There are five scientific and technical processes or concepts that the STM system integrates to make atomic resolution images of a surface possible. Each of these processes was used in other scientific areas before the invention of the STM system. These processes are:

- The principle of quantum mechanical tunneling,
- Achievement of controlled motion over small distances using piezoelectric elements,
- The principle of negative feedback,
- Acoustic vibration isolation,
- Electronic data acquisition.

2.1.1 Quantum Mechanical Tunneling

The concept of electron tunneling phenomenon will be detailed since it is the most fundamemental that allows the microscope to operate. The operating principle of STM is shown in Figure 1(a). A sharp conducting tip is brought into close proximity to a metallic surface. When a bias voltage is applied between tip and surface, electrons have a finite probability to tunnel through the vacuum barrier. The direction of the electron flow depends on the sign of applied voltage. The probability that electrons can be found on the surface, which is not physically contacting the tip, is a consequence of the wavelike behavior of electrons. In tunneling processes, electrons are pictured as a cloud of charges. The size of the cloud is related to the wavelength of the electron (a few angstroms). When electrons collide with

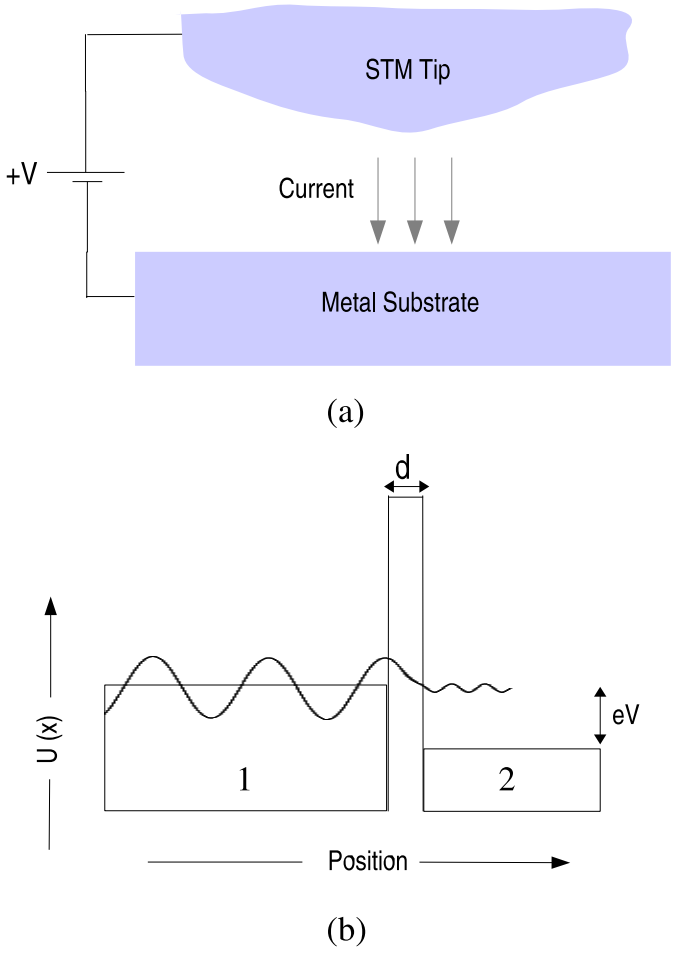

Figure 1: Schematic of STM operation: (a) When a sharp metal tip is brought very close to a conducting substrate, electrons will tunnel with a finite probability to the substrate. (b) Energy diagram of the tunneling process. When bias voltage is applied between (1) and (2), Fermi levels get shifted and electrons move from the higher to the lower energy side

the barrier, their wavefunctions extend into the vacuum region. If the vacuum barrier is thick, electrons will be reflected back. For thin barriers, however, electrons wavefunctions will extend to the other side and electrons will appear on the metal surface, as shown schematically in Figure 1(b). The tunneling process in STM system can be described by solving Shroedinger's equation. The one-dimensional steady-state Schroedinger equation is given by:

$$\frac{\hbar^2}{2m}\frac{\partial^2\psi}{\partial x^2} + U(x)\psi(x) = E\psi(x), \tag{1}$$

where *U(x)* is the potential energy of the electron which will assumed to be a constant U_0 in the barrier and zero outside. E is the kinetic energy of the electron. The general solution

of the above equation in regions 1 and 2 of Figure 1(b) is given by:

$$\psi_1(x) = Ae^{-ikx} + Be^{ikx}, \qquad k = \sqrt{\frac{2mE}{\hbar^2}} \tag{2}$$

$$\psi_1(x) = Ee^{-ikx} + Fe^{ikx}. \tag{3}$$

And in the barrier region, the solution is given as:

$$\psi_1(x) = Ce^{-\mu x} + De^{\mu x}, \qquad \mu = \sqrt{\frac{2m(U_0 - E)}{\hbar^2}}. \tag{4}$$

At very small separation between metal 1 and metal 2 in Figure 1(b), electron wavefunction and its first derivative must be continuous at the boundaries between tip-barrier and barrier-sample in order to conserve energy and mass. For a coordinate system with $x = 0$ at metal 1 and $x = d$ at metal 2, the boundary conditions for continuity result in:

$$A + B = C \qquad\qquad ik(A - B) = -\mu C \tag{5}$$

$$Ce^{-\mu d} + De^{\mu d} = Fe^{ikd} \qquad\qquad \mu Ce^{-\mu d} + \mu De^{\mu d} = ikFe^{ikd}. \tag{6}$$

The probability of finding an electron in the barrier region due to quantum tunneling is given by:

$$|\frac{C}{A}|^2 = \frac{4(k\delta)^2}{1 + (k\delta)^2}, \tag{7}$$

where $\delta = 1/\mu$. The effective electron tunneling transmission coefficient can be found by combining Equation 7 with the boundary conditions at $x = d$ in Equation 6.

$$T(E) \approx |\frac{F}{A}|^2 \approx \left[\frac{4k\delta}{1 + (k\delta)^2}\right]^2 e^{\frac{-2d}{\delta}} \propto e^{-d\sqrt{2m\Phi/\hbar}}, \tag{8}$$

where $k^2 = \frac{2mE}{\hbar^2}$ *and* $(k\delta)^2 = \frac{E}{(U_0 - E)} = \frac{E}{\Phi}$.

Substituting typical values of $\Phi = 5 \times 10^{-19}$ J, $m = 9.11 \times 10^{-31}$ kg, and $\hbar = 1.05 \times 10^{-34}$ J.s, results in

$$T(E) \propto e^{-2d}, \tag{9}$$

where d is in angstroms. Equation 9 shows that for each angstrom change in separation the probability that an electron tunnels decreases by almost an order of magnitude. This demonstrates mathemtically that, in the STM system, tunneling current is a very sensitive measure of the distance between the tip and sample.

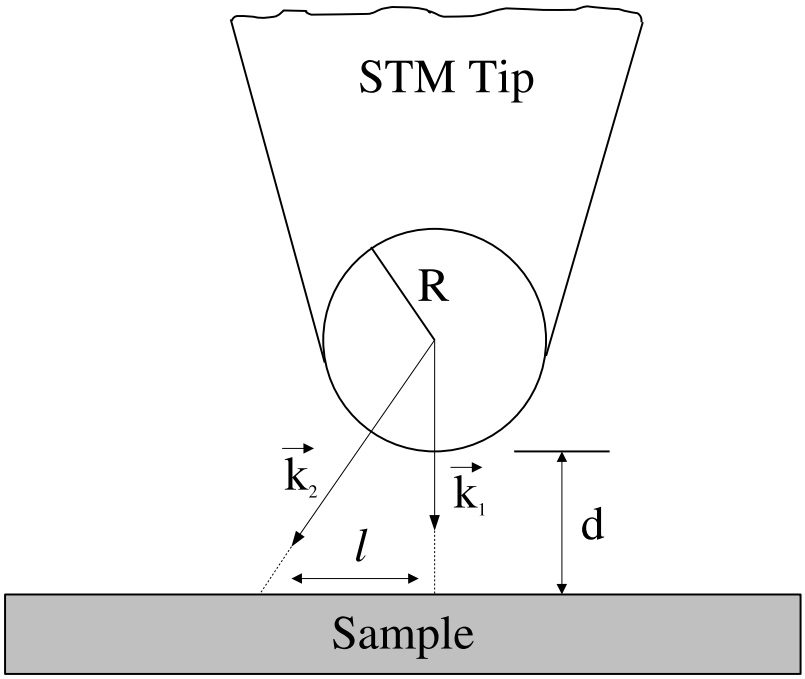

Figure 2: Schematic diagram of the tip sample geometry in STM system. The tip modeled as a sphere with radius R above a flat conducting surface.

2.1.2 Region of Tunneling

The exponential dependence of the tunneling current on the tip sample separation, d, is very important to the STM operation. To estimate the effective area of tunneling between tip and sample, a model shown schematically in Figure 2 is used. In this model, a conducting tip with radius of curvature R is kept a distance d above a flat conducting surface. Electrons present in the tip reach the sample surface with all possible k vectors and have a finite probability of tunneling from tip to sample. For simplicity the two wave-vectors shown in Figure 2, emerging normally to the tip surface, are considered. Electrons with wave-vector k_1 will tunnel to the sample with probability $\sim e^{-2\,k_1\,d}$. As a rough approximation, the wave-vector k_2 can be determined by assuming that its transmission probability is reduced by a factor of $1/e^2$ from that of k_1. From the geometry in Figure 2, the above condition is given by:

$$e^{-2}\,e^{-2\,k\,d} = e^{-2\,k\,\{\sqrt{(d+R)^2+\ell^2}-R\}}. \tag{10}$$

Solving the above equation for ℓ:

$$\ell = \sqrt{\frac{2(R+d)}{k} + \frac{1}{k^2}} \simeq \sqrt{\frac{2(R+d)}{k}}, \tag{11}$$

where the last equality holds for $(R+d) \gg k^{-1}$. For $d = 5\,\text{Å}$ and $k = 1\,\text{Å}^{-1}$, then Equation 11 shows that for a tip electrode with a radius of curvature $R = 200\,\text{Å}$, the tunnel current is confined to a current beam width $\ell = 20\,\text{Å}$. The exponential decay of electronic wavefunctions into the tunneling barrier makes it possible to form such localized beams of current.

2.1.3 Imaging

The STM can perform extremely high resolution imaging of surfaces since its tunneling current usually is confined to a very narrow electron beam. Imaging is accomplished by mounting the probe tip (a sharpened piece of metal wire) and the sample to two different piezo scanners that are capable of moving on an angstrom scale in three orthogonal directions. By convention, the X-Y plane is taken to be the plane of the sample, so that the Z direction is perpendicular to the sample surface and parallel to the tip direction. During imaging, a constant voltage bias is applied between the tip and sample. When the tip and sample are close enough to give a measurable flowing tunneling current, the flowing current is compared to a reference signal that is determined by the system electronics. The tip is then scanned across the sample surface and the resulting variations in tunneling current are due to surface topography changes. These variations in tunneling current are compensated for by an electronic feedback circuit, which adjusts the tip sample separation to maintain a constant tunneling current at each point during the surface scan. Then a tunneling image can be constructed by recording the voltage signal sent to the Z scanner as a function of tip lateral position on the sample surface. The lateral resolution of STM imaging is determined roughly by the width of beam current as was calculated in the previous section. Although the concept of electron quantum mechanical tunneling seems straightforward, the construction of a practical STM system initially was difficult because of problems associated with maintaining the angstrom scale separation between tip and sample during imaging.

2.2 Instrumentation

The microscope used in this research was designed and constructed by our group. More details on the design and operation of the microscope that was used to perform the research in this thesis is available in Refs. [14] and [15]. Some design modifications were introduced to the microscope during the course of this work in order to optimize its operation and to further enhance its capabilities.

2.2.1 Microscope Head

Figure 3 illustrates a top view of the microscope scanning head. Three piezoelectric tube scanners with 0.75 mm walls and 6.4 mm diameter are located at the corners of an equilateral triangle of side 18 mm. A fourth piezoelectric scanner with 0.75 mm wall and 12.7 mm in diameter is located at the center of the equilateral triangle formed by the other three tubes. Each of the four piezo scanners is coated with a single silver electrode on the inside of the tube and four quadrant electrodes on the outside. Since the ultimate goal of the proposed work is acquiring BEES measurements on single nanocrystals, both the sample jig and sample platen are modified to allow for the BEES signal to be acquired along with the conventional tunneling signal. As shown in Figure 3(a), the sample platen consists of two electrically isolated pieces that are mounted to the top of the center scanner. One of the platen pieces is connected to a wire that is used in measuring the tunneling current, and the other piece is connected to a wire that carries the BEES current.

The outer three scanners are used to coarse the tip during the modified (quick) approach. In the careful (slow) approach, the center scanner retracts the tip about one micron before every coarse motion trial. When the tip is in tunneling range, the center scanner controls tip sample separation (Z), while the outer three scanners raster the tip on the sample surface (X and Y). In addition, the outer scanners provide coarse motion of the tip in X and Y directions over about 2 mm distance range on the sample surface. Thus the microscope is very effective for studying surface properties over long distance range. As will be shown in later sections, this design has been very effective in studying nanocrystals samples, since nanocrystals densities are not uniform, and we have to move large distances on the surface

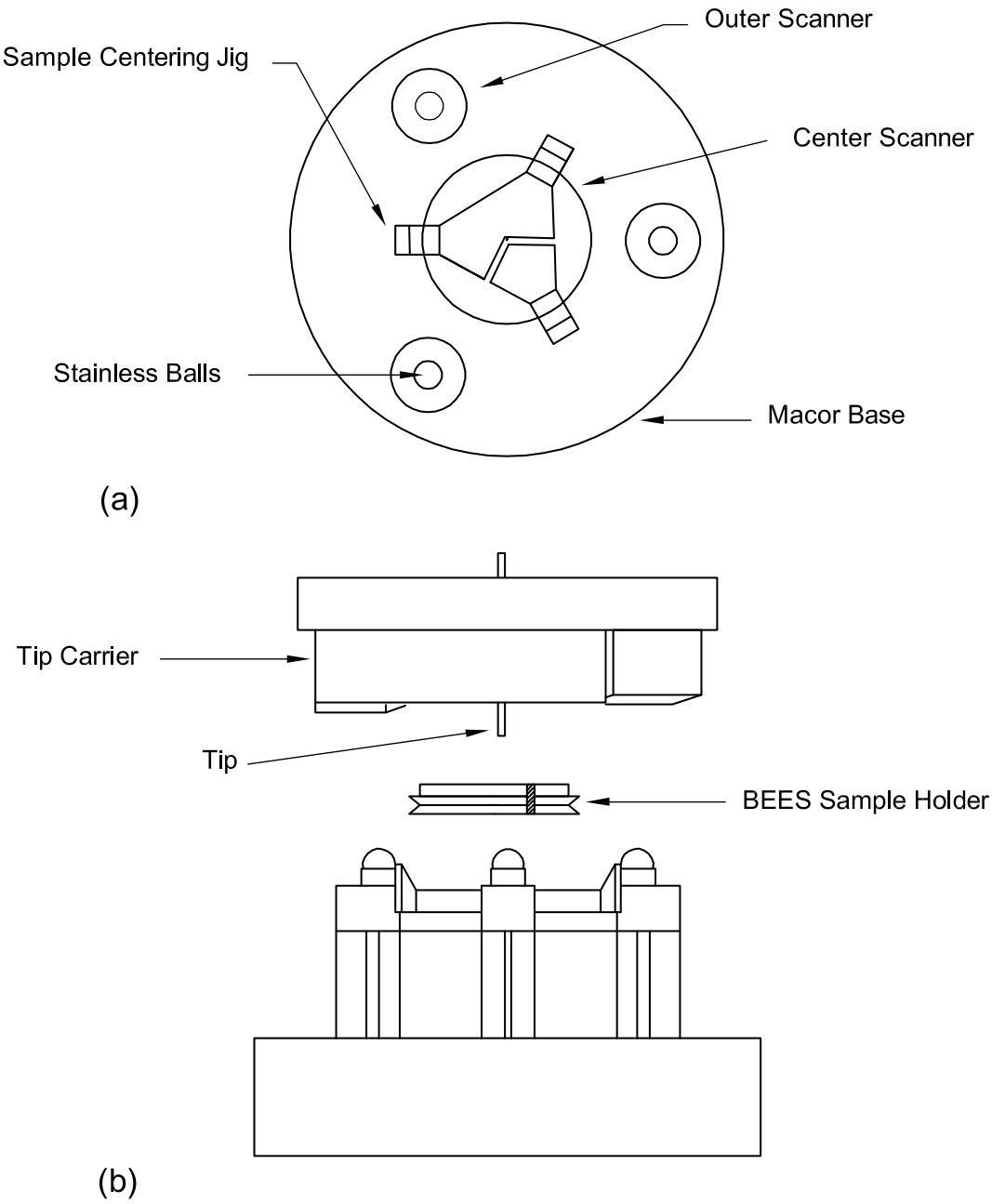

Figure 3: (a) Top view of microscope scanning head. The figure shows the positions of the four piezo tube scanners and the jig for sample alignment during the transfers process. The sample jig is divided into two electrically isolated metal pieces that back contact the sample holder and are connected to the BEES and tunneling current amplifiers. (b) Side view of the tip carrier, BEES sample holder, and microscope scan head. The sample sits on the central piezo. The tip carrier is supported by three outer piezo scanners.

to find single, isolated nanocrystals. Figure 3(b) illustrates a side view of the tip carrier. The tip is mounted pointing down inside the carrier and is coaxial with it. The bottom of the tip carrier has threefold symmetric Cu ramps bolted to an aluminum backing plate. After the transfer, the carrier is positioned on top of three stainless steel balls that are mounted on top of the three outside scanners. The tip sample separation is determined by the rotational position of the tip carrier on top of these three balls.

2.2.2 Microscope Chamber

The tunneling based experiments described in this thesis are carried out with an ultrahigh vacuum cryogenic microscope, which was designed and constructed by our group [14]. Figure 4 shows the overall chamber that includes both the microscope and the surface treatment chamber. System components include a spherical sample preparation and characterization chamber, a horizontal manipulator for sample and tip treatment, a liquid helium cryostat housing the microscope, and a vertical translator that moves both tips and samples between the analysis chamber and the microscope. The entire system rests on four vibration isolation legs. The microscope head is supported by three springs that have several hertz natural frequency for further vibration isolation. An exchange gas cylinder that surrounds both the microscope can and the outside wires has been added to the system. The cylinder is made out of stainless steel and therefore is expected to better shield the wires from external electric fields. During low temperature operation, the cylinder is completely submerged in the cooling liquid and is filled with a few hundred millitorr of helium gas for efficient cooling of the microscope can.

Our microscope is capable of atomic resolution as will be shown in next section, liquid helium operation, and an external magnetic field. The system is thermally stable after cooling, since its cryostat is submerged in the cooling liquid. Submerging the cryostat is also essential for the incorporation of a superconducting magnet. Moreover, the system has the capability of in-vacuum exchanging of both tips and samples. That allows the system to be kept under vacuum and at low temperatures for very long times.

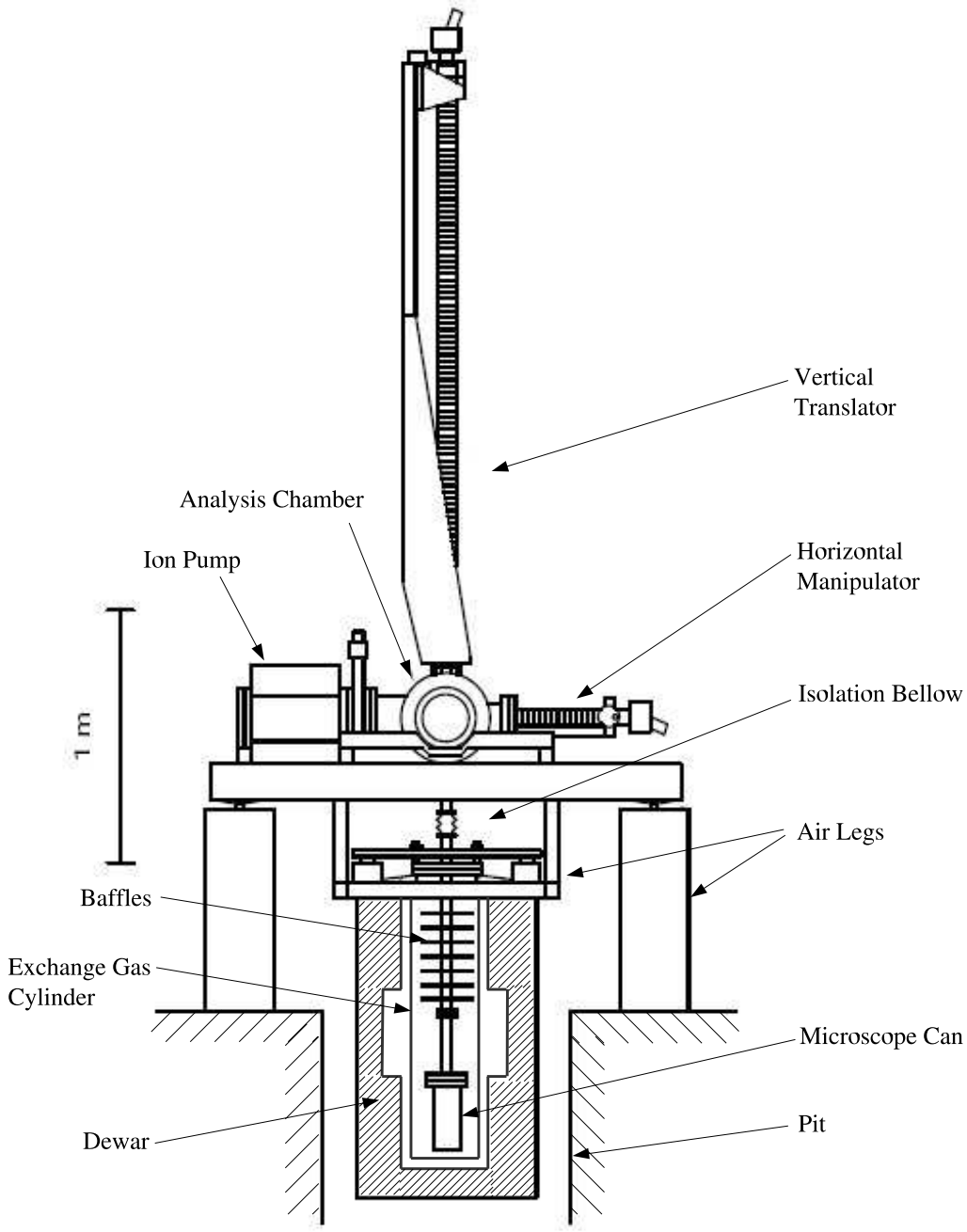

Figure 4: Side view of the low temperature STM system. The system is isolated from the ground vibration by a set of four air legs. The microscope chamber is decoupled from the analysis chamber by another set of four air legs and an isolation bellows. The vertical translator is mounted on the center of the chamber and moves tips and samples down to and up from the microscope. The system cryostat contains a series of baffles that are mounted along a tube to reduce thermal radiation. As a new design modification, a stainless steel exchange gas cylinder is used to electrically shield the microscope can and wires. In addition, the cylinder is designed to maintain a few hundred millitorr of helium gas to enhance thermal cooling of the microscope.

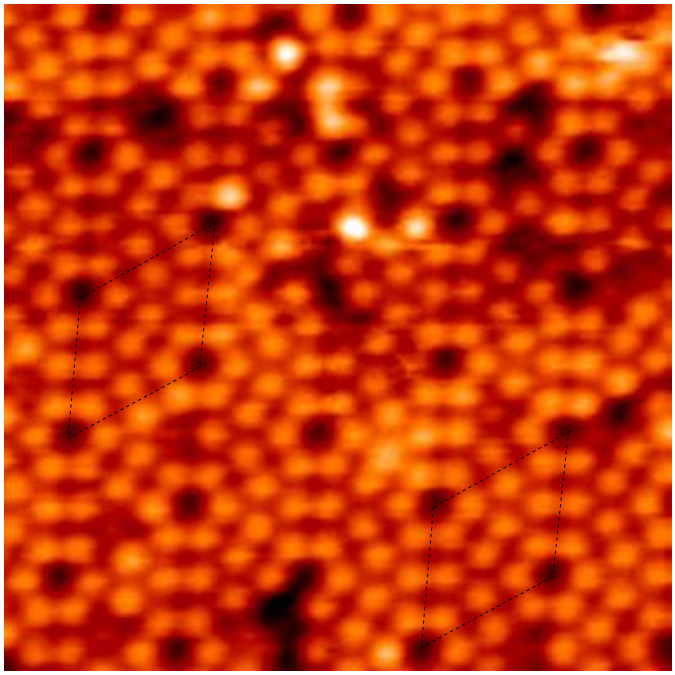

Figure 5: 120×120 Å scanning tunneling image of Si(111) 7×7 surface reconstructions at room temperature in UHV. Two unit cells are marked with black dotted lines. Each unit cell contains 12 adatoms and bounded by four minima corresponding to empty adatom positions. Image acquired at -2 V tip voltage and servo set point at 100 pA.

2.2.3 Microscope Testing with Si(111)

Images presented in this section were taken for the purpose of testing the microscope's lateral and vertical resolutions. Silicon has a diamond lattice crystal structure. The diamond crystal structure can be thought of as two merged FCC cells offset by $a/4$ in x, y, and z directions. When (111) surface of silicon is heated to sufficiently high temperature under ultra high vacuum conditions, the surface atoms rearrange for a more energetically stable configuration called 7×7 reconstruction. Instead of a simple pattern, the new arrangement involves several types of atomic positions in the top three layers to form a much larger unit cell. The first STM resolution of Si(111)-7×7 surface reconstructons was done by Binning, et al. [16]. The reconstruction was then modeled by Takayanagi as a Dimer Adatom Stacking-fault (DAS) structure constituted by three main regimes: bulk, reconstruction, and adatom [17]. The bulk regime lies beneath the second reconstruction layer and retains the unconstructed $(111) - 1 \times 1$ structure. The second reconstruction layer exhibits a local 1×1 configuration and is formed from 36 atoms of top-most crystal layer and is called the

dimer. The first reconstruction layer also exhibits a local 1×1 configuration and constructs the stacking-fault. The fault from this layer lies on either of the subcells in the 7×7 unit cell. The adatom layer exhibits a local 2×2 configuration and is the product of 12 adatoms in triangular formation. Each adatom is bound to 3 silicon atoms in the stacking-fault layer.

The sample used for microscope calibration is highly doped Si(111) with $0.1\,\mathrm{Ohm} - \mathrm{cm}$ resistivity. The 7×7 reconstruction is generated as follows. A silicon sample is cut out from a wafer with about 8 nm thick native oxide layer and mounted on a molybedium sample holder that has a 4 mm diameter hole in its center. The hole allows efficient electron beam heating at the back of silicon substrate. Next, the sample is transfered into the UHV STM chamber and degassed at 650° C for about 12 hours. The sample is then heated by electron bombardment to 900° C for about 5 minutes in a vacuum not exceeding 10^{-8} Torr. This procedure results in fairly clean surfaces. After the sample is allowed to cool down to room temperature, it is transfered into the microscope and a careful approach is used to bring the tip into tunneling range. Imaging is done at $-2.0\,\mathrm{V}$ (tip is negative) and 100 pA servo set point. Figure 5 shows a representative image of the prepared silicon surface as imaged by our microscope at room temperature. Two unit cells of the 7×7 reconstruction are marked by black dotted lines. The unit cells are clearly bounded by the lines of minima with deep corners. Inside each cell, twelve maxima appear. The diagonals of the reconstruction unit cell are about 46 and 29 Å, which are in very good agreement with the crystallographic values and previous STM measurements [16].

2.3 Nanocrystal Imaging

STM spectroscopic studies require a very stable tip-sample junction. The tip also needs to be clean when acquiring spectra. Nanocrystals have small masses; therefore, the high electric fields associated with STM measurements can perturb their positions on the substrate, resulting in slight motion during imaging. The high fields sometimes result in nanocrystals being transfered to the tip particularly during spectroscopic measurements. Thus, in order to investigate the properties of nanocrystals materials at the single nanocrystal-level, high quality samples are prepared and subsequently immobilized on a conductive surface.

There have been many different approaches for preparing immobile nanocrystals samples for STM measurements. The success of each technique depends mainly on the net electrostatic charges residing on the nanocrystals and the type of functionalized group attached to its surface. These two factors are usually controlled during the prepartion processes. Nanocrystals with a net electrostatic charges and functionalized ligand groups interact strongly with bare metal surfaces. Since nanocrystal motion under the STM field was occasionally present, such a system has been imaged with partial success with STM at room temperature [18]. Complementary chemical modification of the subsrate surface has also been tried in order to bind nanocrystals with functionalized ligand groups [19].

Nanocrystals used in our research are coated with a passivating layer of organic molecules. This layer is chosen to prevent nanocrystals from agglomeration and degradation while in solutions. The presence of this layer results in a very large mobility of nanocrystals on the surface. The mobility is larger for atomically flat surfaces. For graphite substrate with surface steps at room temperature, individual nanocrystals are imaged by STM only when they are pinned on a surface step [20]. Nanocrystal imaging at low temperatures is expected to be of better quality than room temperature imaging, since cooling can quench thermally induced motions of nanocrystals on the surface. However, the high electric field required for tunneling can still affect imaging quality even at low temperature [21]. The tip induced motions of nanocrystals make it very difficult to image single nanocrystals and to reproduce spectroscopic measurements. In previous studies by our group, a new technique has been developed to immobilize gold nanocrystals on Au(111) surfaces [21]. This technique involves chemical modification of the Au(111) surface by growing a uniform self assembled monolayer (SAM) of 1,4-benzenedimethanethiol (xylenedithiol, or XDT). XDT orients vertically on Au(111) leaving a surface of exposed active thiol groups in place of the relatively inert gold surface. This technique is briefly described in next section and is used in preparing all samples studied in this thesis.

2.3.1 Nanocrystal Preparation

Nanocrystals were initially grown hoping to have a nanometer scale system analogous to the well known self assembled monolayer system on extended surfaces. Initial characterization of nanocrystals system using laser desorption mass spectrometry (LDI-MS) and x-ray diffraction (XRD) revealed that the system contain highly uniform and separable compounds [22] with inorganic core masses and dimensions corresponding to theoretically predicted stable structures [23]. Further LDI-MS and XRD analysis of nanocrystals system was then implemented to refine reaction parameters in order to prepare nanocrystals in the size range at which quantum effects become dominant.

Gold nanocrystals samples are synthesized and purified using the colloidal chemistry method. The preparation procedure follows a stoichiometric modification of the biphasic procedure originally described by Brust and coworkers [24]. The first step is adding 2 mL of 40 mM hydrogen tetrachloroaurate(I) (1.0 mmol), in water, to 4 mmol tetraoctylammonium bromide (TOAB) in 80 mL toluene. The formation and transfer of the $[AuBr_4]^+[TOA]^+$ complex is indicated by a colorless aqueous phase and dark red organic phase. Adding 3.0 mmol of thiol (RSH; R = C_4, C_6, C_{12}, C_{18} or benzyl) and stirring for 20 minutes results in a cloudy white toluene layer. The cloudy layer indicates the quantitative formation of the polymer (*P-AuSR*) and disulfide by-product (*RSSR*). The reducing agent, > 10 mmol sodium borohydride in 10 mL water, is introduced with vigorous stirring of the solution. After about one minute of introducing the reducing agent, the organic layer color becomes opaque (black/brown). Depending on the desired nanocrystal size, the solution is allowed to stir under ambient conditions for a specified period of time. After stirring for the specified time, the aqueous layer is removed and discarded, and the toluene is allowed to evaporate almost completely. While leaving the other reactants and byproducts in solution, excess acetone is then added to the concentrated toluene solution in order to precipitate the nanocrystals. The nanocrystals are allowed to precipitate overnight at $0 - 15^\circ$ C before filtering. The filtered precipitate is washed a few times with ethanol and then dissolved and precipitated a few more times to ensure the removal of all other reactants and by-products. The washed product is then used for mass spectroscopic analysis and size separations for

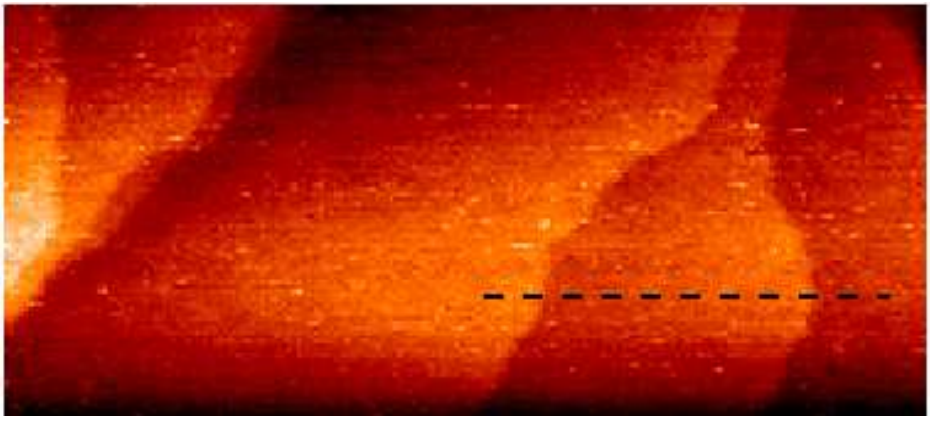

Figure 6: 200×90 nm scanning tunneling image of about 120 nm thick gold film on mica substrate at room temperature. Tip voltage at -1 V and servo set point at 100 pA.

further optical and electronic structure studies.

2.3.2 Gold on Mica Substrate

The substrate used for imaging nanocrystals is gold, thermally deposited on an atomically flat mica substrate. Au is known to grow in the (111) direction when deposited at high temperature. Au(111) is chosen as a substrate, since its surface can be consistently prepared, cleaned and characterized in vacuum. Au(111) is relatively inert, however it can be functionalized easily with thiol (SH) groups. In addition, Au(111) has almost no features in its density of states around the Fermi level, therefore, it has spectroscopic advantages over other substrates.

Au(111) substrates are prepared by depositing $120 - 140$ nm thick gold film on a mica sheet. The deposition is done at a rate of 1 Å/S in 10^{-6} Torr vacuum. The mica sheet is baked at 400° C for few hours before the deposition and is kept at the same temperature during deposition. This procedure is known to result in a gold surface along the (111) direction with atomically flat terraces [25]. After the evaporation, the gold thin film was mounted on a STM sample holder and transported to ultra high vacuum chamber for sputtering and annealing. Thin films initially are sputtered for 15 minutes in 6.5×10^{-5} Torr neon gas environment at 500 eV ion energy. The substrates subsequently are annealed at 420° C for 15 minutes. That usually results in a clear low energy electron diffraction (LEED) pattern of the Au(111) surface. Figure 6 shows an STM image of Au(111) surface that is

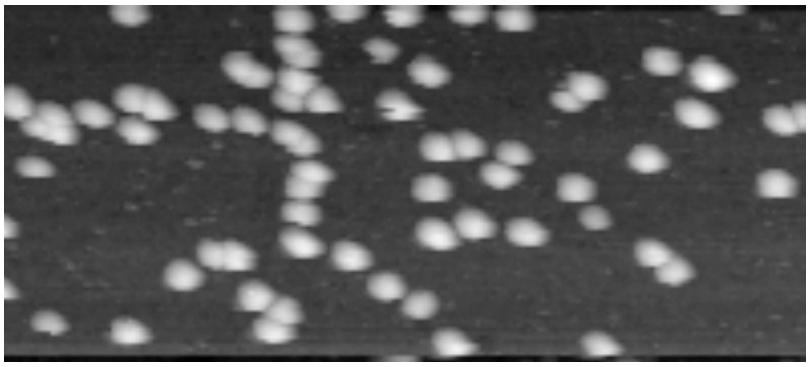

Figure 7: Tunneling image of gold nanocrystals on atomically flat gold thin film. The substrate consists of 10 nm thick gold film thermally deposited on mica substrate. Nanocrystals are chemically attached to the gold surface using a monolayer of self assembled xylenedithiol molecules. Image is taken at -1.0 V tip bias voltage and 100 pA servo set point at 77 K temperature.

prepared with the above procedure. The surface contains atomic steps with large atomically flat terraces.

After completing the gold surface preparation, the A(111) substrate is taken out from the vacuum chamber, and the sample space is intially vented to dry nitrogen gas in oder to keep the surface clean. The substrate then is dipped in a 1 mM solution of xylenedithiol dissolved in tetrahydrofuran (THF) for one hour [26]. The substrate is thoroughly rinsed with THF solution to remove excess xylenedithiol from the surface then is covered with a small beaker and allowed to dry. Since our studies require low coverage of nanocrystals, a known quantity of nanocrystals solution with known concentration was deposited on the modified Au(111) surface using a micropipette. After depositing the nanocrystals solution, the solvent is allowed to dry slowly by covering the substrate with a small beaker. The surface is rinsed to remove unbound nanocrystals by dropping several drops of toluene on the substrate surface. Toluene was chosen for rinsing since it is used for dissolving the nanocrystals. In addition, rinsing the substrate with toluene does not dissolve the already grown SAM on the Au(111) surface.

Bare Au nanocrystals have been chemically bound to xylenedithiol modified Au(111) surface [26]. The binding mechanism suggests a covalent chemical binding between sulfur atoms and gold atoms on the nanocrystals surface. Since our crystals are coated with either

alkanethiol or dodecanethiol ligands, we think that upon depositing the nanocrystals on the surface, interdigitation between the ligand molecules and the SAM molecules allows some of the sulphur atoms on the SAM to interpenterate the ligand and bind with the gold atoms on the surface. A tunneling image of our nanocrystals that were prepared using the above described method is shown in Figure 7. The image shows single, immobile, isolated nanocrystals.

2.3.3 Gold on Silicon Substrate

The growth of a very thin gold films on silicon substrate is chosen so that we can perform both BEES and tunneling spectroscopic measurements on the same sample. Metal-semiconductor contacts at the atomic scale are known to form an interface with a potential barrier. This interface barrier is known as Schottky barrier and will be used as a filter in our BEES measurements as will be shown in chapter IV. Figure 8 shows schematically the preparation of our BEES samples. We start with about $400\,\mu$m thick silicon(111) wafer and about $5\,\text{Ohms} - \text{cm}$ resistivity. The wafer usually has a 10 nm thick native oxide layer. Initially, the wafer is cleaned with organic solvents in order to remove organic and metal contamination on the surface. The native oxide layer is then removed by dipping the wafer in HF acid for several seconds. The wafer is loaded into a furnace in the clean room for 120 seconds at 850° C, and as a result a uniform layer of about 8 nm of SiO_2 is grown on its surface. The wafer is diced into small square chips of 7 mm side length in order to fit into our BEES sample holder.

The next step involves the removal of the thermally grown oxide layer and the immediate deposition of the gold thin film. Initially, the Si chip is cleaned successively with trichloroethylene, acetone, and ethanol solutions in an ultrasound for 4 minutes each. The chip then is dipped in 1:10 volume ratio HF:ethanol solution for about 150 seconds. This process is known to result in a hydrogen terminated silicon surface that is protected against oxidation for a few minutes [27]. The resulting Si surface is rinsed throughly with water and dried with nitrogen gas to remove the residuals of the solutions. The chip immediately is mounted on our designed deposition mask and loaded into the e-beam evaporator chamber

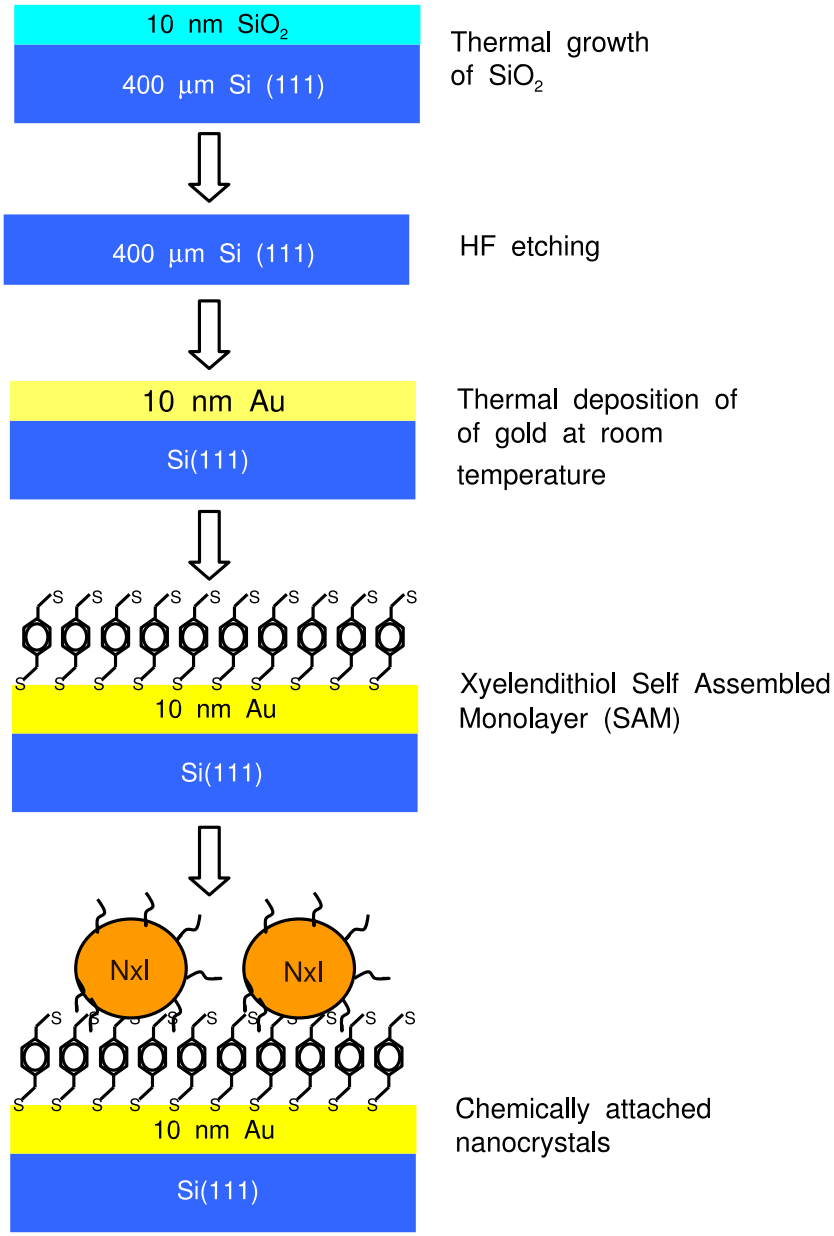

Figure 8: Schematic drawing of sample preparation procedure. In the first step, the native oxide layer is removed with HF acid. A new 8 nm thick SiO_2 layer is thermally grown on the surface. The grown oxide is removed again with HF and about 10 nm thick gold film is thermally evaporated on the cleaned Si surface. Xylenedithiol SAM then is grown on the evaporated gold. A nanocrystal solution is dropped on the SAM surface, and therebye nanocrystals are chemically attached to the substrate through binding with the thiol groups on the SAM molecules

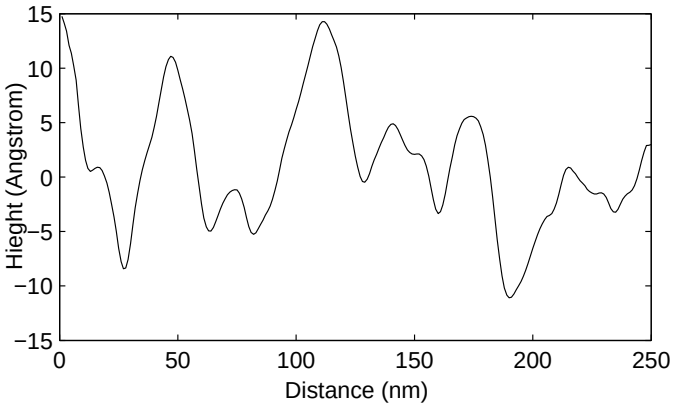

(a)

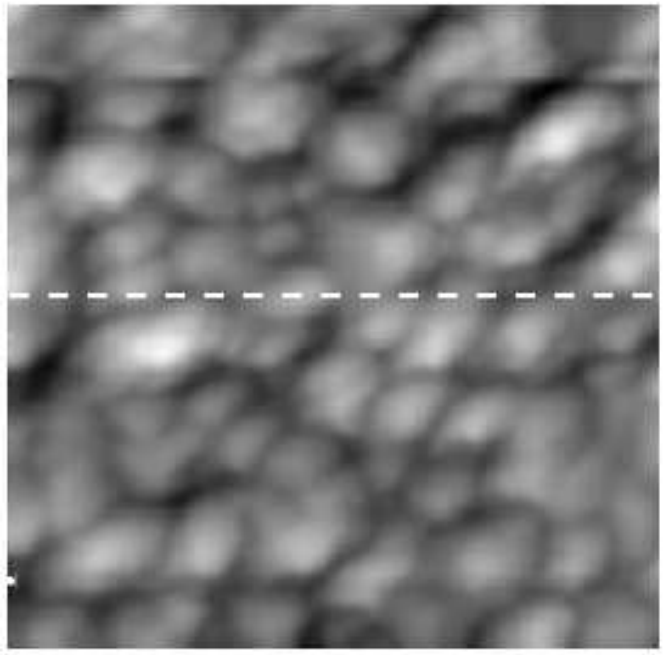

(b)

Figure 9: STM imaging of Au/Si(111) at room temperature. (a) Line profile of the gold film surface. Gold grains sizes are about 1.2 nm high and 15 nm wide. The grains are distingushed from nanocrystals, since the nanocrystals are more spherically symmetric. (b) 250 nm^2 scanning tunneling image of 10 nm thick gold film on Si(111) substrate at room temperature. Tip voltage at -1 V and servo set point at 100 pA.

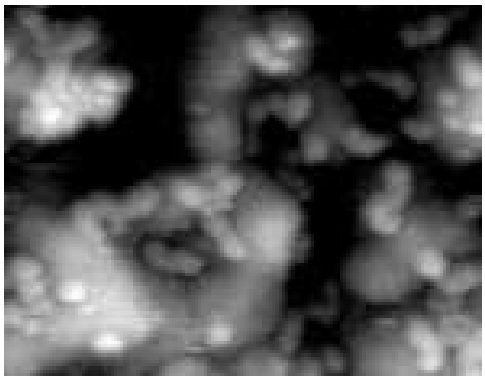

Figure 10: Tunneling image of gold nanocrystals on BEES substrate. The substrate consists of 10 nm thick gold film thermally deposited on Si(111) substrate. Nanocrystals are chemically attached to the gold surface using a monolayer of self assembled xylenedithiol molecules. Image is taken at -1.5 V tip bias voltage and 100 pA servo set point at 77 K temperature.

in the clean room. The mask is designed for the deposition of 5 mm diameter gold film on top of 7 mm square Si chip. After pumping down to a base pressure of about 10^{-7} Torr, a gold film of about 10 nm is deposited on the Si surface at a rate of 2 Å/s at room temperature. STM images of the resulting gold film show large aggregates of objects that are randomly distributed on the surface. These objects result in tip crash during imaging, since they are not conductive. These objects are formed from the diffusing silicon atoms during the deposition and the subsequent oxidization. Silicon diffusion is expected because of two factors. First, our films are very thin. Second, the silicon atoms on the surface might gain enough kinetic energy during the deposition from the hot gold vapor especially if the source is close to the target. This problem is resolved by dipping the deposited gold film in HF acid for several seconds. The film subsequently is cleaned with deionized water and ethanol for residual cleaning and quick drying. A procedure similar to that used for gold on mica samples then is followed to chemically deposit nanocrystals on the BEES substrate.

Figure 9(b) shows a tunneling image of the resulting gold thin film at room temperature. Figure 9(a) shows a line profile of the image surface. Our tunneling images of the resulting surface show that the deposited film consists of grains that are about 1.2 nm in height and 15 nm width. The shapes of the grains are rounded but not spherically symmetric as the nanocrystals.

A procedure similar to that used for the Au/mica substrate was followed to grow nanocrystals on the Au/Si substrate. Figure 10 shows an STM image of gold nanocrystals on BEES substrate that was taken at liquid nitrogen temperature. The image shows single isolated nanocrystals with different sizes. Nanocrystals seem to be strongly bound in valleys between the grains.

CHAPTER III

SCANNING TUNNELING SPECTROSCOPY OF NANOCRYSTALS

In this chapter, the experimental results of Scanning Tunneling Spectroscopy (STS) on single nanocrystals is presented. These experiments are an extension of work on nanocrystals that was previously started by Bigioni and Harrell [15, 21]. In the first sections of this chapter, some of the concepts of single electron tunneling are introduced. Experimental STS data taken at 77 K on isolated gold nanocrystals is presented. Also discussed are experimental studies of the effect of tunneling parameters on our measurements. These parameters include tip-nanocrystal separation and nanocrystal-sample resistance. The effect of change in the local electrostatic environment of our nanocrystals on the tunneling current is presented. In addition to the physics extracted from these studies, they are essential for both the acquisition and interpretation of our BEES measurements on single nanocrystals, which are presented in the following chapter.

3.1 STS Essentials

The theory of electron tunneling in small capacitance systems has been developed by Likharev and Averin [11]. In this chapter, the basic concepts of STS that are related to our studies are introduced. The charging of a neutral piece of metal with an extra charge e requires an energy:

$$E_c = \frac{e^2}{2C}. \tag{12}$$

The above expression is called the electrostatic charging energy. C is the capacitance between the particle and its environment. For a completely isolated particle, C is the self-capacitance. For a sphere with radius r, the self charging energy is $E_c = e^2/8\pi\varepsilon_0 r$. For a macroscopic piece of metal, E_c is negligible but for a particle with $r < 10\,\text{nm}$, E_c becomes

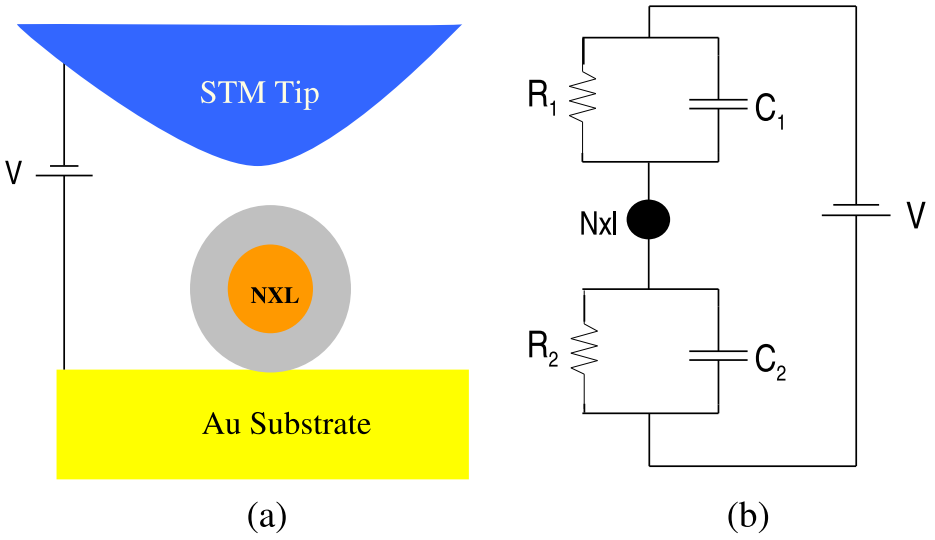

Figure 11: Schematic of STS on single nanocrystal. (a) In STS experiment, STM tip is positioned on top of a nanocrystal, and a double barrier tunneling junction is then formed. The feedback of the servo is disabled to maintain a constant tip-substrate separation during STS spectrum acquisition. (b) Equivalent electric circuit of STS on single nanocrystal. Capacitive coupling determines the voltage division between the two junctions ($C_1/C_2 = V_2/V_1$). The tunneling rate through each junction is determined by its resistance.

significant. The schematic diagram in Figure 11(a) shows our experimental set up for STS on a single nanocrystal. The equivalent electric circuit is shown in Figure 11(b). In our experiments, C is the sum capacitance of the two tunnel junctions and will be referred to as $C_t = C_1 + C_2$ throughout this thesis. Also in our experiments, the two tunneling junctions are formed between tip-nanocrystal and nanocrystal-substrate. The capacitance of these junctions is on the order of 0.1 aF (1 aF $= 10^{-18}$ F). That results in about 600 meV charging energy for our nanocrystals. This is above room temperature and is why these nanocrystals are good candidates for constructing single electron devices at room temperature.

The suppression of tunneling current at low voltage around zero is known as the Coulomb blockade. This is because the voltage source has to provide a measurable amount of energy before adding an electron to the nanocrystal. Because of the additional charging energy involved with having two extra electrons on the nanocrystal, at voltages above the Coulomb blockade threshold, current flows via a sequence of well defined tunneling events.

With no voltage applied to the STS circuit, the electrochemical potentials of tip and substrate are aligned. In order to minimize its energy, the nanocrystal will attempt to

align its electrochemical potential with that of tip and substrate. However, because a nanocrystal has discrete energy levels, it can only change its potential through a discrete amount of energy. Therefore, in the minimum energy state, the electrochemical potential of the nanocrystal μ_{nxl} may not be aligned with that of tip and substrate.

$$|\Delta\mu_{nxl}| \leq \frac{e^2}{2C_t}, \tag{13}$$

where $\Delta\mu$ refers to the difference between nanocrystal and tip Fermi levels at zero applied bias between tip and substrate. This misalignment between the Fermi levels is often referred to as a polarization charge (Q_0). Equation 13 can be equally written as

$$|Q_0| = C_t \frac{|\Delta\mu_{nxl}|}{e} \leq \frac{e}{2}. \tag{14}$$

Because Q_0 is a polarization due to potential misalignment, it is a continuous quantity. This effect can be accounted for by assuming that a continuous charge, Q_0, is residing on the nanocrystal at zero applied bias. The condition for overcoming the Coulomb blockade can therefore be written as

$$eV = \frac{(e+Q_0)^2}{2C_t} - \frac{Q_0^2}{2C_t} \implies V = \frac{e}{2C_t}\left[1 + 2\frac{Q_0}{e}\right]. \tag{15}$$

It is possible to modulate Q_0 using an electrostatically coupled gate to the nanocrystal. This is known as a single electron transistor [28]. STS studies on very small nanocrystals ($r < 2\,\text{nm}$) show Coulomb blockade gaps much larger than the value expected from Q_0 on the nanocrystals. The large Coulomb blockade is attributed to the presence of an energy gap between the HOMO and LUMO levels in these small nanocrystals [29, 30].

The energy diagram of STS on a single nanocrystal is shown in Figure 12. At zero applied bias, the Fermi levels of tip, nanocrystal, and substrate equilibrate to their lowest energy configuration, shown as a dashed line in the Figure. For simplicity, the residual charge on the nanocrystal is taken to be zero ($Q_0 = 0$). The energy supplied by the voltage bias is represented by shifting the Fermi levels of tip and sample relative to each other. The total applied voltage will be divided between the tunneling junctions according to the relation $V_1/V_2 = C_2/C_1$. Therefore, for $C_1 \neq C_2$ the work done by the voltage source for

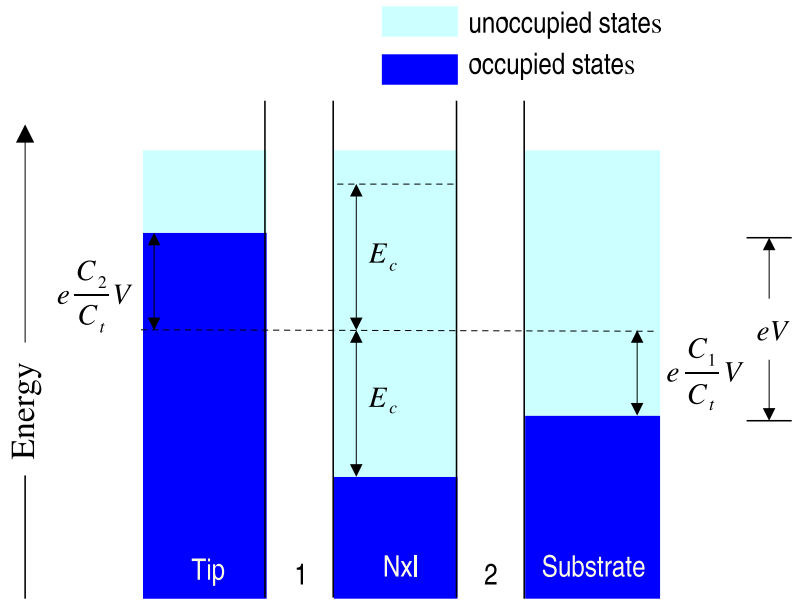

Figure 12: Energy diagram for double barrier tunneling junction. For a tunneling event to occur, the voltage bias must supply the energy to charge the nanocrystal with one electron. For source energy less than the charging energy, no current flows in the system, and this is known as Coulomb blockade. At negative tip voltage, tunneling events occur either from the tip to an empty state on the nanocrystal or from an occupied state on the nanocrystal to the substrate.

tunneling through junction 1 is not equal to the work done for tunneling through junction 2. For tunneling through junction 1, electrons coming from the tip will add a charge e to the nanocrystal. This raises the energy levels on the nanocrystal by an amount E_c relative to the tip. Tunneling events only occur when available filled states on the tip align with empty final states on the nanocrystal. Similarly, tunneling events from the nanocrystal to substrate across junction 2 necessarily subtract a charge e from the nanocrystal. This displaces the energy levels on the nanocrystal by an amount E_c relative to the substrate Fermi level. Tunneling across junction 2 occurs when sufficient energy is applied to align the Fermi level of the substrate with the HOMO on the nanocrystal.

Figure 13(a) demonstrates one process through which current flows at voltages above the Coulomb blockade threshold. As the figure shows, an electron from the tip has sufficient energy to charge the nanocrystal, and therefore tunneling takes place. This event is followed by a second tunneling event that corresponds to discharging the nanocrystal by one electron as shown in Figure 13(b). The nanocrystal energy levels shown in this step are raised above the nanocrystal Fermi level by an amount of energy, E_c, as a result of the first tunneling event. Tunneling-out of the nanocrystal can occur from any of the available energy levels, since the electron may relax to a lower level before tunneling-out. After the second tunneling event, the nanocrystal returns to its initial state, except an electron has been moved through the entire system. In this manner, the current-carrying processes will repeat, and electron current will flow from tip to substrate. A similar two-step process is depicted in Figure 13(c,d); but, in this case the initial tunneling event occurs through junction 2. In an experiment, the voltage thresholds for the onset of these two different current-carrying processes is determined by the capacitive coupling and therefore can be quite different. In our experiments, as we show in section 3.3 of this chapter, the tip-nanocrystal junction is controlled, so the current onset is on junction 1.

3.1.1 Calculations of Tunneling Rates and Current

The descriptions in the preceding section are useful for understanding the different possible tunneling processes in our experiments. For quantitative analysis of the experiments, the

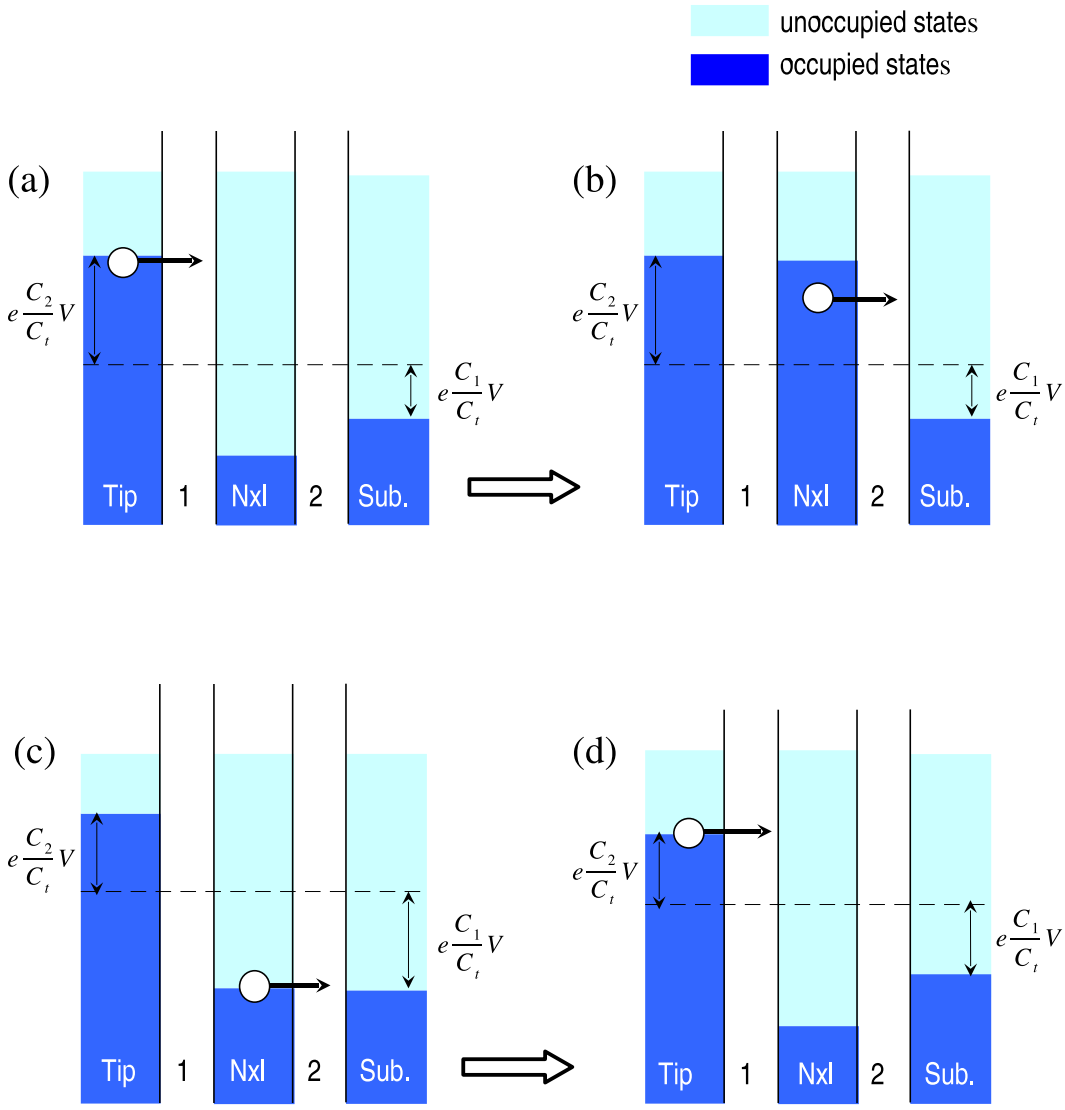

Figure 13: Current-carrying processes in double barrier tunneling junction. At voltages above Coulomb blockade threshold, current flows through two different mechanisms. (a) and (b): The initial tunneling event (a) corresponds to charging the nanocrystal with one electron and occurs across junction 1. The second tunneling event (b) corresponds to nanocrystal discharging, occurs across junction 2, and returns the nanocrystal to its initial charge state. (c) and (d): The initial tunneling event (c) occurs through junction 2, leaving the nanocrystal with one less electron. The second tunneling event (d) returns the nanocrystal to its initial state. The voltage threshold of these processes depends on the capacitive ratios in the system.

tunneling rate in each junction needs to be represented by an explicit expression. In these small capacitance junctions, the energy difference between the initial and final states is given by

$$E_{final} - E_{initial} = \Delta E = \Delta U_{charging} - \Delta W_{source}, \tag{16}$$

where $\Delta U_{charging}$ is the energy needed to charge the nanocrystal with one electron, and ΔW_{source} is the energy gained from the voltage source. Therefore, the energy involved in moving an electron from the tip to the nanocrystal through junction 1 (taking the nanocrystal from n to $n+1$ electrons) is given by

$$\Delta E_1^+(n \to n+1) = -e\,\frac{C_2}{C_t}\,V + E_c\left[2n + 1 + 2\,\frac{Q_0}{e}\right]. \tag{17}$$

When ΔE_1^+ is less than zero, the process is energetically favorable. Similarly, the energy difference for removing an electron from the nanocrystal through junction 2 is

$$\Delta E_2^-(n \to n-1) = -e\,\frac{C_1}{C_t}\,V + E_c\left[-2n + 1 - 2\,\frac{Q_0}{e}\right]. \tag{18}$$

Equations 17 and 18 represent the changes in the system energy associated with different tunneling processes. These expressions are used to calculate the tunneling rates for these processes. The tunneling rate of electrons between two metal electrodes is calculated using the Fermi's Golden Rule:

$$\Gamma(eV) = \frac{4\pi}{\hbar}\int_{-\infty}^{\infty} |T(\varepsilon)|^2 \rho_1(\varepsilon) f(\varepsilon) \rho_2(\varepsilon + eV)\,[1 - f(\varepsilon + eV)]\,d\varepsilon, \tag{19}$$

where ρ_1 and ρ_2 are spin degenerate densities of states in the two electrodes, and $|T(\varepsilon)|^2$ is the matrix element coupling electrons from the two electrodes. For normal metals, ρ_1, ρ_2, and $|T|^2$ are approximatelly constant over small energy range, so that Equation 19 becomes:

$$\Gamma(eV) = \frac{4\pi}{\hbar}\,\rho_1\rho_2|T|^2\int_{-\infty}^{\infty} (\varepsilon) f(\varepsilon)(\varepsilon + eV)\,[1 - f(\varepsilon + eV)]\,d\varepsilon. \tag{20}$$

Denoting Γ_1 as the tunneling rate through junction 1 and Γ_2 as the tunneling rate through junction 2, the tunneling rate for all possible tunneling events are then given by [31]

$$\Gamma_{1,2}^{\pm}(\Delta E_{1,2}^{\pm}) = \frac{1}{e^2 R_{1,2}}\,\frac{-\Delta E_{1,2}^{\pm}}{1 - e^{\beta\,\Delta E_{1,2}^{\pm}}}, \tag{21}$$

Table 1: Experimental parameters for calculating the current in the double barrier system of Figure 14. The capacitances of the junctions determine the voltage division, and the resistances determine the tunneling rate.

Parameter	*Value*
C_1	$2.22 \times 10^{-19}\,\mathrm{F}$
C_2	$2.95 \times 10^{-19}\,\mathrm{F}$
R_1	$3.29 \times 10^{+8}\,\Omega$
R_2	$1.16 \times 10^{+4}\,\Omega$
Q_0	-0.193
$Temp.$	$77\,\mathrm{K}$

where $R_{1,2}$ is the tunneling resistance for a particular junction, and $\beta = 1/k_B T$. At low temperature ($\beta \gg 1$), and tunneling rates are exponentially suppressed until ΔE becomes negative for that tunneling process.

In the steady state situation, there is no net accumulation of charge on the nanocrystal, so that the number of electrons entering the nanocrystal per unit of time must be equal to the number of electrons leaving the nanocrystal per unit time. This condition can be expressed as a set of linear equations. If $\sigma(n)$ is defined as the probability of the nanocrystal being occupied by n electrons, then the steady state condition is described by

$$\sigma(n-1)\Gamma_{n-1\to n} = \sigma(n)\Gamma_{n\to n-1}. \tag{22}$$

The left side of Equation 22 represents electrons entering the nanocrystal, and the right side represents electrons leaving the nanocrystal. Since electrons can tunnel into or out of the nanocrystal through either of the junctions, the total tunneling rates Γ include both of these processes. The occupation probability of the nanocrystal can be calculated using the above set of equations and the normalization condition $\sum_n \sigma(n) = 1$. The tunneling current can then be calculated from

$$\begin{aligned} I &= e\sum_n \sigma(n)\left[\Gamma_1^+(n\to n+1) - \Gamma_1^-(n\to n-1)\right] \\ &= e\sum_n \sigma(n)\left[\Gamma_2^-(n\to n-1) - \Gamma_2^+(n\to n+1)\right], \end{aligned} \tag{23}$$

where the first expression is the current through junction 1, and the second expression is the current through junction 2. They are equal because of the steady state assumption.

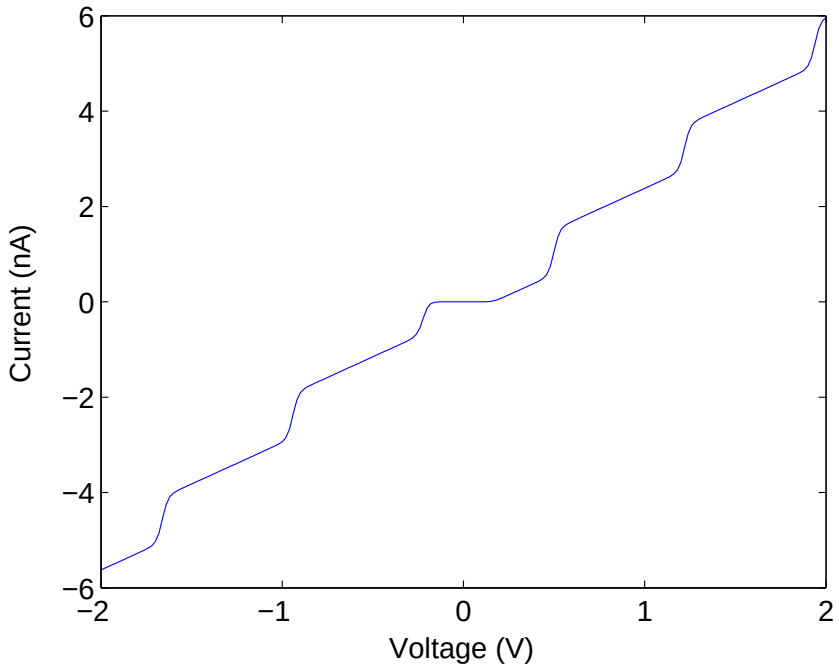

Figure 14: Calculated tunneling current through a double barrier junction using the procedure described in this section. The steady state situation is an approximation.

3.2 Tunneling Through Discrete States

The spectrum of electronic energy levels in a bulk piece of metals is considered a continuous function of energy. As the size of the metal is reduced, energy level spacing increases. This effect of size restriction of the energy level spacing is very apparent even when considering the simplest physical model of metals, a box containing noninteracting electrons. In this approximation, the spacing between two-fold spin degenerate eigenstates (measured at the Fermi level, E_F) is given by [32]

$$\delta(E_F) = \frac{4E_F}{3N} \approx \frac{0.125}{\text{Volume}} \ \ eV.nm^3, \tag{24}$$

where E_F is the Fermi level, and N is the number of electrons in the piece of metal. The last equality in Equation 24 holds specifically for gold ($E_F = 5.53\,\text{eV}$, $n = 5.9 \times 10^{22}\,\text{cm}^3$), which is the material of our metallic nanocrystals. Using Equation 24 for a gold nanocrystal with $r = 0.6\,\text{nm}$, the calculated average energy level spacing is about 138 meV, which is well above room temperature energy (25 meV). Moreover, this value for the average level spacing is larger than the thermal broadening in our experiments at 77 K ($3.5\,\text{k}_\text{B}\text{T} \simeq 23\,\text{meV}$).

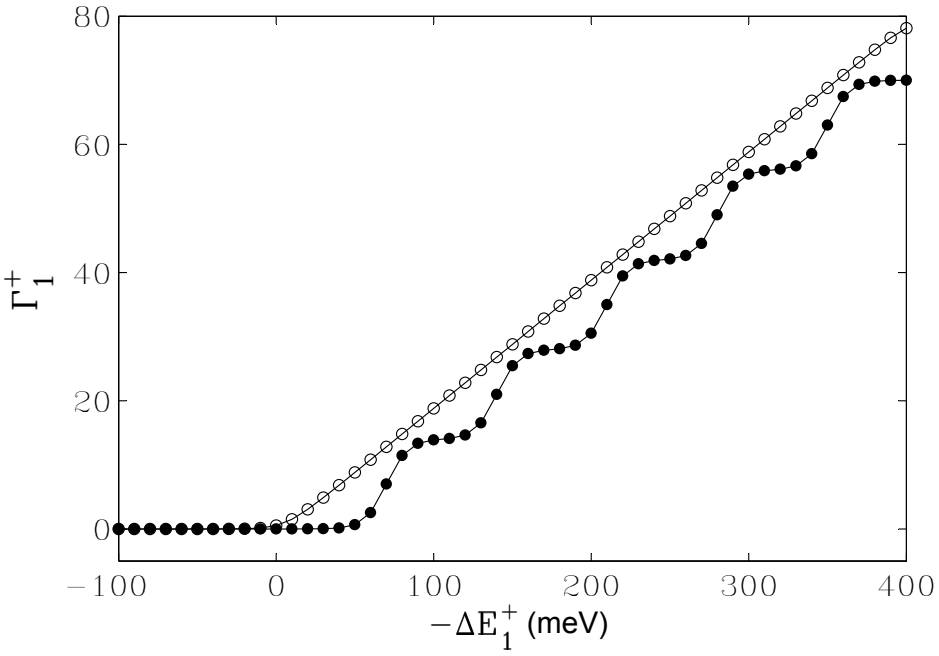

Figure 15: Comparison of tunneling rate for discrete and continuous density of states. For a continuous nanocrystal density of states (open circles) and energies above the Coulomb threshold, the tunneling rate increases linearly as a function of the applied voltage. For a discrete density of states (closed circles), there has to be an available state on the nanocrystal for the tunneling rate to increase. In this case the current increases in square steps, above the Coulomb blockade, with each step corresponding to tunneling through an individual state on the nanocrystal.

3.2.1 Introductory Theory

At temperatures $T < \bar{\delta}/K_B$ (where $\bar{\delta}$ is the average spacing between energy levels) the discreteness of the electronic density of states in nanocrystals becomes measurable. The process of tunneling through a nanocrystal with discrete energy levels can be described by a set of energy diagrams similar to those discused in section 3.1.1. The tunneling rates are modified by the discrete energy levels. For a tunneling event to occur, the system has to provide enough energy to overcome the charging barrier, and there has to be an available energy state on the nanocrystal for the electron to occupy. The modified tunneling rate for an electron to tunnel into the initially uncharged nanocrystal can be obtained using the Fermi's Golden Rule [33]

$$\Gamma_1^+(0 \to 1) = \frac{4\pi}{\hbar}\,\rho_1 \int_{-\infty}^{+\infty} |T(\varepsilon)|^2\, f(\varepsilon)\, \rho_2(\varepsilon + \Delta E_1^+) \left[1 - f(\varepsilon + \Delta E_1^+)\right] d\varepsilon, \qquad (25)$$

where ΔE_1^+ is the change in system free energy on going from a state with 0 extra electrons on the nanocrystal to a state with with 1 extra electron. ρ_1 is the density of states in the tip and can be approximated as a constant over the range of integration. ρ_2 is the density of discrete energy levels on the nanocrystal. ΔE_1^+ is determined mainly from the tunneling junctions parameters and is given by

$$\Delta E_1^+(n \to n+1) = -e\,\frac{C_2}{C_t}\,V + E_c\left[2n+1+2\,\frac{Q_0}{e}\right]. \tag{26}$$

The discrete energy levels on the nanocrystal are expressed approximately as

$$\rho_2(\varepsilon) = \sum_j \beta_j(\varepsilon), \tag{27}$$

where the function $\beta_j(\varepsilon)$ describes the width of the state j in energy. The sum in Equation 27 runs over all energy levels on the nanocrystal. After substituting, Equation 25 becomes

$$\Gamma_1^+(0 \to 1) = \sum_j \gamma_{1j} \int_{-\infty}^{+\infty} \beta_j(\varepsilon) f(\varepsilon + \varepsilon_j + \Delta E_1^+)\,[1 - f(\varepsilon + \varepsilon_j)]\,d\varepsilon, \tag{28}$$

where $\gamma_{1j} = (4\pi/\hbar)\rho_1 |T_{1J}|^2$ is defined as the rate with which electron tunnels from the tip into a particular electronic state j on the nanocrystal, and ε_j is the state energy measured from the Fermi level of the nanocrystal. In the limit where the energy levels on the nanocrystal are sharp compared with the Fermi distribution in the tip, the width of the state can be approximated as $\beta(\varepsilon) = \delta(\varepsilon)$, and Equation 28 becomes

$$\Gamma_1^+(0 \to 1) = \sum_j \gamma_{1j}\, f(\varepsilon_j + \Delta E_1^+)\,[1 - f(\varepsilon_j)]\,. \tag{29}$$

The above equation shows that the tunneling rate increases by an amount $\sim \gamma_{1j}$ each time it is energetically possible to tunnel through a new unoccupied state on the nanocrystal. Figure 15 shows a plot of the tunneling rate as a function of ΔE_1^+ for both discrete and continuous densities of states. As the figure shows, in the case of a continuum of states (open circles) on the nanocrystal, the tunneling rate increases linearly once it is energetically possible to add an electron to the nanocrystal. On the other hand, for discrete density of states (closed circles), the tunneling rate increases in small steps each time the energy is sufficient to access a new unoccupied state on the nanocrystal.

If the first tunneling event corresponds to charging of the nanocrystal, then the second tunneling event in the current-carrying processes occurs through discharging the nanocrystal. For nanocrystal discharging, there can be more than one channel through which the tunneling-out can occur. Usually, the tunneling-out step occurs from a lower-energy (n_0+1) electron state, and thus leaves the nanocrystal in an excited n_0 electron state. This implies that the nanocrystal relaxes to its n_0 ground state in a time τ_r, less than the time between tunneling events. If $\tau_r \ll \frac{1}{\Gamma_1^+}$, then the nanocrystal returns to its equilibrium state before another tunneling event takes place.

The tunneling-out process can be written in a form similar to that written for the tunneling-in process in Equation 29

$$\Gamma_2^-(1 \to 0) = \sum_j \gamma_{2j}\, f(\varepsilon_j + \Delta E_2^-)\,[1 - f(\varepsilon_j)]\,, \tag{30}$$

where ΔE_2^- is the change in system energy due to discharging of the nanocrystal. The number of energy levels that contribute to the tunneling-out rate is determined by the number of terms in the summation for which $f(\varepsilon_j + \Delta E_2^-) = 1$. The number of discharging states can be roughly estimated as follows. Let the energy level spacing on the nanocrystal be equal and given by δ. Then the condition $f(\varepsilon_j + \Delta E_2^-) = 1$ implies that $j\,\delta + \Delta E_2^- < 0$. Therefore, the number of discharging states on the nanocrystal are estimated as

$$N_{discharging} \sim \frac{|\Delta E_2^-|}{\delta} = \frac{1}{\delta}\,\left[e\,\frac{C_1}{Ct}\,V + E_c\,(1 + 2\,\frac{Q_0}{e})\right]. \tag{31}$$

The above equation is a rough estimate and is always $\gg 1$ except for the case when $Q_0 = -e/2$ and $V = 0$.

At voltages just above the Coulomb blockade threshold, there wil be one electron on the nanocrystal at any time. At these voltages the current will flow through the system in a series of two-sequential tunneling events in the discrete energy levels of the nanocrystal. The tunneling current is inversely proportional to the average time it takes an electron to complete the two tunneling events:

$$\frac{I}{e} = \frac{1}{\tau_1 + \tau_2} = \left[\frac{1}{\Gamma_1^+(0 \to 1)} + \frac{1}{\Gamma_2^-(1 \to 0)}\right]^{-1}$$

$$= \frac{\Gamma_1^+(0 \to 1)\,\Gamma_2^-(1 \to 0)}{\Gamma_1^+(0 \to 1) + \Gamma_2^-(1 \to 0)}. \tag{32}$$

A case of interest and relevant for our experiments, as is shown in later sections, is the case where the tunneling-out $\Gamma_2^-(1 \to 0)$ rate is faster than the tunneling-in rate $\Gamma_1^+(1 \to 0)$. This limit is realistic and can be experimentally achieved by controlling the tunneling junction parameters. The tunneling current is therefore reduced to the following form

$$I \approx e\,\Gamma_1^+(n \to n+1). \tag{33}$$

From the above equation, the tunneling current is expected to increase with voltage in steps similar to those shown in Figure 15. In experiments, both step width and height are expected to vary because of the effects of shape irregularities and surface capping molecules of the nanocrystal on its energy levels. In the above discusion, only the current carrying process $n_0 \to (n_0+1) \to n_0$ is considered. As mentioned before, in addition to this process, there is a second voltage threshold for which the current carrying process $n_0 \to (n_0-1) \to n_0$ also becomes favorable. For this tunneling cycle the initial tunneling event occurs through junction 2. Tunneling through these $(n_0 - 1)$ electron states also produces steps in the I-V curve.

3.2.2 Experimental Data

Figure 16(a) shows a tunneling image of our nanocrystals taken at 77 K. The substrate is made of ~ 10 nm thin gold film deposited on a silicon substrate. The image shows single, immobile, and isolated nanocrystals. Our sample is prepared using a mixture of 8, 14, 22, 28, and 34 kDa (1 kDa $= 1.66 \times 10^{-21}$ g) nanocrystals. Nanocrystals are coated with dodecanethiol and dissolved in toluene. A line profile of a single nanocrystal (marked with red dashed line in the image) is shown in Figure 16(b). It is difficult to determine the exact size of the nanocrystal from our images. This is because the gold film surface is thin and consists of grains that are comparable to nanocrystal sizes. Accurate determination of nanocrystal sizes requires atomically flat surfaces. The profile shows a nanocrystal height of about 1.4 nm and a width of about 5 nm. STM height measurements are proportional to the diameter of the nanocrystal. The correlation between STM height and core mass of

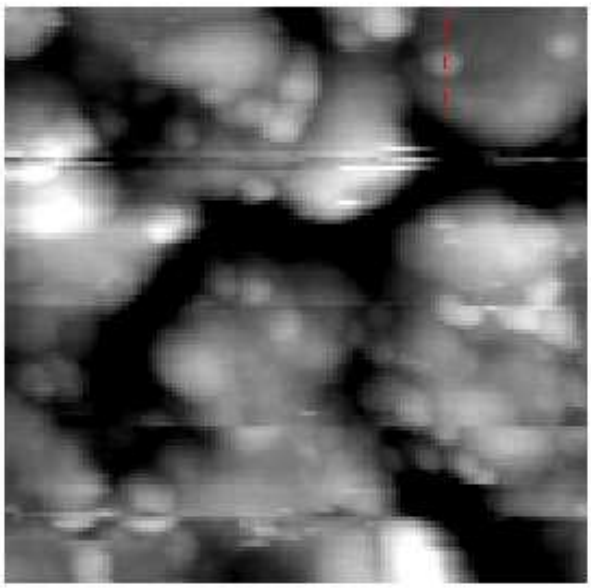

(a)

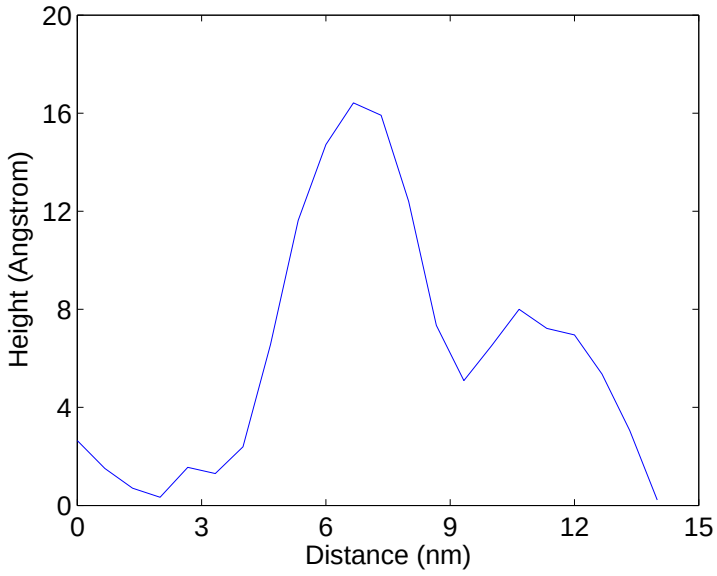

(b)

Figure 16: Tunneling microscopy imaging of Au nanocrystals. (a) Tunneling image of Au nanocrystals on Au/Si substrate at liquid nitrogen temperature. The image shows single isolated nanocrystals of different sizes. Image was taken at $-1.5\,\mathrm{V}$ tip bias and $100\,\mathrm{pA}$ servo set point. (b) A line profile of a single Au nanocrystal (marked with red dashed line in the image). The profile shows a nanocrystal height of about $1.4\,\mathrm{nm}$ and a width of about $5\,\mathrm{nm}$.

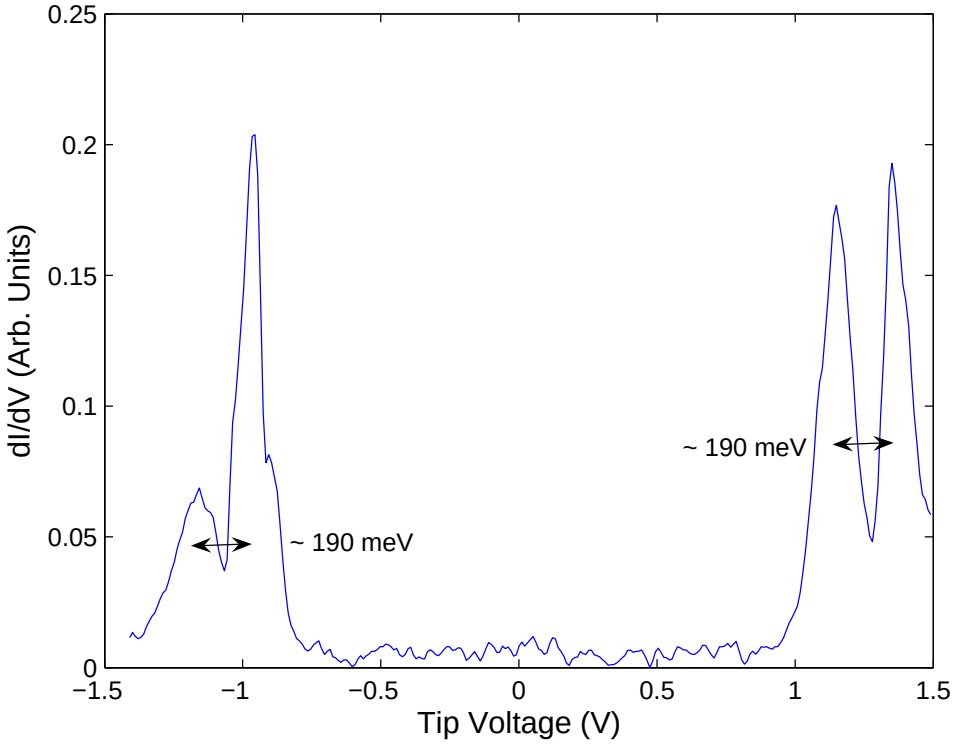

(a)

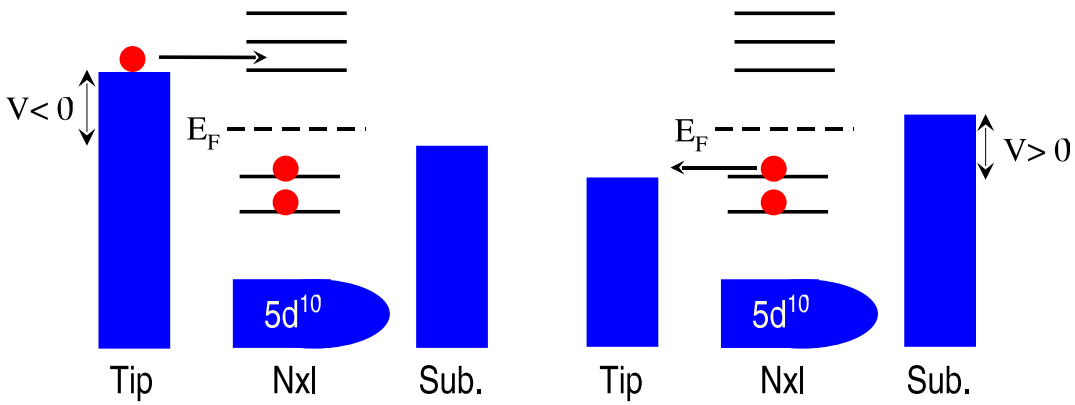

(b)

Figure 17: Tunneling spectroscopy of single 8 kDa nanocrystal. (a) dI/dV on a single nanocrystal. The spectrum is acquired using a lock-in amplifier with the tip voltage modulated at 5 KHz and 50 meV AC signal. The zero current around zero bias voltage corresponds to the sum of charging energy and HOMO-LUMO energy gap. The resolved peaks on the positive voltage side correspond to tunneling from occupied energy states on the nanocrystal. Peaks on the negative voltage side correspond to tunneling into unoccupied states on the nanocrystal. (b) Schematic energy diagram for tunneling through 8 kDa nanocrystal. Tunneling spectrum resolves discrete energy levels above and below the Fermi level.

these nanocrystals was studied in a previous work using atomically flat gold surface on mica [34]. Using a spherical core approximation for nanocrystals shape and the bulk density, the effective core diameter d is obtained from the measured mass M as

$$d[nm] = 0.548 \times (M[kDa])^{1/3}, \tag{34}$$

which allows direct comparison with the STM measured height. The calculated diameter from the measured nanocrystals masses using Equation 34 is overlaid with the STM measured height histogram after offsetting the height axis by -0.36 nm. This way, the major abundance peaks are aligned in the two distributions [34]. This result means that our measured height of about 1.4 nm corresponds to the diameter of the 8 kDa nanocrystal in the mass spectrometry measurements, which is about 1.1 nm. 8 kDa nanocrystals contain about 38 gold atoms and are considered the smallest chemically synthesized, and stable gold nanocrystals [35]. Due to their small size, quantum size effects are expected to be very strong in these nanocrystals.

After imaging, the STM tip is positioned on top of a single nanocrystal, marked by the red dashed line in the image. A lock-in detection set up is then used to acquire dI/dV on this single nanocrystal. The tip voltage was modulated at 5 KHz and 50 meV AC signal. Figure 17(a) illustrates a measured dI/dV spectrum that shows a Coulomb blockade (zero current) of about 1.85 eV around zero bias voltage. The Coulomb blockade is measured as the separation between the first peak on the positive voltage side and the first peak on the negative voltage side and is equal to the charging energy plus the HOMO-LUMO gap. It is not easy to determine the exact value of the HOMO-LUMO energy gap from the tunneling experiments. The large Coulomb blockade indicates that the HOMO-LUMO gap in the 8 kDa nanocrystals is large. Modeling of our experiments shows charging energy of the order of 0.5 eV. Therefore, the HOMO-LUMO gap can be on the order of 1.3 eV [30, 35].

The spectrum in Figure 17(a) also shows two resolved peaks at negative and positive energies, which are separated by about 190 meV. At voltages above the Coulomb blockade threshold, the nanocrystal is charged by one electron. Therefore, as the bias voltage increases, current flows through the system via tunneling into the discrete states. The other

two peaks on the negative side correspond to tunneling into the unoccupied energy levels above the Fermi level on the nanocrystal. The two peaks on the positive voltage correspond to tunneling out of the occupied energy levels below the Fermi level. A schematic diagram of the energy levels and tunneling conditions in a single 8 kDa is shown in Figure 17(b). The completely filled $5d^{10}$ band is located about 1.75 eV below the Fermi level. In each gold atom, there is a free electron in the $6s$ band, which is located below the Fermi level. The separation between this level and the first unoccupied level above the Fermi level represents the HOMO-LUMO gap in these nanocrystals. We believe that the resolved peaks in the dI/dV spectrum correspond to the discrete energy levels above and below the Fermi level.

In the free electron picture of metals, the density of states of a small metal nanocrystal can be described by the discrete particle in a box energy levels, which are determined by the size of the nanocrystal. The density of states of the nanocrystal at E_F can be estimated from the electronic part of the measured heat capacity for bulk gold as $D(E_F) = 0.31\,\mathrm{N/eV}$, where N is the number of atoms. Therefore, assuming spin degenerate energy levels, the average energy spacing is given by $\bar{\delta}(E_F) = 6.5\,\mathrm{eV/N}$. Thus, for the 8 kDa nanocrystal with 38 core atoms, the average energy level spacing is estimated approximately as $\bar{\delta}(E_F) = 170\,\mathrm{meV}$. This estimate is close to our experimentally measured level separation of about 190 meV. 8 kDa nanocrystals have only 38 atoms, and these atoms are expected to be well structured with a high level of symmetry in three dimensional space. The symmetry would stand to increase the average energy level spacing, and therefore the above approximation should be considered as a lower limit on the energy level spacing.

The interpretation of the dI/dV peaks in the 8 kDa nanocrystals spectrum is supported by results from our measurements of the dI/dV for different tunneling parameters. This study (dI/dV at variable tip-nanocrystal separation) is presented in section 3.3 of this chapter. Studies of dI/dV at different tip-nanocrystal separation show that most of the voltage drop in our experiments is at the tip-nanocrystal junction. This implies that at negative or positive voltage the tip-nanocrystal Fermi level difference is larger than the nanocrystal-substrate Fermi level difference. As a consequence, at low negative voltages the unoccupied states on the nanocrystal are accessed by the tip Fermi level, while the

substrate Fermi level is located in the HOMO-LUMO gap. Similarly, at low positive bias voltage, the occupied states are accessed by the tip Fermi level, while the Fermi level of the substrate is located in the HOMO-LUMO gap.

3.3 Variable Tip-Nanocrystal Gap

Tunneling spectroscopy is charge addition, and therefore the density of states are usually entangled with the charging peaks. The separation of the density of states peaks from those due to charging requires more development and refinement of the STS technique. In tunneling spectroscopy experiments, the peak spacing and peak structure depend intrinsically on the parameters of the double barrier tunneling junctions. Therefore, an accurate interpretation of tunneling spectra requires control of these tunneling junction parameters.

As shown in Figure 11, the double barrier junction is realized by positioning the STM tip over the nanocrystal. The nanocrystal is characterized by discrete energy levels with degeneracies reflecting its structural symmetry. The double barrier junction is characterized by a tunneling resistance and a capacitance for each junction. The tunneling rate across each junction is inversely proportional to its resistance. The capacitance and tunneling resistance for the tip-nanocrystal junction (C_1 and R_1) is controlled by changing the tip-nanocrystal distance, usually through the control of the tunneling current settings. In our experiments the tip-nanocrystal distance is controlled through external offset voltages that are applied to the central piezo drive. The applied voltage results in tip extension or retraction for the same tunneling current setting and tip bias voltage. On the other hand, the nanocrystal-substrate junction tunneling parameters (C_2 and R_2) are the same for the specific nanocrystal. They are sample dependent and can be controlled through the choice of the substrate and the attachment mechanisms of nanocrystals to that substrate.

The addition of a single electron to the nanocrystal requires a finite charging energy, E_c, which in the equivalent electric circuit of the double barrier tunneling junction is given by $e^2/2(C_1 + C_2)$. In addition, the capacitance values of the junctions determine the bias voltage division between the junctions as

$$\frac{V_1}{V_2} = \frac{C_2}{C_1}. \tag{35}$$

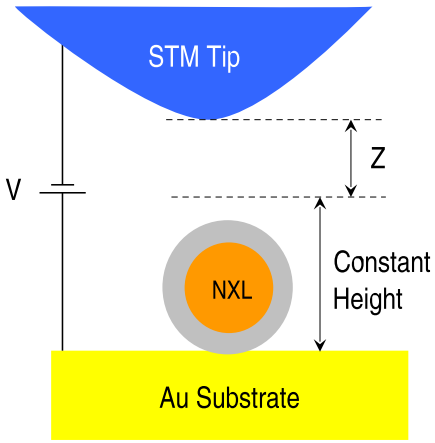

(a)

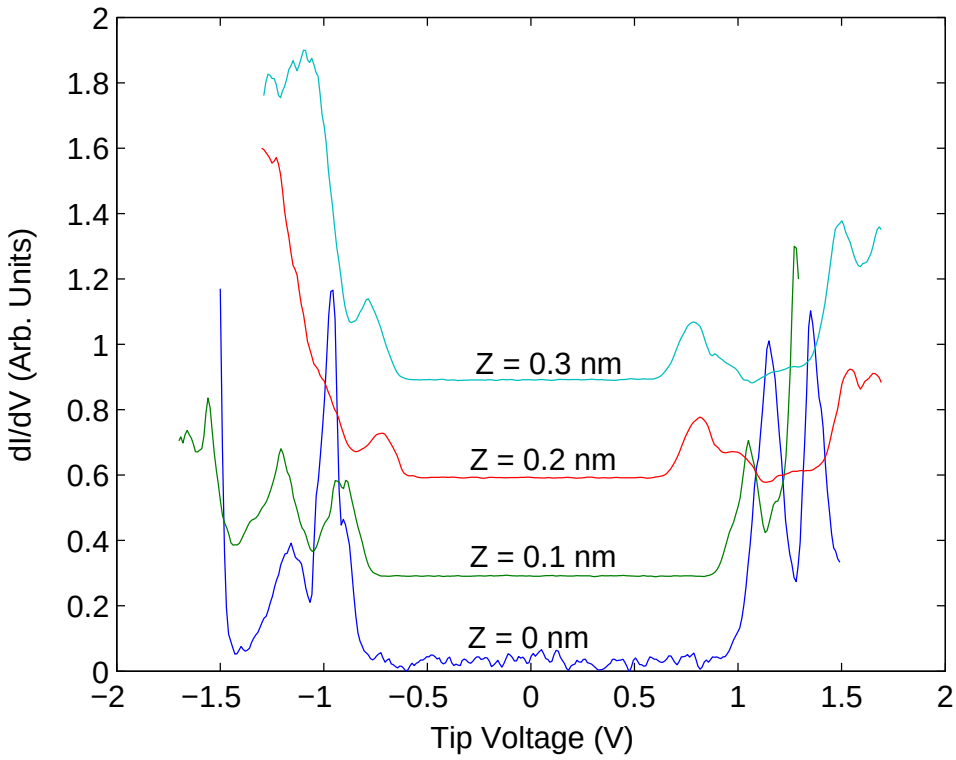

(b)

Figure 18: Tunneling spectroscopy of single nanocrystal at different tip-nanocrystal separation. (a) Schematic diagram of the experiment: the tip is positioned on top of a nanocrystal, the servo is disabled, and the tip is retracted before acquiring the dI/dV spectrum. (b) dI/dV spectra on single nanocrystal is acquired at a different tip-nanocrystal separation. As the tip is retracted, less energy is needed to access energy levels on the nanocrystal.

Because of this voltage division, the experimentally measured spacings between the resonant tunneling peaks in the dI/dV spectrum do not coincide with the real energy level spacings in the nanocrystal. An interesting experimental condition is when the tunneling onset is on junction 1 ($C_1 < C_2$), and at zero bias, the Fermi levels of tip and substrate are aligned in the nanocrystal HOMO-LUMO gap. Applying a bias voltage in this condition aligns the tip Fermi level with the nanocrystal energy levels, while the substrate Fermi level is aligned in the gap. For this tunneling configuration the apparent energy level spacing in the tunneling spectra is larger than the real level spacing by a factor of

$$\frac{V}{V_1} = (1 + \frac{C_1}{C_2}), \tag{36}$$

where V is the total applied voltage between the tip and the substrate, and V_1 is the voltage drop on the tip-nanocrystal junction.

Another important parameter in the double barrier junctions is the ratio between the tunneling resistances, R_1/R_2. This ratio may affect the degree of the nanocrystal charging during the tunneling process through the junctions. When R_1 is much less than R_2, an electron tunneling from the tip to the nanocrystal would escape to the substrate before the next electron could tunnel into the nanocrystal. Consequently, resonant tunneling through the nanocrystal energy levels without extra charging will take place. On the other hand, when R_1 is on the order of R_2, charging effects start to become significant.

Figure 18(a) shows a schematic of our experiments for measuring dI/dV spectrum at different tip-nanocrystal separation. The tip is positioned on top of a single nanocrystal, and the servo is disabled in order to maintain a constant tip-substrate separation. The first dI/dV is acquired at this constant separation. The tip then is further retracted by applying an offset voltage on the central piezo. Figure 18(b) shows four dI/dV spectra that are taken at different tip-nanocrystal separations. The spectra are taken at 0, 1, 2, and 3 Å tip-nanocrystal offset. The figure shows an interesting trend where the apparent Coulomb blockade gap (zero current) decreases as the tip is retracted. The tip retraction results in a decrease in the tip-nanocrystal capacitance, C_1. This experimental study can be used to determine which junction capacitance is larger. The charging energy of the

system [$E_c = e^2/2(C_1 + C_2)$] is inversely proportional to both C_1 and C_2. Thus if $C_1 > C_2$ (therefore has more weight in E_c) then a decrease in C_1 should result in an increase in E_c and consequently larger Coulomb blockade. The observed trend shows a decrease in the apparent Coulomb blockade as C_1 is reduced. This implies that C_1 is much smaller than C_2, and therefore its reduction does not change E_c, since E_c mainly is determined by the value of C_2. Thus in our experimental configuration C_1 is smaller than C_2, and the applied bias voltage largely drops on the tip-nanocrystal junction. Tunneling through the nanocrystal energy levels is onset in this junction. Hence, the apparent energy level spacing is larger than the real energy level spacing by a factor of $V/V_1 = (1 + C_1/C_2)$. When C_1 is reduced through tip retraction, the nanocrystal energy levels become accessable at less bias voltage; and therefore, the apparent Coulomb blockade gap decreases.

The above experimental conclusion is important for the interpretation of our measurements of electron dynamics in single nanocrystal. These measurements are performed using a new technique developed in our lab and is presented in chapter IV. The fact that in our experimental configuration most of the voltage drop is on the tip-nanocrystal junction implies that the first tunneling event corresponds to electron charging of the nanocrystal. In this case electron relaxations mechanisms are not mediated by electron-hole interactions. Holes are present in the nanocrystal if the first tunneling event corresponds to electron discharg from the nanocrystal.

3.4 Time Evolution of dI/dV Spectra

The implementation of both phase sensitive detection technique and long sampling time have enabled us to acquire STS data with high signal to noise ratio. Our STS data was taken at liquid nitrogen temperature. At such low temperature the microscope is stable thermally. Because of the stability of the tip-nanocrystal junction, spectra can be recorded over long period of time. The thermal stability also allows us to study the evolution of STS spectra over time. This time evolution can reveal valuable information about the dynamics of the nanocrystal environment. As mentioned previously, our nanocrystals were chemically attached to the gold substrate. This implies that nanocrystals can still move as a result of

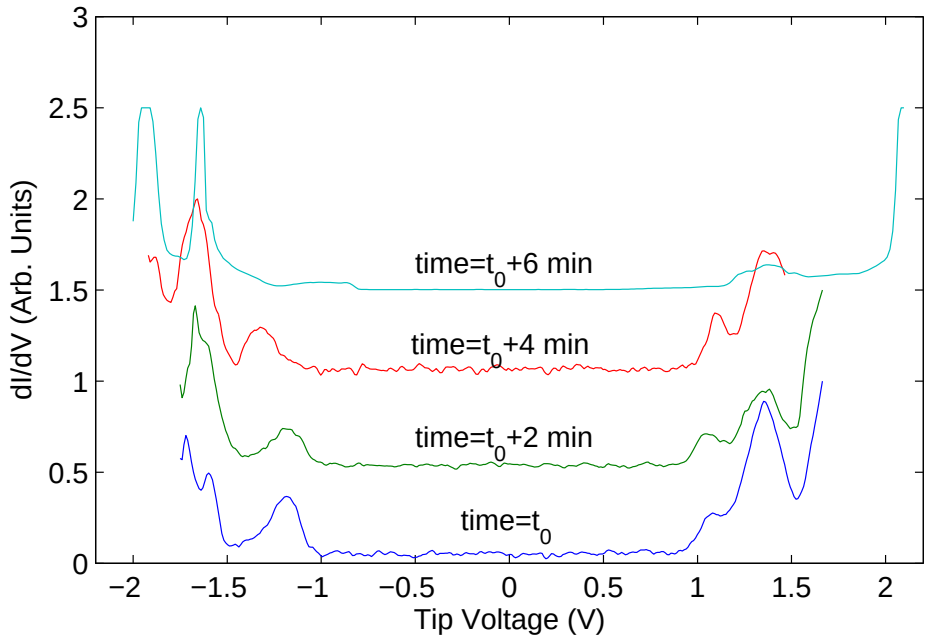

Figure 19: Time dependent of dI/dV spectra. The spectra were acquired on a single isolated nanocrystal. The time difference between each spectrum is about two minutes. The STM tip was re-servoed after the acquisition of each spectrum. The Coulomb blockade gap, peaks positions, and peaks widths are changing as a function of time.

their interaction with the tip. If the motion is small, then it appears as streaks in image. On the other hand, if the motion is large, then it results in nanocrystals disappearance. This motion is expected to be stronger during spectroscopic measurements, since the tip is positioned on the nanocrystal for long times and relatively larger voltages than the tunneling voltage are used.

Figure 19 shows four dI/dV spectra that are taken at 2 minute intervals. The data shows that both the Coulomb blockade and peaks in the spectrum change over time. The spectra appear to evolve to a slightly new form over short times. The width of the Coulomb blockade changes from about -2 eV to about 2.5 eV as time evolves from the first to the last spectrum. However, Coulomb blockade is almost the same for the first three spectra. This change in Coulomb blockade does not seem to follow a specified trend, and therefore is due to random changes in the nanocrystal environment. The widths and positions of the dI/dV peaks are also evolving over time. For example, the second peak on the negative side voltage of the first spectrum has a doublet. This doublet becomes weaker in the second

spectrum and disappears completely in both the third and fourth spectrum. In addition the intensity of the first peak on the negative voltage side decreases with time until it is suppressed completely in the fourth spectrum. The peaks on the positive voltage side seem to preserve their intensity and relative separation over the time evolution of the first three spectra. However, these peaks experience dramatic change in the intensity in the fourth spectrum. The disappearance of some of the dI/dV peaks is related to the widening of the Coulomb blockade, since tunneling through states within the Coulomb blockade gap becomes energetically unfavorable.

The change in Coulomb blockade width is explained by changing either the capacitance ratio or the effective partial charging of the nanocrystal, or both of them. This change in the tunneling geometry can be due to random tip drift. The drift can bring the tip over a region of different symmetry on the nanocrystal resulting in a change in the spectrum. Nanocrystal motion is another possible source of geometric change in the tunneling junction. While we have shown in chapter 2 that the nanocrystals are chemically attached to the gold surface, small motions of nanocrystals are observed in our experiments.

CHAPTER IV

BEES ON SINGLE NANOCRYSTALS

The currently available spectroscopic techniques provide limited information about electron dynamics in a single nanocrystal. As shown in the previous chapter, STS is a very powerful technique for studying energy level structures in single nanocrystals. However, information about the electron dynamics in these studies is limited. On the other hand, combined frequency- and time-resolved optical methods are extensively used to study both energy level structures and hot electron dynamics in nanocrystals. However, these studies are usually performed on ensembles of nanocrystals, where size distributions and solvent impurities significantly affect the measurements. Moreover, optical measurements can only probe the dipole-allowed electronic transitions. Given these limitations on the currently used techniques, new methods that combine both single nanocrystal addressability as well as electron dynamics investigations need to be developed for better understanding of the size-dependent properties in both metals and semiconductors. This chapter introduces a new experimental approach for studying the electron dynamics at the single nanocrystal level. This approach is based on Ballistic Electron Emission Spectroscopy (BEES), a three terminal extension of STS, initially developed for studying Schottky interfaces and buried structures. The basics of BEES are introduced at the beginning of this chapter followed by a detailed description of its implementation for single nanocrystal characterization.

4.1 Metal-Semiconductor Contacts

When clean metal and semiconductor surfaces are brought into contact at the atomic scale, under equilibrium conditions, their Fermi level is invariant with position. Consequently a short time after the conceptual contact formation, electrons are transferred between the semiconductor and the metal. For n-type semiconductor and typical metals, the net loss of electrons from the semiconductor creates a surface depletion region and a growing barrier to

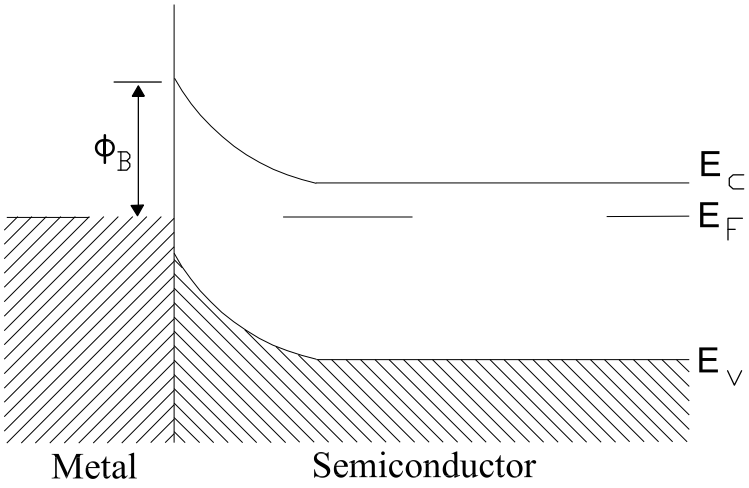

Figure 20: Energy band diagram for ideal metal n-type semiconductor contact.

electron transfer from the semiconductor to the metal. This continues until the transfer rate is the same on both sides, and E_F is the same throughout the structure. The equilibrium energy band diagram for an ideal metal to n-type semiconductor is shown in Figure 20. The surface potential energy barrier encountered by electrons with $E = E_F$ at the metal semiconductor interface is called the Schottky barrier [36]. In Schottky original model the barrier is given by

$$\Phi_B = \Phi_m - \chi, \tag{37}$$

where Φ_m is the work function of the metal, and χ is the semiconductor electron affinity. Real Schottky barriers also depend on the interface states [37], but a simplified model is sufficient for the present purpose.

When $V > 0$ is applied to the metal, the voltage reduces the barrier seen by electrons in the semiconductor to the metal and therefore permits a net flow of electrons from the semiconductor to the metal. Increasing the voltage leads to a rapidly rising forward current. On the other hand, applying $V < 0$ voltage to the metal side shifts E_F in the metal above E_F in the semiconductor, and therefore the current flow from the semiconductor to the metal is blocked. This is a rectifying current-voltage characteristic that is similar to that displayed by a *pn* junction diode.

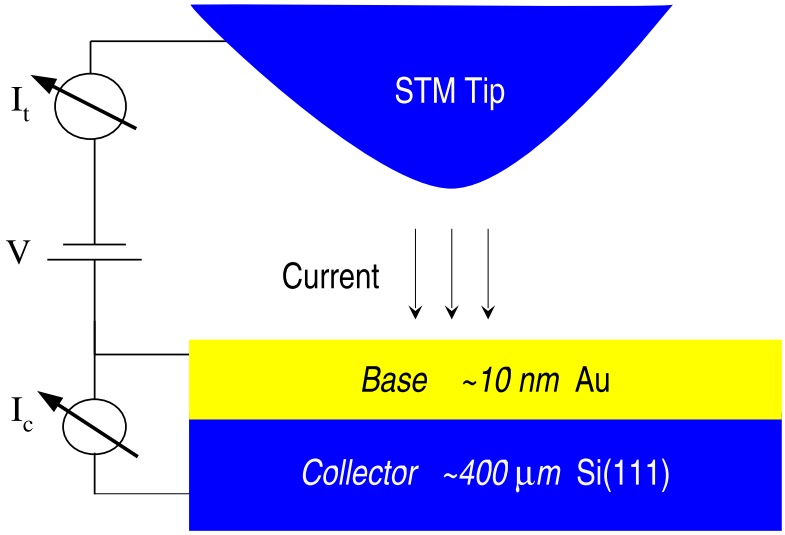

Figure 21: Schematic of an STM/BEES system. Electrons are injected into the base at either a constant current or constant tip-substrate separation. The tunneling current is measured at the grounded sample base layer (gold film) through a current amplifier. The transmitted current into the semiconductor collector is measured by a virtual ground current amplifier.

4.2 Introduction to BEES

Ballistic Electron Emission Spectroscopy (BEES) was developed by Bell and Kaiser in 1988 [38]. BEES utilizes an STM system in a three-electrode configuration, allows for the characterization of interface properties with nanometer spatial resolution, and enables an energy spectroscopy of carrier transport. BEES employs an STM tip for injection of ballistic electrons into the sample under investigation. Usually the sample consists of at least two layers separated by an interface of interest. BEES operates as a three electrode system as shown in Figure 21, with electrical contact to each layer of the sample surface. Figure 22 shows the corresponding energy diagram of tip, base, and collector for the case of a metal-semiconductor Schottky barrier system. In this system, the metal layer serves as a biasing electrode, and the semiconductor functions as a collector of ballistic electron current.

When a bias voltage is applied between tip and base, electrons tunnel through the vacuum gap and enter the metal layer as hot carriers. For tunnel voltages less than the interface barrier height, none of the injected electrons has total energy equal to or larger than the barrier height, and the measured collector current is zero. As the voltage is increased to

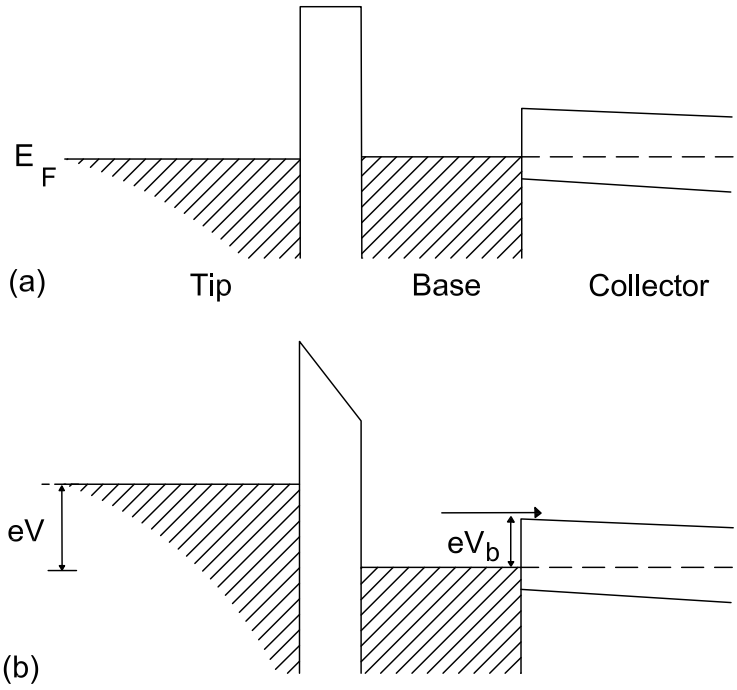

Figure 22: Energy diagram for BEES of a metal base-semiconductor collector Schottky barrier system. (a) Energy diagram for zero applied voltage. (b) For applied voltage (V) larger than the interface barrier height (V_b), some of the injected electron from the tip would have sufficient energy to cross enter the semiconductor.

values in excess of the barrier, i.e., $eV \geq E_F + eV_b$, some of the hot electrons cross the interface into the semiconductor conduction band, and a collector current is observed. A typical thickness for the base layer is on the order of 10 nm, therefore, electrons may propagate through the base layer and reach the interface before scattering. In BEES experiments, an n-type semiconductor is used typically for electron collection, since band bending pushes the collected electrons away from the interface and prevents their leakage back into the base. By varying the voltage between tip and base, the energy of hot carriers can be controlled, and spectroscopy of interface carrier transmission may be performed. The location of the threshold in the spectrum defines the interface barrier height. The magnitude of the current above threshold and the threshold spectrum shape also reveal important information about interface properties.

4.3 Theory of BEES

This section describes a simple theoretical model developed by Kaiser and Bell to describe the physics of BEES [39] (note that Gauthrie, et al., have published a more detailed description [40]). The model treats sequentially the processes of vacuum tunneling, base layer transport, and interface transport. The effective mass approximation is used for each of these processes. The metal semiconductor interface is simplified by a smooth interface that dictates the conservation of the component of the electron wave vector parallel to the interface k_t. Total energy conservation across the interface provides another constraint on the electron transport.

A particle incident on a simple potential step, with total energy in excess of the step height, loses a portion of its kinetic energy as it crosses the step, due to reduction in k_x, the component of $\vec{\mathbf{k}}$ normal to the interface. For incidence with nonezero angle to the normal, conservation of k_t requires that $\vec{\mathbf{k}}$ changes across the interface, i.e., the particle is refracted. If the angle of incidence is larger than a critical angle, θ_c, the particles are not able to cross the interface and are reflected back. This critical angle is given by [41]

$$\sin^2\ \theta_c = \frac{E - E_0}{E}, \tag{38}$$

where the particle total energy is E, and the step height is $E_0 = E_F + eV_b$. For real band structure and for two materials with different dispersion relations, the normal and parallel components of the energy are no longer separable. A change in the electron effective mass or in the location of the conduction band minima within the Brillouin zone, changes the conditions for the critical angle.

As an approximation, zone-centered conduction band minima for both the metals and the semiconductor are assumed. For an evaporated metal base layer, which is polycrystalline, the approximation of an isotropic free-electron mass for the base can be made [38]. The critical angle then is defined with respect to the interface normal as

$$\sin^2\ \theta_c = \frac{m_t}{m}\frac{e(V - V_b)}{E_F + eV}, \tag{39}$$

where m is the free electron mass. For Si(100) with small component parallel to the interface and for $e(V - V_b) = 0.3\,eV$, the critical angle is less than 6 degrees. Since only electrons

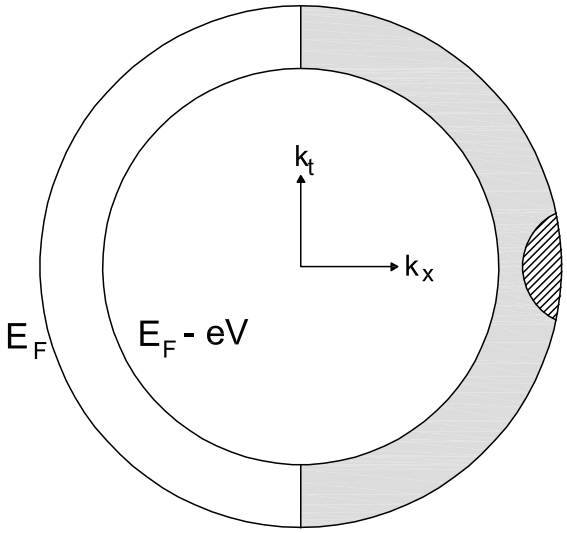

Figure 23: Diagram of **k**-space representing the free electron Fermi sphere of the metal STM tip. The diagram shows the case of electrons tunneling from tip to substrate. For an applied bias voltage between tip and sample, electrons occupying states within the shell determined by E_F and $E_F - eV$, and $k_x > 0$, can tunnel. These states are shown in grey. For $eV > eV_b$, a subset of these tunneling electrons, are defined by a hyperboloid in **k**-space and satisfy phase space requirements for collection in the semiconductor. These states are shown by diagonal lines in the figure.

incident on the interface at small angles can be collected, critical angle reflection at the interface results in high spatial resolution in BEES measurements. For a 10 nm thick base layer, around 2 nm spatial resolution is expected for BEES.

Electron tunneling from the STM tip into the base layer is treated using a planar tunneling formalism [42]. This description provides simple analytic expressions for the (E, $\mathbf{k}$) distribution of the tunneling electrons and for the total tunnel current. Current across the metal semiconductor interface (BEES current) is then calculated from this initial distribution by considering the fraction of the total tunneling current, which is within the cone formed by the critical angle. Using the WKB approximation, the tunneling probability $D(E_x)$ is given by [43]

$$D(E_x) = \exp\left(-2\int k_x \, dx\right). \tag{40}$$

The vacuum barrier is assumed to be square at $V = 0$, with height Φ measured relative to the Fermi level, the tunneling probability then becomes

$$D(E_x) = \exp\left(-\alpha \, s \, \frac{2}{3\,eV}\left[(E_F + \Phi - eV - E_x)^{3/2} - (E_F + \Phi - E_x)^{3/2}\right]\right), \tag{41}$$

where $\alpha = (8m/\hbar^2)^{1/2} = 1.024\, eV^{-1/2}$. With $\bar{\Phi} = \Phi - eV/2$ for the square barrier, the tunneling is approximated as

$$D(E_x) \approx exp\left(-\alpha s \left(E_F + \bar{\Phi} - E_x\right)^{1/2}\right). \tag{42}$$

Tunneling current in terms of the integrals over E_x and E_t is then given by the expression

$$I_t = C \int_0^\infty dE_x\, D(E_x) \int_0^\infty dE_t \left(f(E) - f(E + eV)\right). \tag{43}$$

The integration is over all tip states with $E_x > 0$, and $C = 4\pi mae/h^3$. E_x is the energy associated with k_x, and E_t is the energy associated with k_t. In this model for the tunneling current, the tip and base are taken to be identical free-electron metals. Figure 23 shows the states that contribute to tunneling from the tip. These states occupy a half-shell within the tip Fermi sphere between $E = E_F + eV$ and $E = E_F$.

An expression similar to the tunneling current can be derived for the BEES current, with the allowed phase space in the tip determined by the critical angle conditions at the interface. For the case of m_t less than m, the restrictions on the tip states are

$$E_t \leq \frac{m_t}{m - m_t} \left[E_x - E_F + e\left(V - V_b\right)\right], \tag{44}$$

$$E_x \geq E_F - e\left(V - V_b\right). \tag{45}$$

If the equalities in the above equations are taken as limits, the collector current can be expressed as

$$I_c = R\, C \int_{E_x^{min}}^\infty dE_x\, T(E)\, D(E_x) \int_0^{E_t^{max}} dE_t \left(f(E) - f(E + eV)\right), \tag{46}$$

where R is a measure of attenuation due to scattering in the base layer, which is taken to be energy-independent for these energies. $T(E)$ is the transmission coefficient across the metal/semiconductor interface. For $eV_b \gg k_B T$, the second Fermi function $f(E + eV)$ may be neglected, and the integral can be evaluated analytically. At very low temperatures and for voltage near threshold, the BEES current can be approximated by

$$I_c \propto \left(V - V_b\right)^{5/2}. \tag{47}$$

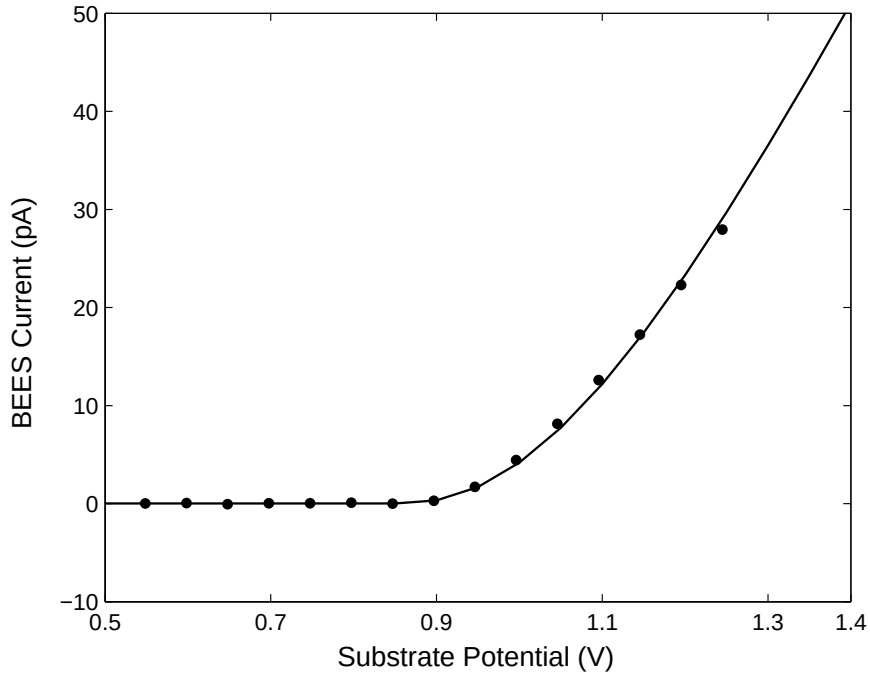

Figure 24: BEES spectrum (circles) acquired on Au/n-Si(111) sample. Figure also shows a fit (line) to the data using the proposed model for BEES (Equation 48). Values of $\Phi = 3\,\mathrm{eV}$ and $s = 10\,\text{Å}$ are used in modeling the tunnel barrier.

BEES spectra are usually obtained with STM operating at a constant tunneling current mode, which normalizes the BEES current to the tunneling current. BEES current formula contains a factor of s, tip sample separation, which changes with tunnel voltage at constant current. Therefore, the calculated BEES current should include the change in current due to the change in s. This can be done by treating s as a constant s_0, and normalizing $I_c(s_0, V)$ by $I_t(s_0, V)$ for each voltage value. This is an exact normalization if both I_c and I_t are measured at constant s. The expression for I_c then takes the form

$$I_c = R\, I_{t0}\, \frac{\int_{E_x^{min}}^{\infty} dE_x\, D(E_x) \int_0^{E_t^{max}} dE_t\, T(E)\, [f(E) - f(E + eV)]}{\int_0^{\infty} dE_x\, D(E_x) \int_0^{\infty} dE_t\, [f(E) - f(E + eV)]}. \tag{48}$$

The above formula is a good fit to experimental data. An experimental BEES spectrum from Au/Si(111) at liquid nitrogen temperature is shown in Figure 24 with a numerical fit using Equation 48.

4.4 Experimental Details

In this section, some of the modifications and newly designed features introduced to the low temperature STM are described. The modifications are needed in order to optimize the system's operation. The new design features are introduced in order to allow BEES capabilities in our system. These new features include the design of a new sample holder, the redesign of the sample jig, and details of sample preparation for an optimized signal to noise ratio.

4.4.1 General Considerations

In order to perform BEES experiments with an STM instrument, three additional requirements have to be satisfied: The semiconductor and the metal film have to be contacted separately; the collector current, i.e., the BEES current, has to be measured; and the tunneling current has to be measured. In our system, the collector current is measured at the back of the sample holder by forming an Ohmic contact between the silicon substrate and the metal holder. The Ohmic contact is formed by scraping the back of the silicon chip with a sharp diamond tip and depositing a thin layer of indium onto it. The indium is therefore sandwiched between the back of the silicon and the sample holder, and establishes a good electrical contact. Since BEES current level is about 2 percent of the tunneling current, good electrical performance is required to allow BEES current measurements with a noise level of less than 1 pA. This is achieved by reasonable electrical shielding and by positioning the current amplifiers as close as possible to the sample in order to minimize noise pick up on the signal carrying cables.

Special care is taken in the mechanical design when using the STM for BEES measurements. STM systems are designed to have sufficient vibration isolation to obtain a mechanical noise level of less than 0.1 Å for atomic resolution. This noise level is required for BEES experiments. As shown in chapter 2, for example, a difference in tip-sample separation of 1 Å results in an order of magnitude change in the tunneling current. This also results in a corresponding noise level in the BEES current. In addition, thermal drift velocities have to be as small as possible in order to allow enough time for acquisition of a

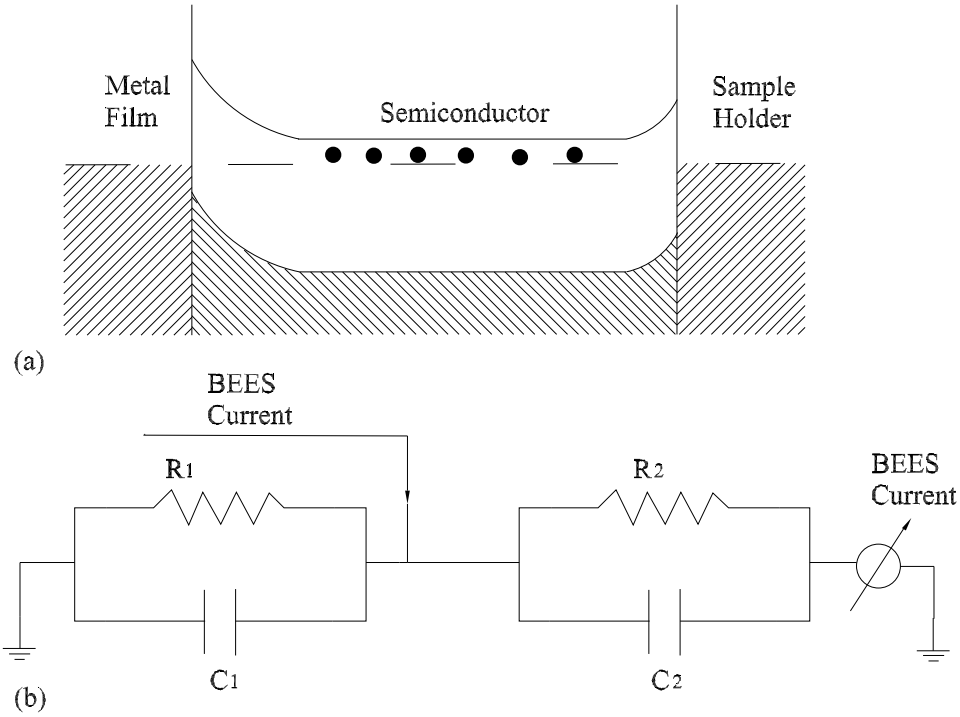

Figure 25: (a) Energy diagram of BEES sample used in our experiment. Dashed line represents the Fermi energy level. (b) Corresponding electrical circuit of the BEES sample.

spectrum at a fixed tip-sample separation. All of our BEES experiments are performed at liquid nitrogen temperatures. The use of lower temperature has several advantages: BEES current noise is significantly reduced because thermal current fluctuations are absent, and less thermal drift is observed because of lower thermal expansion coefficients and better temperature stability. On the other hand, boiling liquid nitrogen introduces mechanical vibration that can contribute to the noise. Low temperature operation increases significantly the metal/semiconductor resistance R_1, and the back contact resistance R_2, shown schematically in Figure 25(b). That increase in resistance would increase the corresponding time constants, which then may require reduced measurement speed.

4.4.2 Design Criteria of the Sample

BEES currents are usually small, on the pA range, therefore for good signal to noise ratio, the BEES sample is designed with some technical considerations. In addition to the pick up noise from outside sources, voltages applied on the BEES sample result in substantial current noise since the sample has finite resistance. The sources of these voltages can be

current amplifiers or contact potential changes due to thermal variations during cooling down. The best current amplifiers now available have an input voltage-noise of the order of $60\,\mathrm{nVHz}^{-1/2}$. A typical time constant for the low pass filter on the BEES current amplifier is about $0.1s$. This time constant corresponds to a band width above 1.6 Hz. Therefore, an input voltage of at least 100 nV results from the input voltage-noise on the amplifier. The contact potential changes are known to generate sudden voltage jumps of the order of $1\,\mu$V. Thus for the BEES current noise to be below 1 pA, the sample resistivity should be well above $1\,\mathrm{M}\Omega$.

The Schottky diode behavior is well described by thermionic emission theory. The current I through the junction of a metal with an n-type semiconductor is given [44, 45] as

$$I = \left[(4\pi\, m_c\, e\, (k_B T)^2 A)/h^3\right] \exp(-\Phi_B/k_B T)[\exp(eV/k_B T) - 1], \tag{49}$$

where A is the area of the junction, m_c is the effective mass at the conduction band minimum (CBM) of the semiconductor, Φ_B is the Schottky barrier height, and V is the voltage applied to the junction. The resistivity of the diode at $V = 0$, which represents the condition during the current measurements, is then given by the derivative of the current with respect to voltage at $V = 0$,

$$R_0 = (dI/dV|_{V=0})^{-1} = [h^3/(4\pi m_s e^2 k_B T A)]\ \exp(\Phi_B/k_B T). \tag{50}$$

Our n-type Si Schottky diode is roughly described with the following parameters: $\Phi_B = 0.85\,\mathrm{eV}$, $A = 12\,\mathrm{mm}^2$, $T = 300\,\mathrm{K}$, and $m_s = 0.3m$, where m is the free electron mass. A simple estimation of the resistance of this diode is $R_0 = 33\,\mathrm{k}\Omega$. This resistance results in a noise level of the order of few μA, which is larger than the BEES current signal. For this reason, our BEES experiments were all performed at 77 K, liquid nitrogen temperatures. At 77 K, the estimated resistance of our samples is on the order of several hundred $M\,\Omega$. The corresponding noise level in our experiments is therefore about 0.1 pA. In addition, the value of R_0 is significantly reduced by leakage currents at the edges of the metal film or at other low-barrier areas of the metal/semiconductor interface.

The back contact is another constraint on the BEES sample. The back contact should be a good Ohmic contact, i.e., a Schottky diode with a very low barrier height to yield low

R_0. Figure 25(a) shows an energy schematic diagram of the sample. Figure 25(b) shows the corresponding electrical circuit in the BEES experiment. The metal/semiconductor interface is characterized by R_1 and C_1 and the back contact by R_2 and C_2. In the shown electric circuit representation, the incoming ballistic current I_c feeds into the semiconductor (between the contacts), and it flows to ground either via the metal/semiconductor interface (R_1) or the back contact (R_2). Since we are detecting the BEES current at the back of the semiconductor, a correct measurement of I_c requires that $R_1 \gg R_2$, otherwise the BEES current is significantly reduced or not detected at all.

In BEES experiments, electrons are transported ballistically through the metal film layer so that they reach the metal/semiconductor interface with the same energy. Therefore, the metal film thickness should be very small to avoid inelastic scattering of the hot electrons. For noble metals, a film thickness of the order of 100 Å would equal the electron's mean free path. If the film thickness is too thin, then it may not form a metallic film or it may consist of clusters on the surface. For films that are too thin, local charging might appear because of poor contact between the film surface and BEES electrode. The resistance along the metal film is small compared to the tunnel resistance, which is about 1 GΩ at $V_T \cong 1\,\mathrm{V}$ and $I_t \cong 1\,\mathrm{nA}$, in order to prevent charging effect.

4.4.3 Sample Holder Design

In order for the STM system to be used for measuring BEES spectra, the sample holder was redesigned. Figure 26 shows a picture of the BEES sample and its holder. The holder is made by cutting out a quadrant of stainless steel disk. The quadrant then is attached back to its original position with nonconductive epoxy. Thus, the new disk will consist of two electrically isolated pieces. Our BEES sample consists of a 4 mm diameter gold film deposited on top of 7 mm × 7 mm silicon chip. For BEES studies, the silicon chip is mounted on the sample holder so that both tunneling and BEES currents are measured simultaneously. The chip is mounted on the BEES sample holder by two fingers that are spot welded to one side of the holder. BEES current is collected at the back of the silicon chip. For Ohmic contact formation between the silicon chip and sample holder, the back of

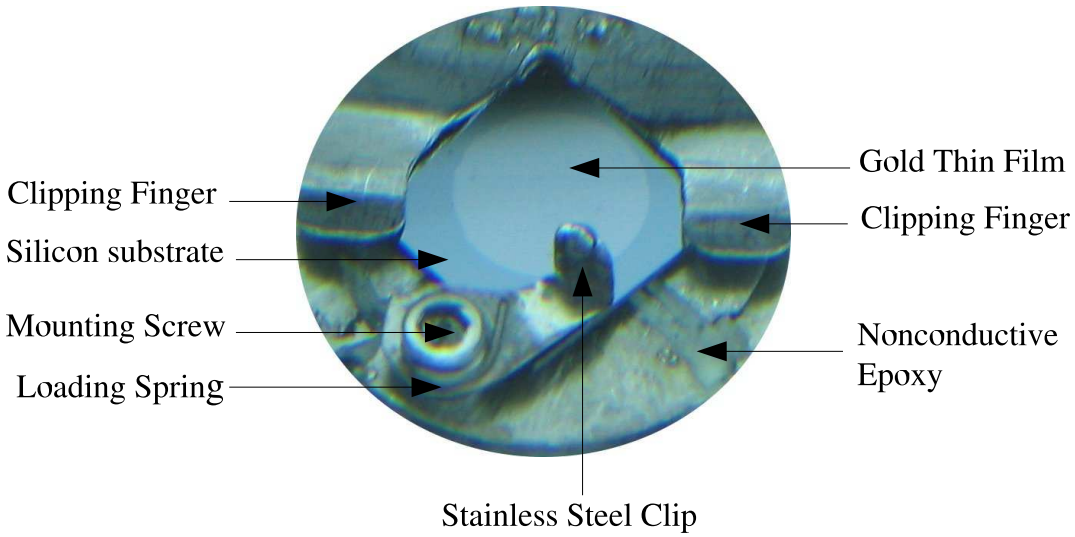

Figure 26: BEES sample and its holder. BEES sample consists of a 10 nm gold film deposited on Si(111) substrate. Sample is mounted on the holder by two finger clips. The silicon forms Ohmic contact with the one part of holder through a layer of indium for BEES current. The gold film is electrically connected to the other holder part through a clip for tunneling current measurements.

the silicon chip is scraped by a diamond scraper, and a thin layer of indium is deposited. The tunneling current is measured as usual at the surface of the gold thin film. Since the gold film is very thin (10 nm) a fine spring-loaded stainless steel clip with little downward force is used to establish the electrical contact with the gold film. The clip is hook-shaped in order to minimize its conact with the gold and is loaded with a spring from the top.

4.5 BEES on Single Nanocrystals

As mentioned in the beginning of this chapter, BEES has been developed to study buried interfaces, since it measures electrons that are transmitted through interfaces. This section introduces a new application of BEES in single nanocrystal characterizations. Narayanamurti's group previously reported on the use of BEES to study electron transport through InAs quantum dots [46]. In their approach, InAs quantum dots were grown epitaxially within a GaAs matrix, where the difference in bandgap will result in electron confinement in the InAs region. This process results in 30 nm diameter and 3 nm high quantum dots. To form the Schottky barrier a 10 nm thick gold layer was evaporated on the top of the GaAs matrix, where the dots are buried. Therefore, the quantum dot is buried spatially beneath

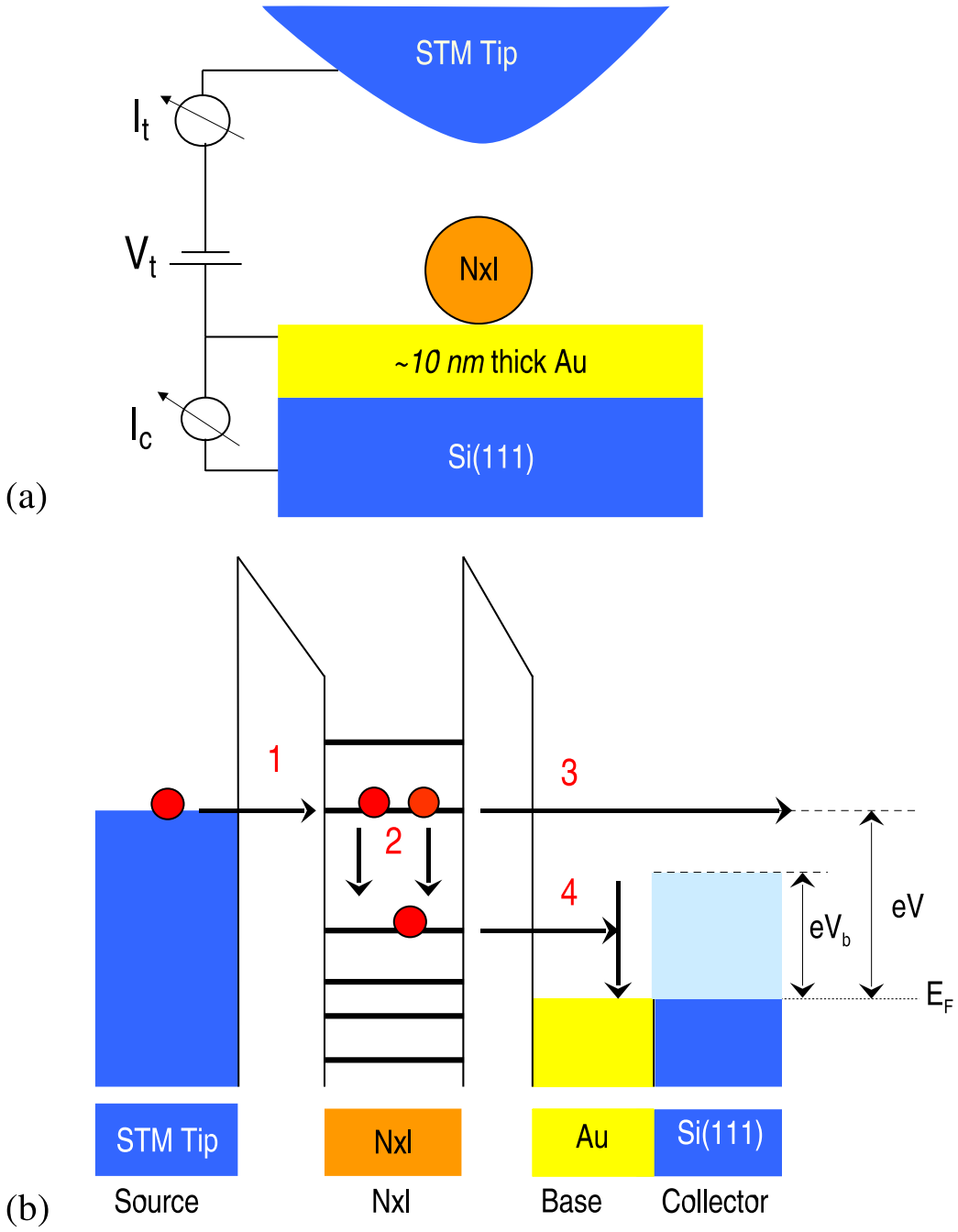

Figure 27: Schematic diagram of BEES measurements on a single nanocrystal. (a) Nanocrystals are chemically attached to a thin gold film that is deposited on Si(111) substrate. A sharp STM tip is brought in tunneling range, and electrons tunnel from tip into the gold film through the nanocrystal. Tunneling current is measured between the STM tip and the gold film, and BEES current is collected at the back of the Si(111) substrate. (b) A schematic energy diagram of BEES on single nanocrystal. (1) Electrons are injected into the nanocrystals excited states at a constant rate. (2) After their injection, electrons may relax into a lower energy level inside the nanocrystal by losing some energy . (3) Electrons may tunnel out without suffering energy loss. (4) After relaxation, electrons may not have enough energy to overcome the Schottky barrier at the metal semiconductor interface.

the metal/semiconductor interface. In this configuration, BEES measurements provide information about conduction band offset, resonant tunneling through the quantized states of the quantum dot, and their energy separation. However, in this approach, the strain induced by the matrix on the quantum dots has been found to affect the transport measurements. Furthermore, due to the spatial location of the quantum dots with respect to the Schottky barrier, electron dynamics and lifetimes of hot electrons can not be experimentally measured.

In our approach, nanocrystals are chemically deposited from solution onto the surface of a very thin SAM coated gold film. Therefore, nanocrystals are isolated from each other and separated from the substrate by an organic layer, which forms a tunneling gap. This configuration does not result in any strain on the nanocrystal. Moreover, it allows for studying and controlling the effect of tunneling parameters on nanocrystal transport properties. A schematic diagram of the experimental set up of BEES on a single nanocrystal is shown in Figure 27(a). A voltage is applied between the STM tip and the thin gold film, which is deposited on the top of Si(111) substrate. After that, the tip is brought into the tunneling range through careful approach. After tunneling is achieved, the sample surface is scanned using regular STM technique in order to identify nanocrystals on the surface. After imaging, the tip is positioned on a nanocrystal of interest, and both tunneling IV and BEES IV are captured at either constant current or constant tip-sample separation. As shown in Figure 27(a), the tunneling I_t is measured between the tip and the gold film, while, BEES I_c is measured at the back of the silicon substrate. A schematic energy diagram of BEES on single nanocrystal is shown in Figure 27(b). Electrons are injected into the excited states of a nanocrystal at a constant rate (step one in the diagram). After their injection, electrons may relax to a lower energy state by losing some of their energy (step two in the diagram), or they may tunnel out directly from their injection state (step three in the diagram) without energy loss. We expect to detect BEES current whenever electrons tunnel out with energy high enough to pass the Schottky barrier. This event takes place even after energy relaxation in the nanocrystal. If electrons experience inelastic scattering in the nanocrystal and relax to an energy below the Schottky barrier, we expect to detect

no current at the collector (zero BEES current). The BEES spectrum on the nanocrystal therefore represents an energy distribution of electrons tunneling out from the nanocrystals states. When compared with BEES on the substrate, this energy distribution provides significant information about electron dynamics within a single nanocrystal. It also provides a new experimental measure of hot-electron lifetimes in a single nanocrystal, as we present in Sections 4.6 and 4.7.

BEES measurements in our experiments are taken at constant tunneling current. As mentioned in chapter 3, tunneling spectroscopy on our single nanocrystal samples is a double barrier tunneling junction. The first junction is formed by STM tip-nanocrystal, and the second junction is formed by nanocrystal-substrate. The total applied voltage bias is divided between these two junctions, and the division is determined by their capacitive coupling. The relative values of the voltage divisions are given by $V_1/V_2 = C_2/C_1$, where C_1 is the tip-nanocrystal capacitance, C_2 is the nanocrystal substrate capacitance, and $V1$ and V_2 are the corresponding voltage values. During STS measurements, the servo feedback is disabled; therefore, the tip substrate distance is held fixed, and the increase in tunneling current corresponds to an increase in the number of current carrying channels on the nanocrystal. The capacitive coupling between the nanocrystal and tip depends on their separation, therefore, during tunneling spectroscopy the capacitive coupling is assumed to be constant unless the nanocrystal moves due to some changes in its environment. On the other hand, when constant current is maintained (BEES spectroscopy case) and the tip voltage is swept, the servo retracts the tip in order to maintan a constant current. This retraction increases tip-nanocrystal separation that results in a decrease in the tip-nanocrystal capacitive coupling. The decrease in capacitance leads to an increase in the voltage drop across the tip-nanocrystal junction.

The change in voltage division across the tunneling junctions during BEES current acquisition has some effect on the measured electron dynamics and its interpretation. As mentioned in chapter three of this thesis, the capacitive coupling determines the voltage division on the tunneling junctions and hence the tunneling current onset. For example when a negative voltage is applied to the tip, if the voltage drop across tip-nanocrystal

junction is larger than that across nanocrystal-substrate junction, then the first tunneling event corresponds to charging of the nanocrystal through the transfer of an electron from the tip to the nanocrystal. In this tunneling configuration, if hot electrons relax inside the nanocrystal, then the relaxation mechanism is something other than electron-hole Coulomb interaction. For example it can be electron-phonon coupling or electron-surface scattering. This experimental tunneling configuration is an ideal test for the effect of Coulomb interaction on hot electron relaxations in three dimensionally confined structures. On the other hand, if the voltage drop across the nanocrystal-substrate junction is larger than that across tip-nanocrystal junction, then the first tunneling event corresponds to discharging of the nanocrystal by the transfer of one electron from the nanocrystal to the substrate. In this tunneling configuration, the second tunneling event proceeds through the transfer of an electron from the tip to the discharged nanocrystal. This new electron is injected into a higher energy level and interacts with the already existing hole in the nanocrystal. This electron-hole interaction affects the dynamics of the injected hot electrons in the nanocrystal. Optical measurements on semiconductor nanocrystals show confinement induced enhancement of electron-hole interaction that leads to electron relaxations through energy exchange with the optically created holes.

The voltage drop on the tip-nanocrystal junction is controlled by adjusting the tip-nanocrystal separation. Our STS measurements on a single nanocrystal at different tip-nanocrystal separations show a decrease in Coulomb blockade as the tip-nanocrystal separation increases. The details of this study and its analysis are presented in chapter three of this thesis. This result has two implications. First, the region of zero current around zero bias voltage (Coulomb blockade $\sim 1.8\,\mathrm{eV}$) is due mainly to the HOMO-LUMO gap. Second, in our experimental configuration $C_1 \ll C_2$, therefore most of the voltage drop in our experiments is on the tip-nanocrystal junction. In order to make an estimate of the change in voltage across tip-nanocrystal junction and whether that change will affect the experiment configuration, the tip retraction is recorded during BEES measurements. The recorded change in the tip-substrate separation as the voltage increases in constant current mode is found to be around $0.8\,\text{Å}$ for voltages up to $1.5\,\mathrm{V}$. Since most of our measurements

are done at voltages just above the Schottky diode threshold, this change in tip-substrate separation will not have a significant effect on the data interpretation.

In fact, our STS studies show large Coulomb blockade that is comparable to semiconductor nanocrystals. This is expected since optical studies on these nanocrystals show HOMO-LUMO gap of the order of 1.31 eV [29]. In addition, dI/dV measurements resolve two peaks on both sides of zero bias that are separated by about 190 eV. This separation is less than the charging energy, and therefore these peaks are attributed to tunneling through the energy levels of the nanocrystal. This is because in our tunneling experiments the nanocrystal-substrate junction is the fast junction. In a double barrier tunneling junction, the resistance of the junction determines its tunneling rate. Thus, if the nanocrystal-substrate is the fast junction, then electron tunneling-out rate is faster than tunneling-in rate. In this tunneling configuration, the dI/dV peaks correspond to tunneling through the discrete states of the nanocrystals. The junction resistance and hence the tunneling rate is determined by the resistive coupling between the nanocrystal and the substrate. Our nanocrystals are chemically deposited on a rough gold film where nanocrystals are usually confined in the valley formed by the gold grains. That results in strong nanocrystal-substrate coupling and therefore low junction resistance. The above mentioned experimental evidence is similar to tunneling spectroscopy of semiconductor nanocrystal where, due to the large band gap, the conduction band and valence band states are resolved on the separate side of the voltage. The above-discussion implies that the BEES data presented in this chapter corresponds to electron injection into the nanocrystal in the absence of holes. Thus the electron relaxation mechanisms addressed do not include electron-hole interactions.

4.5.1 BEES Threshold Shift

Our experimental BEES spectra on single nanocrystals show a shift in the threshold when compared with BEES on a substrate. A typical STM image of one studied nanocrystal sample is shown in Figure 28(a). Imaging shows a high density of nanocrystals. Nanocrystals seem to be more immobile on the surface when they form a monolayer or rafts. Single isolated nanocrystals are difficult to image, because they tend to move under the influence

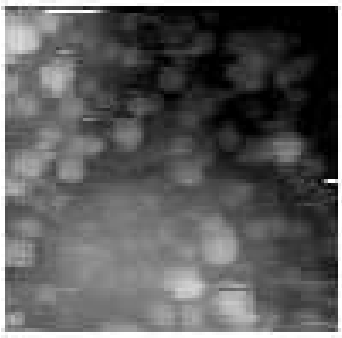

(a)

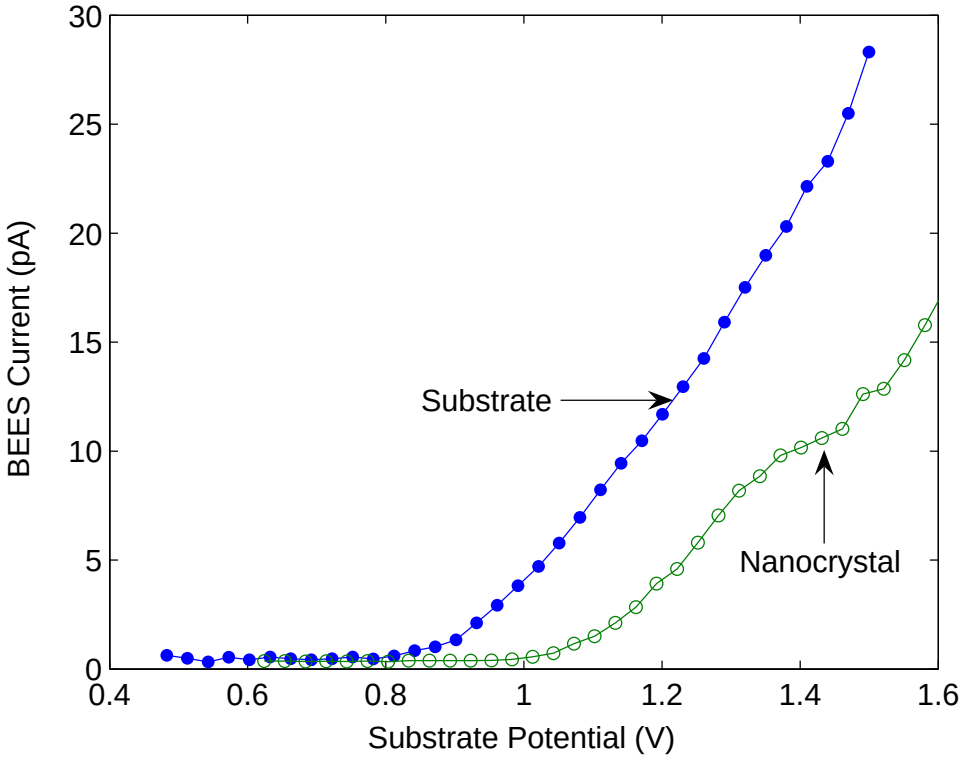

(b)

Figure 28: BEES spectroscopy on a single 28 kDa Au nanocrystal. (a) STM image of nanocrystals at 77 K. Tunneling current setting at 100 pA and tip voltage bias at −2 V. (b) Comparison of BEES spectra on a nanocrystal and on substrate. BEES spectra taken on a nanocrystal shows a shift in the threshold as a result of electron relaxation in the nanocrystal.

of the tip. This is an indication of the weak attachment of nanocrystals to the surface, which is because the thin gold film surface is very rough and the xylenedithiol molecules do not form an ordered monolayer as compared with the atomically flat gold film on mica substrates. Figure 28(b) shows two BEES spectra that are taken on a nanocrystal and on the substrate. The substrate BEES current shows a turn on voltage that equals to the Schottky barrier height ($\sim 0.85\,\mathrm{V}$). On the other hand, BEES on nanocrystals shows a threshold voltage that is larger than the substrate Schottky barrier height. Moreover, as the voltage increases, nanocrystal BEES exhibits noticeable features. BEES current increases at a slow rate for defined energy ranges, which result in a roll over in the BEES spectra. This roll over is followed by enhancement in BEES current. In order to understand the physics behind the threshold delay and the structures in the BEES spectra, we acquire tunneling IV on the same nanocrystal. Figure 29(a) shows a tunneling IV and BEES spectra taken on the same nanocrystal. Tunneling IV on nanocrystal was taken at constant tip-substrate sparation, and it shows current steps that correspond to tunneling through the nanocrystal energy levels. We expect to see enhancement in BEES current whenever a new current carrying channel is available. However, since the injection current is maintained constant during BEES spectrum acquisition, the increase in voltage increases the number of accessible energy states on the nanocrystal not the total tunneling current. In other words, the accessible states on the nanocrystal carry the same amount of current at all times. The comparison of tunneling and BEES spectra is useful to identify the location of tunneling current steps relative to the Schottky barrier. The first current step in the tunneling IV shown in Figure 29(a) is located at $0.35\,\mathrm{V}$. This is well below the Au/Si(111) Schottky barrier. Therefore, electrons that occupy this state do not have enough energy to overcome the barrier at the metal semiconductor interface. In addition, if electrons that are injected into higher energy states (at high voltages) relax to this energy state, then we expect a reduction in I_c near the BEES threshold. This would result in an apparent shift in the BEES threshold.

Figure 29(b) shows a simple schematic model for describing the threshold shift in BEES spectrum on nanocrystal. When electrons are injected to high energy states, they can

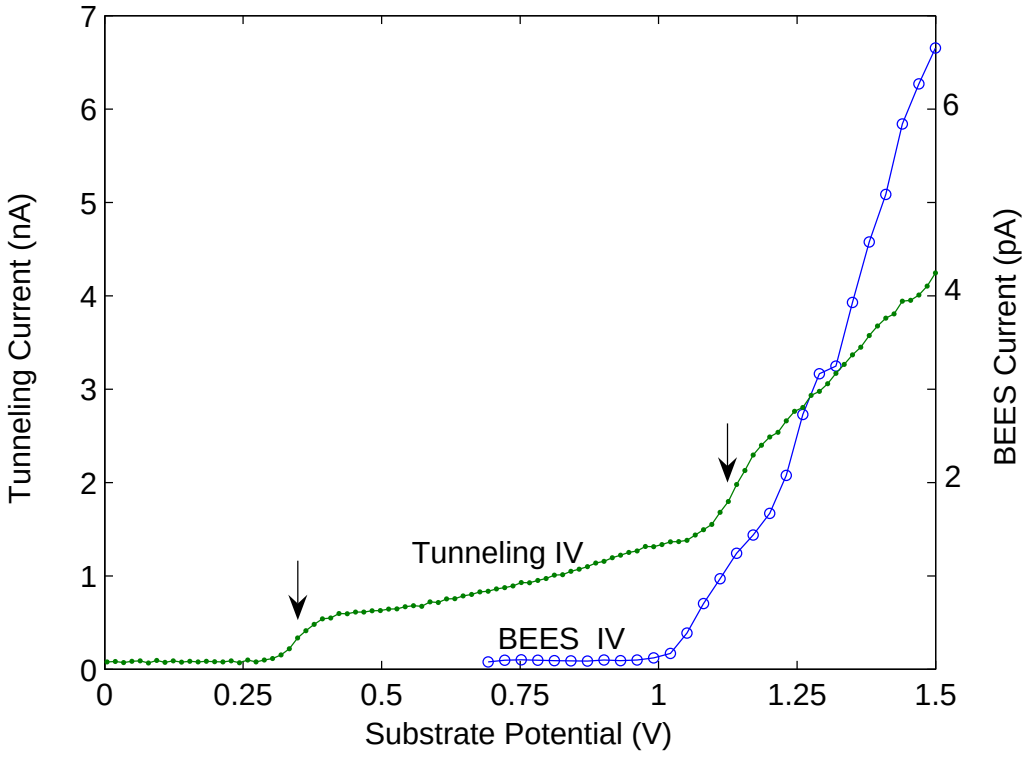

(a)

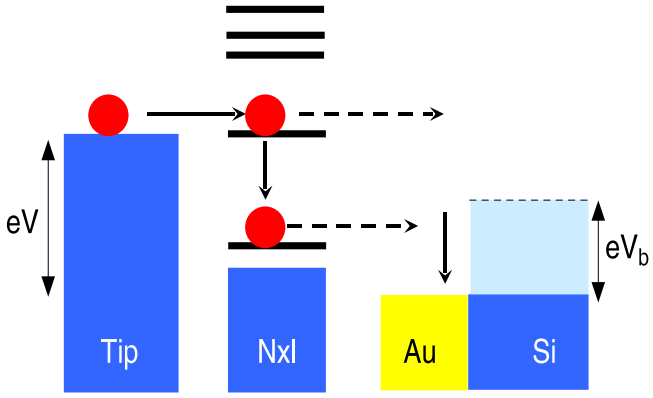

(b)

Figure 29: Comparison of BEES and tunneling spectra taken on the same single nanocrystal. (a) BEES spectra taken on a nanocrystal shows a shift in the threshold. Tunneling IV taken on the same nanocrystal shows that the first tunneling step is located at an energy below the Schottky barrier. An enhancement in BEES current is taking place near the threshold of the second step in the tunneling IV. (b) Schematic of the energy level diagrams showing that electrons relaxations into an energy level below the Schottky barrier results in a threshold shift.

either tunnel-out into the gold substrate without losing energy, or they can relax down to a lower energy state by losing some energy through inelastic scattering in the nanocrystal. If electrons relax to an energy level that is above the Schottky barrier, they still have enough energy to overcome the barrier and are collected at the semiconductor. However, if electrons relax down to an energy level that is below the Schottky barrier, then they have zero probability of being transmitted into the collector. For the BEES spectrum shown in Figure 29(a), the first charging step is below the Schottky barrier, and therefore electron relaxations in the nanocrystal result in an apparent shift of the BEES spectrum threshold.

The comparison of BEES and tunneling spectra shows some interesting similarities. For example as shown in Figure 29(a), BEES spectrum taken on a nanocrystal has a threshold shape similar to the charging step shape in the tunneling IV. Another interesting similarity is the enhancement of BEES current at the energies of the charging steps in the tunneling IV. Moreover, for the energy range between charging steps in the tunneling IV, BEES current seems to increase at slow rate. This is because as the voltage is swept in the energy range between charging steps, the number of electrons on the nanocrystal is maintained constant, yet more charging configurations become available for these electrons in the nanocrystal. Thus electron relaxations increases, and BEES current is attenuated as a result. The enhancement in BEES current at the tunneling step energies results from the increase of the number of electrons on the nanocrystal, which decreases electron relaxation and results in an increase of the tunneling-out current.

4.5.2 BEES Roll Over

The location of charging peaks in the tunneling spectroscopy are directly related to the size of the nanocrystal, because quantum size effects result in discrete energy states as well as an increase in the Coulomb blockade. Our tunneling spectroscopy measurements on the 8 kDa gold nanocrystals show the first charging peak located around 0.9 V, slightly above the Schottky barrier. BEES measurements on such nanocrystals should show interesting features. Since the location of the first accessible energy level is above the Schottky barrier,

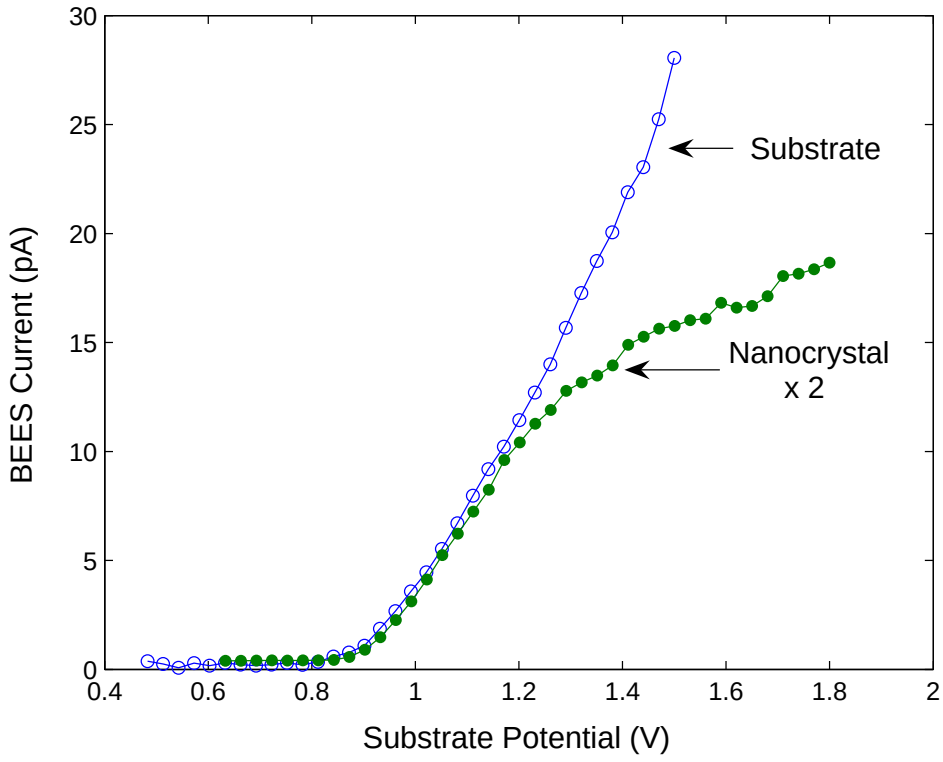

(a)

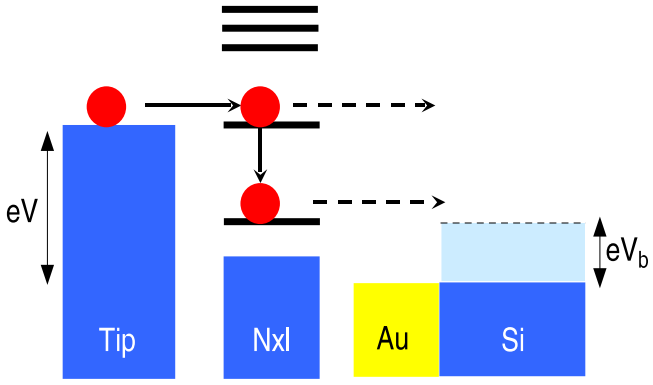

(b)

Figure 30: Comparison of BEES spectra taken on the substrate and on 8 kDa gold nanocrystal. (a) BEES spectra on substrate and on nanocrystal. Both spectra show almost the same turn-on voltage. However, the nanocrystal BEES spectrum rolls over at high energy as compared to substrate BEES. (b) Schematic of the energy level diagrams showing electron relaxation into an energy level near the Schottky barrier. This results in reduced transmission, hence the roll-over at high voltage.

electrons relaxing to this level will still have enough energy to be collected in the semiconductor. Figure 30 shows BEES spectra taken on a single 8 kDa nanocrystal and on the substrate. Both spectra seem to have the same threshold. In addition, both spectra seem to have nearly the same threshold shape. This shape of the current curve near threshold is determined by the transmission coefficient at the metal semiconductor interface. However, when compared with BEES on substrate at voltages slightly above threshold, BEES on the nanocrystal tends to roll over at high voltages. A possible explanation of the observed roll-over is as follows: Since the injection current is kept constant during BEES spectrum acquisition, the number of charging configurations increases as the voltage increases. The increase in the number of charging configurations results in enhanced electron relaxation in the nanocrystal. After relaxing, electrons impinge on the metal/semiconductor interface with small energy. The transmission coefficient at the metal semiconductor interface is approximately proportional to the electron energy as

$$T(E) \propto \sqrt{E}. \tag{51}$$

Equation 51 implies that if electrons relax down into a lower energy state then they will have lower probability of transmission at the interface. Therefore, the roll-over of BEES on nanocrystal shown in Figure 30 results from electrons losing some of their energy in the nanocrystal.

4.6 Hot Electron Lifetimes in Single Nanocrystals

Measurements of the lifetimes of hot electrons in single nanocrystals are important for the application of nanocrystals in single electron devices. These measurements also have fundamental scientific importance as they reveal information about the operative physical mechanisms in confined structures and their size dependence. In this section, experimental measurements of hot electron lifetimes are presented using our new single-nanocrystal BEES method.

Time-resolved optical methods are ideal experimental techniques for measuring the lifetimes of excited electrons. However, there are some problems associated with optical measurements particularly for nanocrystals. First, in optical measurements, the relaxation

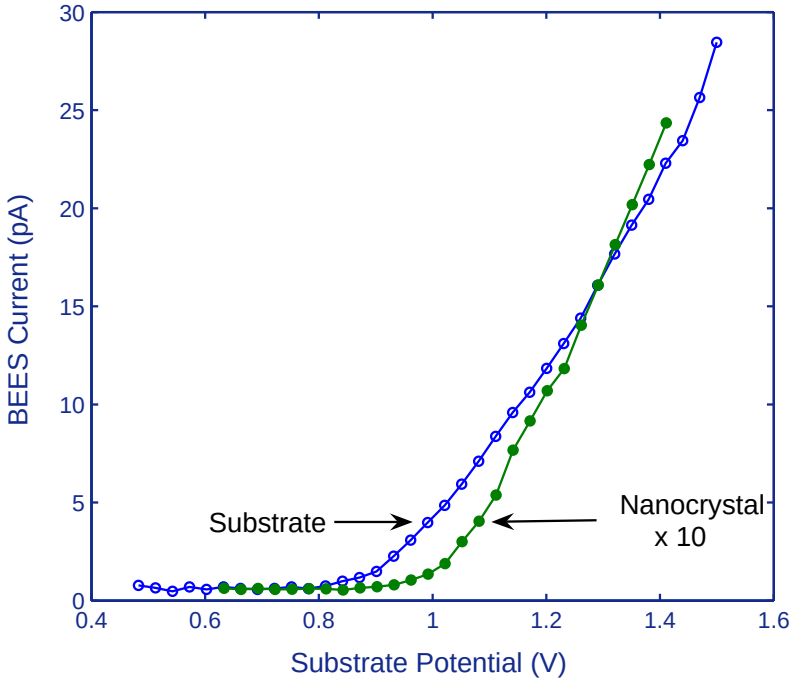

Figure 31: BEES spectra on the substrate and on a single nanocrystal. BEES spectrum taken on a nanocrystal shows an attenuation of a factor of ten and a shift in the threshold when compared with BEES on the substrate. The attenuation results from energy loss in the nanocrystal. The shift in threshold is attributed to electron relaxation into energy level below the Schottky barrier.

times are intensity dependent. Therefore, for accurate measurements of lifetimes, the optical intensity should be as low as possible. However, for low optical intensity, the signal to noise ratio is low. So, optical measurements do not provide accurate information about single electron excitation in nanocrystals. Second, optical measurements are always performed on an ensemble of nanocrystals where size distribution significantly affects the data interpretation.

Electron injection in our experiments was maintained at 1 nA tunneling current, which corresponds to about 160 picoseconds between tunneling-in events. This is the tunneling rate across the tip-nanocrystal junction, which is the slower junction in our system. The residence time of an electron on the nanocrystals is determined by the tunneling-out rate of electrons from the nanocrystal to the substrate, which is the fast junction. Therefore, if hot electrons live for time shorter than their residence time, then relaxation takes place in the nanocrystal.

Lifetimes of hot electrons in our studies are experimentally measured by comparing BEES on a nanocrystal with BEES on a substrate. The amount of attenuation in BEES on a nanocrystal as compared to BEES on a substrate is used to estimate the lifetimes. The rate of injection is constant and the same (1 nA) for both spectra. Therefore, BEES spectrum on a substrate is used as a base-line for the collected current in the semiconductor. This means that the effects of electron scattering in the base layer and scattering and matching of the electrons wavefunctions at the metal semiconductor interface are included in this base-line. Therefore, the difference in the collected BEES current intensity for the two spectra is due to electron relaxation in the nanocrystal. The amount of current attenuation is proportional to the strength of relaxation and hence the the lifetimes of hot electrons in the nanocrystal. Figure 31 shows two BEES spectra that are taken on a nanocrystal and on a substrate. When compared with substrate BEES, the BEES on nanocrystal shows a threshold shift and one order of magnitude attenuation in the BEES current intensity. The shift in threshold is attributed to electron relaxation to energy levels below the Schottky barrier as described in a previous section. One order of magnitude attenuation in BEES current intensity means that electrons relaxations in the nanocrystal are ten times faster than their

residence time. Actual lifetime determination requires measuring the mean tunneling-out rate. In this section we will make a quantitative estimate of the an upper limit for hot electron lifetimes in single nanocrystals using the experimentally determined tunneling-in rate of 160 picoseconds. An upper limit of hot electron lifetimes in a single gold nanocrystal equals to the mean tunneling-in rate divided by the attenuation factor that is on the order of 16 picoseconds. The actual lifetimes should be the mean tunneling-out rate divided by the attenuation factor, which is much less than 16 picoseconds.

As mentioned through experimental evidence, hot electrons relaxations measured by our developed BEES method are not mediated by electron-hole interaction in the nanocrystals as compared with optical studies. In the absence of holes, hot electrons in single isolated nanocrystal can only relax through surface-scattering or phonon coupling. The subpicosecond relaxation times reported by femtosecond dynamics measurements on the 28 kDa nanocrystals [29] is in good agreement with intraband relaxations in semiconductor nanocrystals in the presence of an optically created hole. Electron relaxations mediated by electron-hole interaction involve transfer of the electron excess energy to a hole, with a subsequent fast hole relaxation through its dense spectrum of states [47]. These relaxation rates are reduced by a factor of ten when electrons are chemically injected into the nanocrystal excited states where no holes are available in the nanocrystal [48].

4.7 Energy Distribution of Tunneling-out Electrons

One important objective of BEES measurements on single nanocrystals is to be able to map the energy distribution of the tunneling-out electrons. The measured BEES spectra are the integration of the electron current over energy slices. In previous sections, we tried to extract information about electron dynamics in single nanocrystals by comparing the BEES on nanocrystal spectrum with both tunneling IV and BEES taken on the substrate. These comparisons resulted in information about the attenuation as well as lifetimes of the hot electrons. In this section, a further analysis of BEES data will be presented in order to extract the energy distribution of electrons tunneling-out of the nanocrystals. The theory of BEES was introduced in section 4.3. A simple semiclassical approach has been used

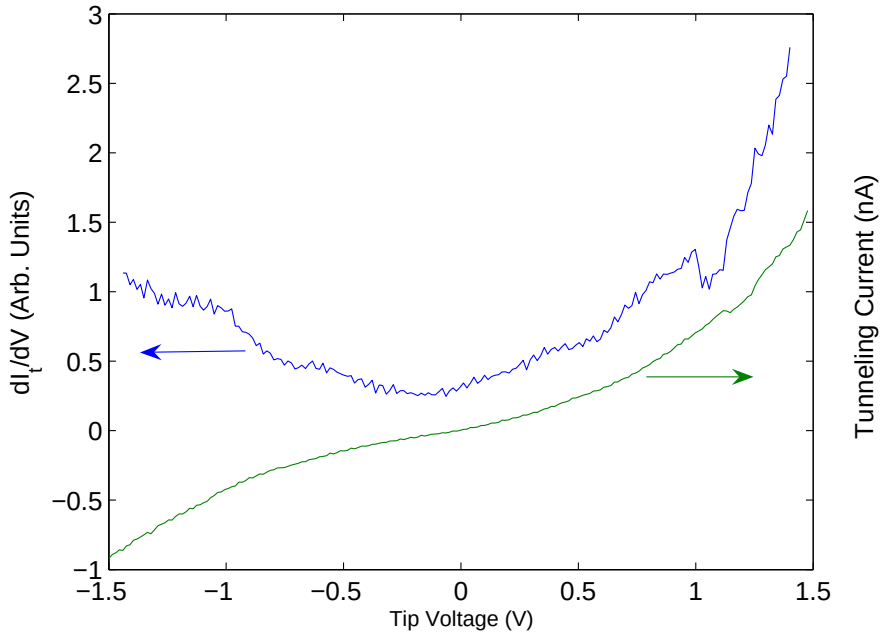

(a)

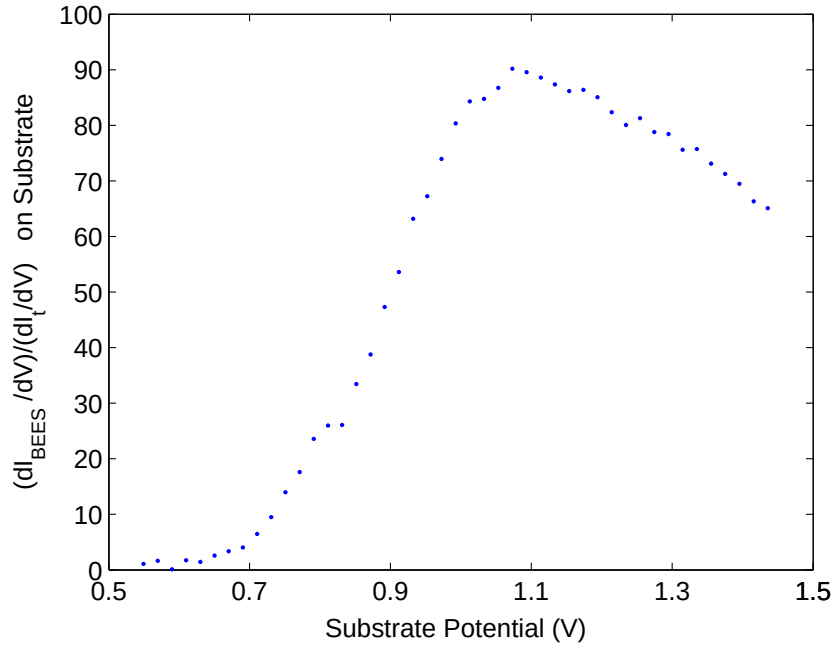

(b)

Figure 32: Transmission coefficient across the metal/semiconductor interface. (a) Measured tunneling current and its numerical derivative. Numerical derivative of tunneling current with 9 point averaging (green curve). (b) Ratio of the numerical derivatives of BEES IV and tunneling IV taken on the substrate.

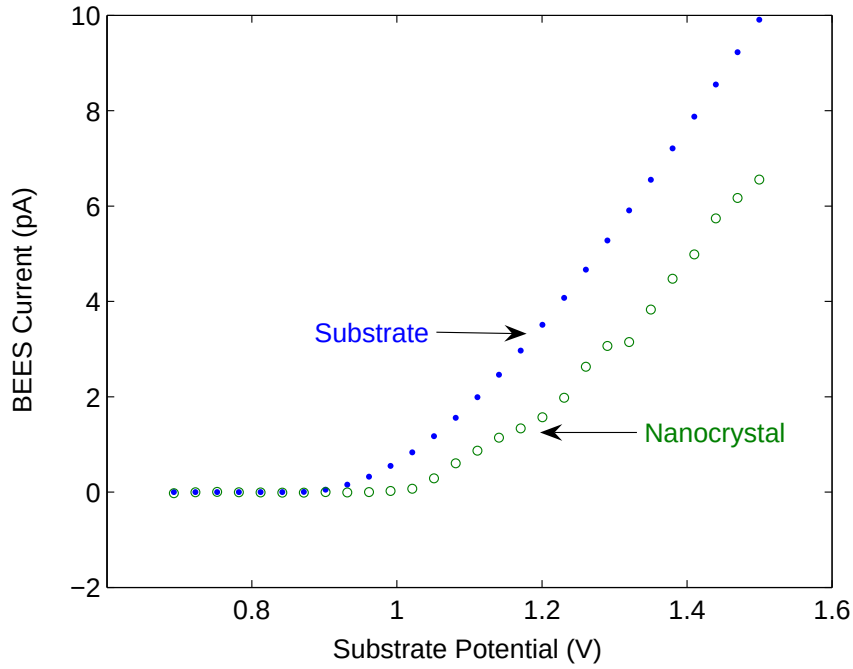

(a)

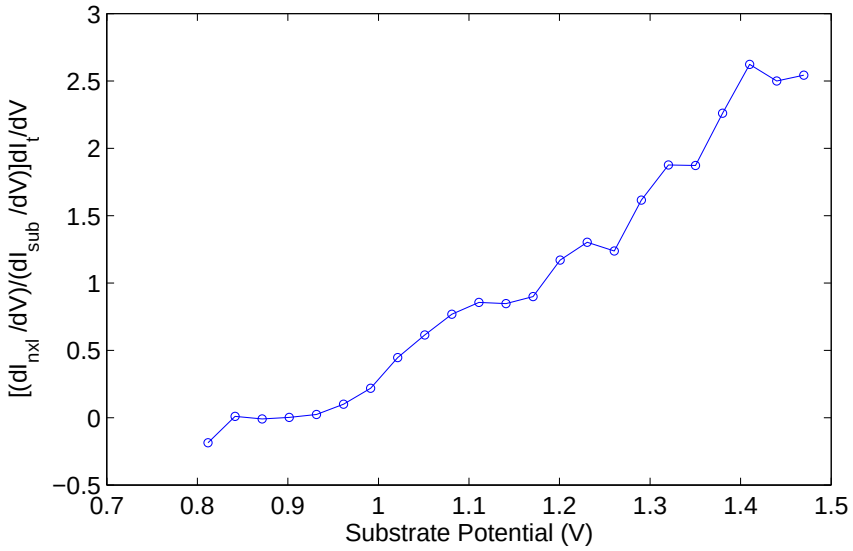

(b)

Figure 33: Energy distribution of tunneling-out electrons. (a) BEES spectra taken on the substrate and on a single nanocrystal. (b) The curve is the numerical derivative of BEES spectrum taken on nanocrystal divided by the transmission coefficient at the metal/semiconductor interface. The transmission coefficient is proportional to the ratio of the derivative of BEES and tunneling current IV taken on the substrate. Five point averaging was used to smooth the data after the numerical derivation.

for BEES current calculation. For the Au/Si substrate both the tunneling current I_t and collector current I_c can be rewritten as

$$I_t = \int_{E_f}^{E_f+eV} e\,\rho(E)\,\Gamma(E,V)\,dE, \tag{52}$$

$$I_c = \int_{E_f+eV_b}^{E_f+eV} e\,\rho(E)\,\Gamma(E,V)\,T(E)\,dE, \tag{53}$$

where $\rho(E)$ is the density of states in the STM-tip, $\Gamma(E,V)$ is the tunneling rate between the STM tip and the gold substrate (base), and $T(E)$ is the transmission coefficient across the metal/semiconductor interface. The transmission coefficient can be approximated as

$$T(E) \propto \frac{\partial I_c/\partial V}{\partial I_t/\partial V}. \tag{54}$$

The BEES on a nanocrystal can be written as

$$I_{nxl} = \int_{E_f+eV_b}^{E_f+eV} e\,\rho(E)\,\Gamma_{nxl}(E,V)\,T(E)\,dE, \tag{55}$$

where $\Gamma_{nxl}(E,V)$ is the tunneling rate from the nanocrystals to the gold film. The derivative of BEES spectrum taken on a nanocrystal is given by

$$\frac{\partial I_{nxl}}{\partial V} \propto \frac{\partial \Gamma_{nxl}(E,V)}{\partial V}\,T(E). \tag{56}$$

The energy distribution of the tunneling-out electrons therefore can be calculated by dividing Equation 56 by T(E). The energy distribution of the tunneling-out electrons per energy width δE is therefore given by

$$\frac{\partial \Gamma_{nxl}(E,V)}{\partial V} \propto \frac{\partial I_{nxl}/\partial V}{\partial I_{sub}/\partial V}(\partial I_t/\partial V). \tag{57}$$

Equation 57 is an approximation for the rate of tunneling-out electrons per energy width. Ideally, the first derivative of both BEES current and tunneling current should be acquired at a constant tip-substrate separation using a lock-in detection method. This experiment requires holding the STM tip for the duration of spectrum acquisition, which was not possible to achieve in the current experimental design for the following reasons. First, due to the high noise level, BEES current is acquired at very low-pass-filter sittings

(3 Hz), and each data point was sampled a few thousand times. That results in a relatively long time ($2-3$ minute) for BEES spectrum acquisition. It is not practical to hold the STM tip for such a long time due to vertical drifts and electric field generated motions during the sweeping of the tip voltage. Second, BEES current represents small ratio of the tunneling current, and holding the tip results in a small BEES current at low voltages.

In this section, we will attempt to numerically extract the energy distribution of the tunneling-out electrons. This is possible by making a simple approximation in order to use the data acquired at constant tunneling current. The approximation is that the change in tip-nanocrystal separation is the same for both of the BEES spectra taken on the substrate on the nanocrystal. They are not equal because the density of states on the nanocrystals modifies the tunneling current, and hence tip retraction will be different. With this assumption the effect of tip-retraction at constant current will cancel out through the division of their numerical derivatives.

Figure 32(a) shows a tunneling current IV that was taken on the substrate along with its numerical derivative. The transmission coefficient across the metal/semiconductor interface is calculated by taking the ratio of the numerical derivative of BEES on the substrate in Figure 33(a) and the tunneling dI/dV in Figure 32(a). The ratio of these two derivatives is shown in Figure 32(b). The curve represents an approximation for the overall shape of $T(E)$ since the number of data points used is not enough to generate a smooth curve. Figure 33(b) shows a numerically extracted spectrum of the rate of the energy distribution of tunneling-out electrons. The spectrum shape has an overall shape that progresses at a slow rate. The enhancement in BEES current in Figure 33(a) at about 1.1 V appears as steps in the tunneling-out rate. The density of points in the acquired BEES spectra is low, and a better interpretation of some of the features in the tunneling-out spectrum requires a higher density of data points.

CHAPTER V

COMPARISON OF BEES AND OPTICAL SPECTROSCOPY

5.1 Introduction

The size-induced changes of the electronic structure of nanocrystals result in a change in their optical properties. A variety of optical spectroscopic methods have been used to probe this change in properties. Optical spectroscopy probes the energy separation between electric dipole allowed transitons using frequency-resolved techniques. Time-resolved techniques also measure the lifetimes of excited states and their respective energy relaxation channels. Optical measurements are usually performed on an ensemble of nanocrystals in solution or on a surface. Therefore, the measurement is an average property of different sizes. Optical measurements have been used by many research groups to gain information about the density of states [49]. Since these measurements are governed by the selection rules in the system, they fail to probe states that are inaccessible due to forbidden transitions. An example of the limitations of optical spectroscopy is bulk silicon, where the lowest energy transition is indirect and therefore not allowed. On the other hand, tunneling-based spectroscopic techniques have weak or no restriction on the momentum conservation. In tunneling spectroscopy, it is possible to probe separately the conduction band states and the valence band states since there are no selection rules [10]. Photoluminescence excitation spectroscopy has been widely used to probe the electronic structures of materials, where the intraband energy levels separations can be extracted from the spacing between peaks in the spectrum [50, 51]. In principle, it should be possible to compare directly the photoluminescence excitation and the tunneling spectra. However, in tunneling spectroscopy, the nanocrystal charge state changes, and therefore the energy level structure may be perturbed as compared with the neutral nanocrystal energy levels monitored by the photoluminescence

excitation technique. Furthermore, even if nanocrystal charging does not intrinsically perturb the level structure significantly, the peak spacing and peak structure in the tunneling experiment depend extrinsically on the parameters of the double-barrier tunneling junction.

Optical absorption spectroscopy provides a means for identifying the electronic properties of nanocrystals, allowing information to be obtained about the nature of the electronic structure of the system. While optical absorption measurements are relatively easy and inexpensive to perform, and result in a very useful information, the technique has some limitations. When compared to tunneling spectroscopy, there are three limitations. The first limitation is that optical absorption experiments have to be done on an ensemble of nanocrystals due to the very low signal to noise ratio from an individual nanocrystal. Ensemble measurements usually have an impurity issue, which can affect the interpretation of the data. In addition to sample impurity, orientational, configurational, and local environmental effects are found to result in an inhomogeneous broadening of the spectra and therefore limit the resolution of the experiment. Another limitation on the spectral resolution comes from the temperature at which the measurement is performed. Due to technical difficulties, most of the absorption experiments are done at room temperature, although it is possible to perform absorption experiments at low temperatures. The final limitation is that optical measurements provide information only about the density of states for which the electric dipole transitions are allowed. However, this information is valuable when compared with another technique that has different selection rules.

The large energy level separation in nanocrystals has been predicted to inhibit the intraband energy relaxation due to a phonon bottleneck [52]. Recent experimental data argues against this effect [53, 54]. In a bulk semiconductor, optical excitation involves the formation of an electron and hole, which are separated by distances that include a number of atoms or ions in the material. After initial fast energy redistribution of the excited carriers, carriers relaxation in a bulk II-VI semiconductor proceeds primarily by radiative decay. On the other hand, carrier dynamics in nanocrystals take place at a time scale shorter than the radiative time scale due to the enhancement of nonradiative mechanisms associated with surface scattering and surface state trapping [54]. Furthermore, in nanocrystal systems,

the optical nonlinearity at the band edge results mainly from energy-level filling leading to bleaching of optical transitons. The large energy level separation inhibits thermal depopulation of the lowest quantized states, the role of energy level filling in nanocrystals is enhanced in comparison with that of bulk materials. In small nanocrystals, Coulomb interaction is enhanced because carrier motion is confined in a small space. Coulomb potential scales with $1/R$, where R is the radius of the nanocrystal. Further enhancement of the Coulomb electron-hole interaction can occur as a result of surface trapping of one type of carriers (electrons or holes) leading to the generation of strong local fields in the nanocrystal.

Most of the optical measurements are done by using a light source to populate the conduction band states with electrons from the valance band and monitor their relaxation back into the conduction band ground state or into the valance band states. The population involves the creation of electron hole pair, and their Coulomb interaction could mediate their relaxations. However, in nanocrystals, electron-hole interaction is not important in electron relaxations unless the surface is completely free of surface traps, or the hole density of states is very large [48]. Coulomb mediated relaxation mechanisms will not compete with mechanisms involving the nanocrystals surface. Surface trapping is a well known mechanism of fluorescence quenching in both semiconductor and very small metal nanocrystals. Surface passivation is known to result in an increase in the fluorescence intensity of CdSe nanocrystals by orders of magnitude [55, 56].

Different experimental studies have been performed in order to explain the relaxation mechanisms of hot electrons in both semiconductor and metallic nanocrystals. These studies include the use of passivated surface to eliminate traps on the surface. Introducing molecules to the nanocrystals solution in order to trap holes and study the holes involvement in the relaxation process. Chemically injected electrons have been also introduced into the nanocrystals excited states and their intraband relaxation is studied using infrared spectroscopy. These studies are done on ensembles of nanocrystals in solutions, and therefore sample impurity is still an issue in these measurements.

The work performed and presented in this thesis investigates nanocrystals at the single level. These investigations directly correlate the change in properties to the size change.

Our newly developed BEES technique enables us to investigate electron dynamics in single nanocrystal as reported in Chapter 4. There are many advantages for using BEES to study nanocrystals. First, BEES measurements will not be affected by any kind of impurity in the nanocrystals solution. Second, there is no size distribution effect on the measured signal, since the measurements are performend on a single nanocrystal; and therefore BEES measurement relates directly the size effect on the electronic structure of nanocrystals. Third, in BEES measurements, electrons are injected into the nanocrystals from an external source (STM tip), thus, there are no holes associated with the electronic excitations. This is an ideal system to test the effect of electron-hole Coulomb interactions on the hot electron relaxations in a single nanocrystal.

This chapter includes a summary of the optical properties of nanocrystals. It also introduces some of the optical measurements techniques currently used in studying nanocrystals. When possible the results of some of those studies are reported and compared with our tunneling and ballistic spectroscopic measurements. In order to understand the change in materials properties as a function of size, a different combination of experimental techniques needs to be performed on the material. Although these techniques are different, when compared they complement each other, and a new unique information about the system properties is gained. Our tunneling spectroscopy measurements and some optical techniques, like optical absorption and photoluminescence excitation, are expected to complement each other. This complement is particularly important in the determination of the density of states and the identification of energy levels locations. In addition, our newly developed BEES technique is found to complement time-based optical spectroscopy. In our BEES experiments, hot electrons are injected with known energy at a constant rate into the nanocrystals excited states, and we monitor the energy distribution of these electrons as they tunnel out from the nanocrystals. The intensity of this distribution will depend on the amount of energy loss inside the nanocrystals. Therefore, BEES measurements will reveal direct information about the energy lose mechanisms within a single nanocrystal. Furthermore, from our experimental conditions, we can measure lifetimes of hot electrons in a single nanocrystal.

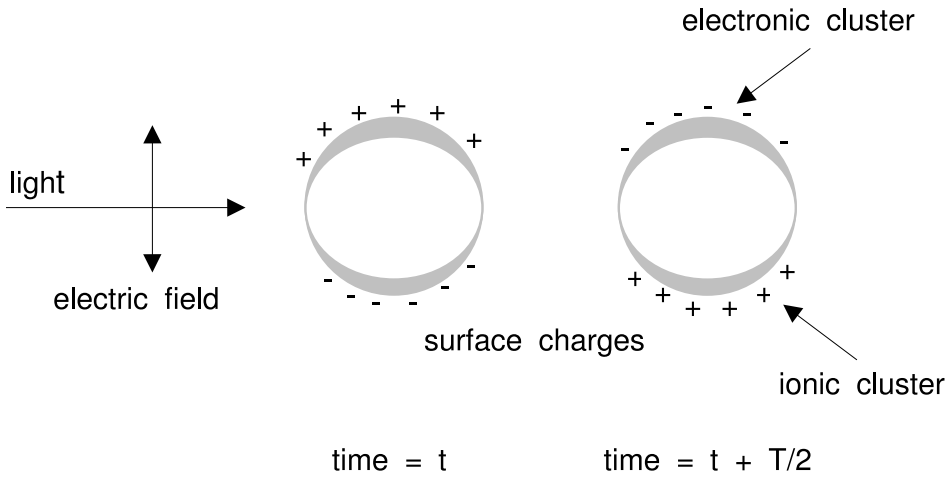

Figure 34: A schematic illustrating the excitation of the dipole surface plasmon oscillation. The electric field induces a polarization of the conduction band electrons with respect to the heavier core of the spherical nanocrystal. A net charge difference is built at the surface and acts as a restoring force.

5.1.1 Surface Plasmon Oscillations in Metal Nanocrystals

The surface plasmon resonance is described as the coherent motion of conduction band electrons caused by the interaction with an external electromagnetic field. In a classical picture, the electric field of an incoming light wave induces a polarization of the electrons with respect to the ionic core of the nanocrystal. Ultimately, this polarization drives all the electrons to follow a dipole oscillation with the same phase. When the frequency of the incident electromagnetic field comes in resonance with the electronic motion, a strong absorption in the spectrum is observed, and it is the physical origin of the color in these nanocrystals. The frequency and width of the plasmon peaks depend on the size, shape, and the dielectric constant of both the metal and its surrounding [57]. The plasmon oscillations are very enhanced and shifted into the visible region for the noble metals [58].

Light interaction with small spherical metal particles, which account for the surface plasmon resonance, were explained in a theory developed by Mie in 1908 [59]. Mie used the dielectric constant of the macroscopic bulk for the small sphere and solved Maxwell's equations for electromagnetic wave interacting with this sphere. This approach has resulted in a series of multipole oscillations for the extinction and scattering cross section as a

function of the particle radius. As the particles size increases higher order-modes dominate the oscillation causing the absorption band to redshift and broaden.

For spherical particles with a radius much smaller than the interacting light wavelength ($R < 20\,nm$), only dipole oscillations contribute, and Mie's theory reduces to the following expression

$$\sigma_{ext} = \frac{9\,V\,\varepsilon_m^{3/2}}{c}\frac{\omega\,\epsilon_2(\omega)}{[\epsilon_1(\omega)+2\,\varepsilon_m]^2+\varepsilon_2(\omega)^2}, \tag{58}$$

where V is the particle volume, ω is the angular frequency of the incident light, and c is the speed of light. ε_m and $\varepsilon(\omega) = \varepsilon_1(\omega) + i\varepsilon_2(\omega)$ are the dielectric functions of the surrounding medium and the metal, respectively.

Equation 58 is independent of the particle size, and its prediction is in disagreement with experimental results on metallic nanocrystals with sizes less than 10 nm [57]. Experimental studies show that pasmon oscillations are size dependent, and they disappear completely for nanocrystals with diameters less than about 2 nm [30, 35]. The size dependence of the plasmon oscillations is introduced into Mie's theory through modification of the materials dielectric function. This modification is introduced through a classical approach since electron-surface scattering must be enhanced in small particles.

Many theoretical models have been proposed to describe the size dependence of plasmon oscillation. In most of these models, the dielectric constant of the material is assumed to be size dependent ($\varepsilon(\omega, r)$) below an average diameter of about 20 nm [59, 60]. The smaller the nanocrystals sizes are, the larger the electron-surface scattering rates. Therefore, the electrons coherence is lost at a faster rate in small particles than in large particles. One successful model that describes the plasmon frequency size dependence treats the dielectric function as a combination of an interband term $\varepsilon_{IB}(\omega)$ and a Drude term $\varepsilon_D(\omega)$ by considering only the free conduction electrons.

$$\varepsilon_D(\omega) = 1 - \frac{\omega_p^2}{\omega^2 + i\gamma\omega}, \tag{59}$$

where $\omega_p^2 = ne^2/\varepsilon_0 m_{eff}$ is the bulk plasmon frequency. γ is introduced as a phenomenological damping constant and is related to the lifetimes of electron-electron, electron-phonon,

and electron-defect scattering in the bulk material [57].

$$\gamma_0 = \sum_i \tau_i^{-1} = \tau_{e-e}^{-1} + \tau_{e-ph}^{-1} + \tau_{e-d}^{-1}, \tag{60}$$

where γ_0 is the bulk damping constant. For nanocrystals smaller than the mean free path of the conduction electrons, electron-surface scattering becomes effective. An additional term for electron-surface scattering is added to the equation above, and γ becomes a function of nanocrystal radius r [61, 62]

$$\gamma(r) = \gamma_0 + \frac{A\nu_F}{r}, \tag{61}$$

where A depends on the scattering process details. This is considered an intrinsic size effect since the material dielectric function is size dependent itself. For very small nanocrystals ($r < 2\,nm$), the plasmon oscillations are strongly damped, and their absorption peaks become weak and broaden until they disappear completely for $r < 2\,nm$. For these very small nanocrystals, the electron density in the conduction band is small and they exhibit a molecular-like energy level structure.

5.2 Hot Electrons Dynamics in Gold Nanocrystals

With the advancement of ultrashort laser pulses technology, electrons in metals can be selectively excited, and the electron-phonon coupling can be monitored in real time. This is possible using laser pulses that are shorter than the electron-phonon energy relaxation time. Due to the high electron density in metals, electron-electron interactions are expected to be strong enough to thermalize the electron gas within the duration of the exciting laser pulse. In the two-temperature model (TTM) [63], the electrons and the lattice can be treated as two coupled subsystems because of the difference in their heat capacities. After laser pulse excitations, electrons absorb the photon energy, and a nonequilibrium temperature difference is established immediately between the electron gas and the lattice. The excitation energy is then exchanged between the electron subsystem and the lattice, energy relaxation T_1. The time evolution of the electron and lattice temperatures are represented by the following mathematical equations [63].

$$C_e\left(T_e\right)\frac{\partial T_e}{\partial t} = -g\left(T_e - T_1\right) + \bigtriangledown.(\kappa^{'} \bigtriangledown T_e) + LP(Z,t) \tag{62}$$

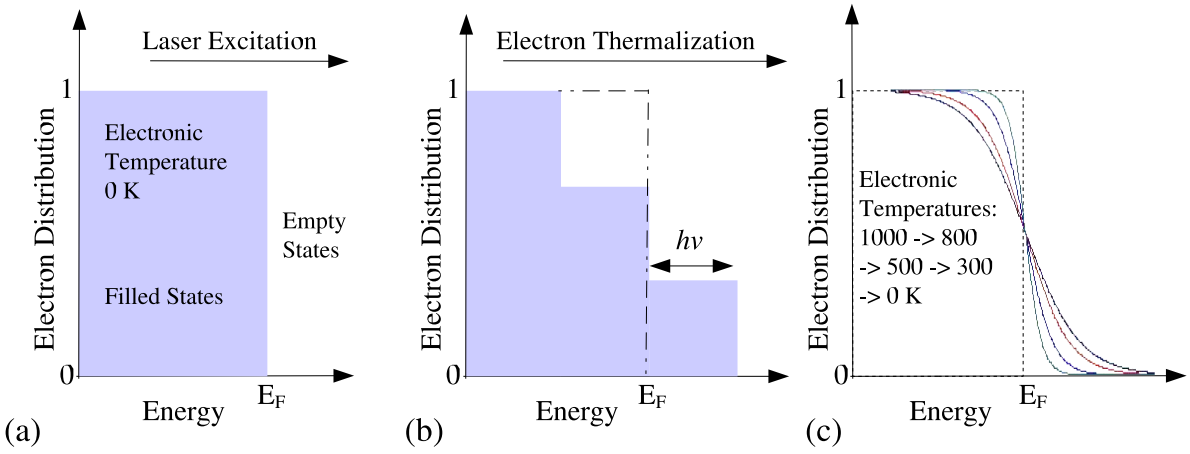

Figure 35: Schematic illustration of electrons distribution in metallic nanocrystals conduction band. (a) Before laser excitation, all energy states below the Fermi level are occupied, while all states above the Fermi level are unoccupied. This is the distribution at $T = 0\,K$; zero temperature is chosen for simplicity. (b) After laser pulse excitation, electrons with energies of up to the excitation energy below the Fermi level will be excited into states above the Fermi level having maximum energy equal to the excitation energy $h\nu$. The resulting electron distribution is nonthermal with regard to Fermi-Dirac statistics. This distribution relaxes by electron-electron scattering without losing the absorbed photon energy. (c) Electron-phonon coupling and phonon-phonon interactions with the surrounding medium cool the hot electron gas as shown by the curves drawn at low temperatures.

$$C_1 \frac{\partial T_1}{\partial t} = g\,(T_e - T_1), \tag{63}$$

where C_e and C_1 are the electronic and lattice heat capacities, respectively, g is the electron-phonon coupling constant, and κ' is the electronic thermal conductivity. $LP(Z,t)$ is the spatial and temporal evolution of the exiting laser pulse. The new electron distribution in the metal conduction band after the rapid internal electron relaxation due to electron-electron collisions is given by Fermi-Dirac statistics. Each Fermi electron distribution is associated with an electronic temperature. Therefore, the energy relaxation of hot electrons into the lattice motion is followed by its electronic temperature.

The change in the electronic energy distribution within the metal conduction band is shown in Figure 35. Only the intraband excitations are considered in this picture. The electron distribution f is calculated using the Fermi-Dirac statistics. Laser pulses excite electrons having an energy less than or equal to the pulse energy below the Fermi level to

electronic levels up to the laser pulse energy above the Fermi level. Figure 35(b) shows the corresponding electron distribution after excitation. Electron-electron scattering between the hot electrons occurs until a new Fermi distribution with higher electron temperature is reached, Figure 35(c). Electron-electron interactions are elastic, and the total energy is conserved during this first relaxation process. A equilibrium temperature between the electron and the lattice subsystems then is established through the phonon path [64, 65]. As the excited electrons above the Fermi level now lose their energy to phonons, with the assumption of heat release to the surroundings, the Fermi distribution narrows down until a distribution shown in Figure 35(a) is reached.

Electron-phonon relaxation times of the order of a few picoseconds are measured for gold thin films. Transient optical absorption spectroscopy is used to measure the effect of size on the electron-phonon coupling. The reduction in size and dimensionality of the material introduces new boundaries on electron motion. Enhanced electron-surface scattering is a proposed mechanism for the dephasing of the coherent plasmon oscillation and also could be used to explain the energy relaxation of hot electrons. The reduction in the density of electron and phonon states further alters the relaxation dynamics in these zero-dimensional systems. For gold nanocrystals in the size range of 10-100 nm, the average energy level spacing in the conduction band is smaller than the room temperature thermal energy. Quantum size effects on the hot electron dynamics are therefore expected to occur only in very small gold clusters.

5.2.1 Electron-Phonon Relaxation

The initial goal of studying electron-phonon relaxation dynamics in nanocrystals is to answer the question of how hot electron dynamics might change with nanocrystal size and shape. Confinement enhanced electron-surface scattering was thought to be the mechanism responsible for the plasmon band broadening in metallic nanocrystals intrinsic region. Femtosecond transient absorption experiments are performed to determine whether electron-surface scattering is an inelastic process, and thus it contributes to the energy relaxation of hot electrons in very small metal nanocrystals. In gold and sliver, the electron mean

path is about 40-50 nm. Therefore, if the electron-surface scattering becomes an important relaxation mechanism for small nanocrystals, the measured electron-phonon relaxation time should increase with decreasing nanocrystal size. Experimental studies of electron dynamics on 48 and 15 nm gold nanocrystals show no change in the electron-phonon relaxation rate [66]. Moreover, the relaxation dynamics seem to be independent of the nanocrystal shape or even the specific plasmon mode. Experimental results show that the measured electron-phonon relaxation rates are independent of size and shape for gold nanocrystals in the investigated size range, diameter > 15 nm. This result would exclude the fact that electron-surface scattering is the dominant mechanism for hot electron relaxations in small gold nanocrystals.

For thiol-passivated very small gold nanocrystals with diameters 1.9, 2.6 and 3.2 nm, no size dependence of electron-phonon relaxation has been observed [67]. The spectral changes in the transient absorption signal of these nanocrystals are attributed to the very low available density of states, molecular-like energy levels. Other similar work on gold nanocrystals between 4 and 120 nm show that electron-phonon relaxation rate is independent of nanocrystals sizes. For silver nanocrystals with diameter greater than 6 nm, electron-phonon coupling constant and the electronic and lattice specific heats are found to be size independent [68]. On the other hand, for tin nanocrystals with diameters of 2, 4, and 6 nm in Al_2O_3 matrix, electron-surface scattering is found to be size-dependent [69]. Experimental measurements show decreasing electronic lifetimes with decreasing nanocrystals sizes. The decrease in liftimes is attributed to an increase in electron-surface scattering in tin nanocrystals, since the mean free path is about 4.4 nm. Similar experimental measurements show size-dependent hot electron relaxations in solid and liquid gallium nanocrystals, which have mean diameters of 5, 7, and 9 nm [70]. The result is attributed to confinement enhanced electron-surface scattering in these systems. For Au_{13} and Au_{15} clusters, electron-phonon coupling is found to be size-dependent when compared with 15 nm diameter gold nanocrystals [71].

A model is proposed to describe the size-dependence of electron dynamics in metal clusters in which the relaxation dynamics of the photoexcited electron gas are described by two competing processes [1]. These processes are the electron-phonon coupling decreases

and the electron-surface scattering increases as the size of nanocrystals decreases. These two competing processes will ultimately determine the lifetimes of hot electrons. Electron surface scattering occurs by coupling between electrons and two kinds of surface modes, acoustic and capillary. The acoustic mode changes the volume, while the capillary deviates the shape of the particle. These mechanisms occur at the same time, therefore, the effective electron-phonon coupling constant is given by

$$g_{eff} = g_{Bulk} + g_A + g_c, \tag{64}$$

where the last two terms are the acoustic and capillary surface mode coupling terms, respectively. g_{Bulk} is the bulk contribution term and is equal to $2.95 \times 10^{16}\,\mathrm{Wm^{-3}K^{-1}}$, as measured for bulk gold [72]. Hot electrons are assumed to be in a potential well with the dimension of the nanocrystal and with depth V_0, which is the Fermi energy. The coupling constant between electrons and the capillary mode is given by [2]

$$g_c = \frac{3}{16\pi}\, k_B\, \frac{\nu_F}{R}\, n\, \frac{m_e \omega_l^2}{\sigma} \left(\frac{V_0}{\varphi_0}\right)^2, \tag{65}$$

where k_B is the Boltzmann's constant, n is the free electron density, m_e is the electron mass, σ is the surface tension, φ_0 is the metal work function, and ω_l is the minimum frequency of the capillary mode, and is given by

$$\omega_l = \sqrt{\frac{\sigma}{\rho R^3}\, l\,(l-1)\,(l+2)}, \tag{66}$$

where ρ is the density of the metal, and l is the angular momentum of the shortest capillary mode, which is given by the integer part of $\pi R/d$ where d is the lattice parameter. The energy loss associated with excitation of the acoustic surface modes is given by [2]

$$g_A = \frac{1}{16\pi}\, k_B\, \frac{\nu_F}{R^2}\, n\, \frac{m_e}{\rho} \left(\frac{\omega_D}{c_l}\right)^2 \left(\frac{V_0}{\varphi_0}\right)^2, \tag{67}$$

where c_l is the longitudinal speed of sound in the material, and ω_D is the Debye frequency.

The calculated coupling constants for different Au nanocrystals sizes are listed in Table 2. Since both g_A and g_c are inversely proportional to the nanocrystals radius, the model predicts the relaxation rate to increase as nanocrystal size decreases. Also, the contribution of the capillary modes to electron relaxation is much larger than that for the acoustic

Table 2: Electron-surface and effective electron-phonon coupling constants ($Wm^{-3}K^{-1}$) calculated with the model of Beloskii and Tomchuk [1, 2].

Nanocrystal radius (nm)	g_c	g_A	g_{eff}
1.3	1.75×10^{15}	5.57×10^{14}	3.18×10^{16}
2.3	9.97×10^{14}	1.64×10^{13}	3.05×10^{16}
4.2	1.58×10^{14}	5.05×10^{12}	2.97×10^{16}
Bulk			2.95×10^{16}

modes. The calculations using this model show that the energy loss to the surface modes does not form a substantial value of the effective electron-phonon coupling constant g_{eff} for Au nanocrystals with diameter $> 2\,nm$. These results of the calculations performed using this model are in good agreement with the available experimental data for Ga, Ag, and Au nanocrystals [70, 73, 74]. For all of these materials, the surface coupling is dominated by g_c.

The magnitude of g_c for different metals is mainly determined by the ratio of the electron density to the metal density (n/ρ) . Therefore, for Au ($n/\rho = 3.1 \times 10^{21} g^{-1}$), which has large atomic mass, would have a smaller electron-surface coupling than Ga ($n/\rho = 2.6 \times 10^{22} g^{-1}$) or Ag ($n/\rho = 5.6 \times 10^{21}\ g^{-1}$). According to this model, the physical description of the above mentioned experimental results is that electron-surface scattering would not result in significant displacement of the surface atoms from their equilibrium position for heavy elements, such as Au. This implies that the surface phonon modes will not be efficiently excited by electrons collision, and the amount of energy transfered to these modes from the hot electrons is very small. On the other hand, in metals with high density of free electrons such as Ga, the number of electron-surface scattering event is larger, and thus energy transfer to phonons is larger. Likewise, metals with small atomic mass will have larger electron-phonon coupling.

The gold nanocrystals used in our BEES studies are mixtures of different stable clusters. Thes clusters were capped with dodecanethiol ($C_{12}H_{25}SH$) organic molecules. Optical and STS measurements on these clusters show a molecular-like energy levels structure [75]. The optical absorption spectra of 28 kDa gold nanocrystals is well structured with distinct

absorption onset near 1.31 eV (950 nm) corresponding to the electronic energy gap between the HOMO and LUMO. Femtosecond transient absorption studies on 28 kDa further show an induced transient absorption instead of a plasmon band bleach with a double-exponential decay that is independent of the laser pump power [29]. For the 28 kDa nanocrystals, hot electrons relaxation times from the initially excited energy state to the LUMO or band gap level is measured on the subpicosecond scale (750 fs). Furthermore, the radiative or nonradiative recombination from the band edge to the final relaxation of the these clusters takes place on a much longer time scale, nanosecond to microsecond. These observations indicate a molecular-like response with single electron excitation.

The relaxation times of hot electrons in gold nanocrystals are sensitive to both electron-phonon coupling and electron-surface scattering. These two processes seem to compete as the nanocrystals sizes decrease. In large and small (diameter $>$ 2 nm) nanocrystals, the weak electron-phonon coupling dominates surface-scattering, resulting in slower electronic relaxation relative to the bulk. However, in very small nanocrystals, the relaxation times are significantly slower, reflecting that of the molecular system.

Our hot electron dynamics studies on a single 28 kDa nanocrystal show electron relaxations times $\leq$ 16 picoseconds. These relaxations are not mediated by electron-hole interaction in the nanocrystals as compared with optical studies. In the absence of holes, hot electrons in single isolated nanocrystal can relax through electron-electron scattering. surface-scattering, or phonon coupling. As mentioned in earlier discussions, electron-phonon coupling is expected to dominate surface scattering because of the large atomic mass of gold and the small electron density in the nanocrystal. The subpicosecond relaxation times reported by femtosecond dynamics measurements on the 28 kDa nanocrystals are in good agreement with intraband relaxations in semiconductor nanocrystals in the presence of an optically created hole. This relaxation mechanism is mediated by electron-hole interaction, which involves transfer of the electron excess energy to a hole, with a subsequent fast hole relaxation through its dense spectrum of states [47]. These relaxation rates are reduced by a factor of ten when electrons are chemically injected to the nanocrystal excited states, no holes are available in the nanocrystal [48]. In our studies, electrons are injected into

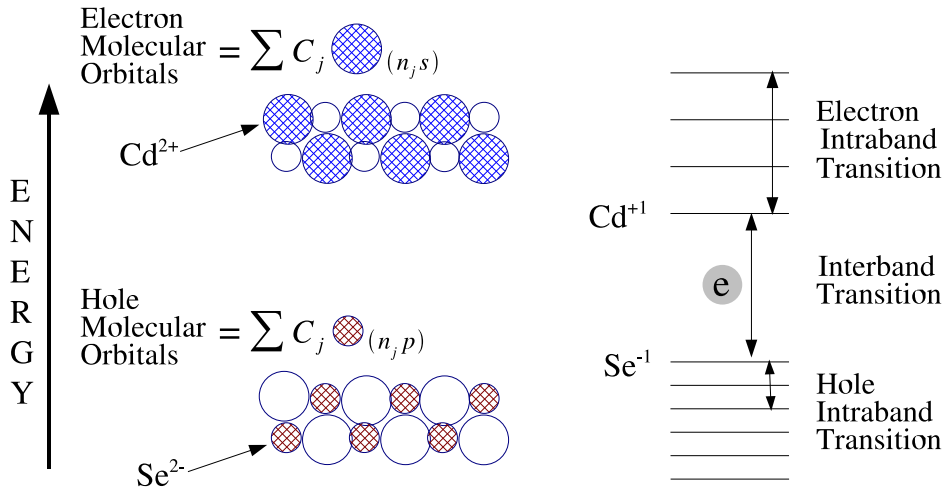

Figure 36: Molecular orbitals in semiconductor nanocrystals are different from those in a conducting polymer: (left) The molecular orbitals of the hole (bottom) in the Se^{2-} electronic system and the electron (top) in the Cd^{2+} electronic system in a CdSe semiconductor nanocrystal. (Right) The band gap (interband or HOMO to LUMO) transition (separating the electron and hole) and the different intraband transitions of the electron (top) and hole (bottom) in a semiconductor nanocrystal. The interband transition involves a charge transfer from the Se^{2-} MOs to the Cd^{2+} MOs and forms a delocalized Cd^{+} and Se^{-} electronic system in the band gap state.

the nanocrystals from the STM tip, therefore, electron relaxations are not mediated by electron-hole interactions. Our measured lifetimes of hot electrons in 28 kDa are comparable to intraband relaxations of chemically injected electrons in semiconductor nanocrystals. This shows that the presence of molecule-like energy levels and the HOMO-LUMO gap in these systems make their hot electron dynamics similar to that of semiconductor nanocrystals.

5.3 Nonradiative Relaxations in Semiconductor Nanocrystals

Optical excitations of neutral semiconductor nanocrystals and conjugated molecules result in the creation of an electron-hole pair. In both systems, molecular orbitals can describe the electronic excitation process. However, their formed molecular orbitals are different. In conjugated molecules, the occupied and the unoccupied molecular orbitals (MO) are made of linear combination from the same type of atoms, thus the molecules are strongly correlated. In semiconductor nanocrystals such as CdSe and CdS, the occupied MOs are made of linear

combination of atomic orbitals on the negatively charged anions (e.g., Se^{2-}, S^{2-}), while the unoccupied MOs are made of atomic orbitals on the metallic cations (Cd^{2+}) as shown in Figure 36. Therefore, the bandgap electronic excitation involves a charge transfer of an electron from the HOMO of the Se^{2-} or S^{2-} electronic system to the vacant LUMO of Cd^{2+}. This process creates a hole in the HOMO, top level in the bulk valence band. Thus, the holes always occupy the anion MOs, while the excited electrons occupy the cation MOs. Due to this process and the high dielectric constant of semiconductor materials, the charge carriers in semiconductor nanocrystals are weakly coupled. Electrons and holes in semiconductors can be excited, be trapped, and relax nonradiatively independent of one another. Furthermore, intraband excitations of electrons take place between different MOs of the metal cation, whereas, those for the holes take place in the higher energy anion MOs. The bandgap excitations are called interband excitations and are shown schematically in Figure 36. In II-VI semiconductors, the different MOs made from the atomic orbitals of the anions are larger than those formed from the atomic orbitals of cations. This is why the electron intraband absorption occurs at higher energy than the hole intraband absorption.

The mechanisms of hot electron relaxations in nanocrystals are currently an active research topic. In the bulk system, excited electrons in the conduction band can relax by releasing energy to the lattice phonons as they relax down to the bandgap level. This is possible because the electronic energy level separations in the conduction band are small and less than the room temperature energy. As electronic quantization takes place due to quantum confinement, electrons in nanocrystals acquire fixed energy values. Therefore, electrons can only exchange a quantized amount of energy with the lattice as it relaxes down to the bandgap level. These electronic excitation energies are very large (fraction of an electron volt) as compared with the phonon energy at room temperature ($0.025\ eV$). Therefore, as electrons relax down from one energy level to the other, they releases energy that requires the simultaneous excitation of 10 or more phonons. Such a process is improbable and slows down the electronic relaxation leading to phenomenon known as the phonon bottleneck. However, the observed electronic relaxations in nanocrystals are found to be on the order of subpicosecond to picosecond time scale, and thus, other mechanisms must be

involved in relaxing the hot electrons.

5.3.1 Size Dependence of Intraband Relaxations Rates

In bulk semiconductors, hot electrons energy relaxations are dominated by the interaction with longitudinal optical phonons. That interaction leads to a fast carrier cooling, typically on a subpicosecond time scale [76]. In nanocrystals systems, even in the weak quantum confinement regime where the energy levels separation is about 10 meV, the carrier relaxations mediated by interactions with phonons are reduced dramatically because of restrictions imposed by energy and momentum conservations [52]. In the regime of strong quantum confinement, the energy levels separation can be much larger than optical phonon energy, and therefore further reduction is expected on the hot electrons energy loss rate. In the strong regime, electron-phonon scattering can only occur via weak multiphonon processes.

Despite of the above theoretical predictions, many recent experiments report that carrier relaxations in nanocrystals are not significantly slower than in bulk materials [77, 78]. Moreover, the existence of the phonon bottleneck in three dimensionally confined systems is being questioned by recent experimental studies of the electron intraband relaxations in CdSe nanocrystals [54]. These studies report subpicosecond *1P-1S* electron relaxation times in nanocrystals for which the *1S-1P* energy separation is more than 10 longitudinal optical phonons energies.

Femtosecond transient absorption spectroscopy provides measurements of the *1P-1S* intraband relaxation rates. Intraband relaxation in colloidal CdSe nanocrystals is found to increase as the size of nanocrystals decreases. Furthermore, the energy loss rate in nanocrystals is found to be orders of magnitude larger than the rate expected for the multiphonon emission mechanisms [79]. The fast relaxations and the confinement induced enhancement in the relaxation process clearly indicate that energy relaxations in nanocrystals are dominated by mechanisms other than phonons.

Recent works propose that coupling to defects outside the nanocrystals, Auger interactions with carriers outside the nanocrystals or Auger-type electron-hole energy transfer

can lead to fast relaxation not limited by the phonon bottleneck. However, recent experimental work indicates that in colloidal nanocrystals, energy relaxation does not show any dependence on surface properties. Moreover, the relaxation rate remains almost identical for different liquids and solid matrices.

5.3.2 Quantum Confined Auger Relaxation

The excitation of a near surface atom results in the ejection of of low-lying electron and creates a hole state in the atomic levels. A higher energy electron recombines with this hole state and releases some energy. This released energy in the electron-hole recombination can be emitted as a photon (radiative decay) or as an electron in the nonradiative Auger process. Auger process can occur in bulk semiconductor where the emitted (re-excited) particle can be either an electron or a hole [80]. At high laser intensities, more than one electron-hole pair can be excited. In the case of two electron-hole pairs being excited, the repulsion between the two excited electrons and the attraction of one of them to the hole leads to the recombination of one of the electrons-hole pairs. The energy released in this recombination process ionizes the other electron. This is known as the Auger process and usually results in the relaxation of the two excited electrons. Hot electrons relaxations through the Auger process is observed experimentally in different semiconductor nanocrystals at reasonably high excitation laser intensities [78].

The efficiency of Auger processes, which are mediated by Coulomb interaction, is different in an atomic system than in a bulk semiconductor. In an atomic system, the electron-electron coupling is stronger than electron-photon coupling, thus the rate of Auger transitions are significantly larger than the radiative transition rates. As a result, the decay of multi-electron states in atomic systems is dominated by Auger processes. The efficiency of Auger effects is reduced in bulk materials because of the reduced Coulomb electron-electron interaction. In the transformation from bulk to atomic regime, Auger effects are therefore expected to change as matters evolve from atoms to bulk materials. Since nanocrystals have sizes in between molecules and bulk, the confinement induced modifications in Auger interactions can be studied using nanocrystals samples with different sizes.

Carrier confinements in three dimensions result in discrete atomic-like energy levels and a modification of the multiparticle interactions [47, 81]. Quantum confinements result in an enhancement in Coulomb interactions and lead to increased Auger rates in comparison with bulk materials. On the other hand, the atomic-like structure of nanocrystals is expected to hinder the Auger processes because of the reduced availability of final states satisfying energy conservation. As a consequence, Auger recombination can only occur efficiently through the involvement of a phonon or a final state outside the nanocrystal (Auger ionization). These two competing effects complicate the theoretical analysis of quantum confined Auger recombination and stress the need for experimental mapping of the size-dependent Auger rates.

In bulk system, Auger recombination is characterized by a continuum of density dependent recombination times $\tau = (C_A n_{eh}^2)^{-1}$. However, in a confined system, Auger recombination is characterized by a set of recombination constants, characteristic of the decay of 2-, 3-, ..., e-h pair nanocrystals. The extracted dynamics [82] of the 2-, 3-, 4-electron-hole pair states indicate that the carrier decay becomes progressively faster with increasing the number of e-h pairs per nanocrystals. This is an expected trend for the Auger recombination process. In the case of bulk semiconductor, the effective decay time constant τ_N in the Auger regime is given by $\tau_N^{-1} = C_A(N/V_0)^2$ $(N \geq 2)$. This expression predicts a ratio of $\tau_4 : \tau_3 : \tau_2 = 0.25 : 0.44 : 1$, which is very close to the ratio $0.22 : 0.47 : 1$ of experimentally determined times of the 4-, 3-, 2-pair relaxation (10, 21, and 45 ps, respectively). The quantitative match of scaling for the multiparticles relaxation times indicates that the decay rates for quantum-confined Auger recombination are cubic with respect to the carrier density $(dn_{eh}/dt \ \propto) \ -n_{eh}^3$, the same for bulk materials.

Transient absorption measurements on CdSe nanocrystals of different sizes indicate that the τ_2 time constant rapidly decreases with decreasing nanocrystals size following a cubic size dependence $(\tau_2 \ \propto \ R^3)$ [82], $\tau_2 = 363$ ps in nanocrystals with $R = 4.1$ nm and reduces down to 6 ps for nanocrystals with $R = 1.2$ nm. The time constant measured for the 3- and 4-pair decay follows the same size dependence as that of the 2-pair state. This implies that the time constant ratios predicted by the semiconductor model hold for all nanocrystals sizes.

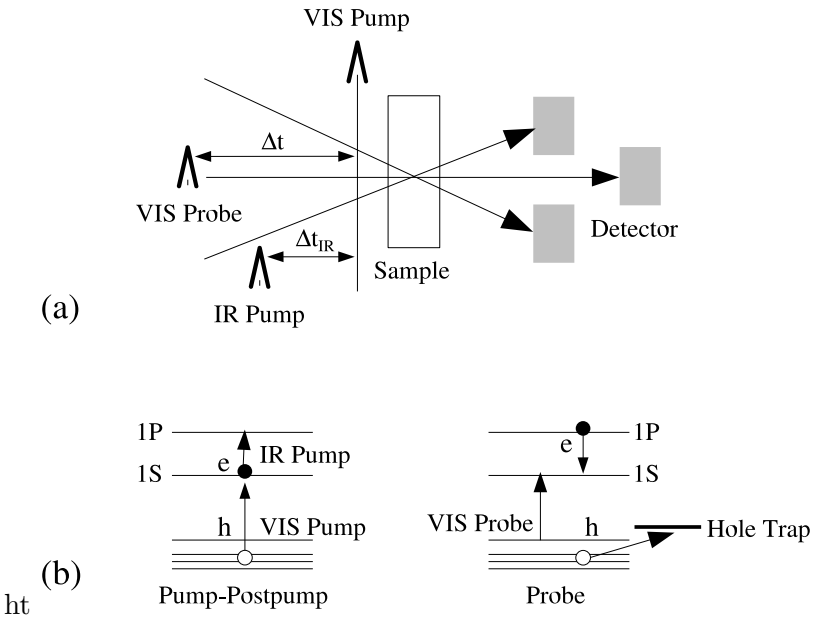

Figure 37: Three-pulse pump-probe experiments for intraband relaxations. (a) Schematics of a three-pulse pump-probe experiment and the excitation and relaxation processes monitored in it. (b) An electron-hole pair is created via an interband excitation using a pump pulse in the visible spectrum. Electrons are re-excited within the conduction band by infrared postpump. Electrons relaxing back to the ground state are monitored with a third pulse probing the interband absorption changes. Surface capping molecules are used to trap holes immediately after photoexcitation

The enhancement in the Auger decay rate in nanocrystals is therefore due to an effective increase in carrier concentrations resulting from the increased spatial confinement on the carriers. However, the R^3 size dependence of the relaxation times measured experimentally is in disagreement with the R^6 dependence predicted by the bulk-semiconductor model, which implies that in a three dimension confined system, the Auger constant depends on the nanocrystals size.

5.3.3 Electron-Hole Interactions and Intraband Relaxation

Due to the large surface-to-volume ratio in nanocrystals, both electron and hole wave functions are strongly affected by the nanocrystals surface properties. This surface effect can be used to spatially separate electrons and holes by passivating nanocrystals surfaces with electron accepting [83] or hole accepting molecules [84]. A model for the electron-hole mediated relaxation is proposed by Efros [47]. In this model, the excited electron is always

coupled with the hole. As electron relaxes to a lower energy state, it gives some of its energy to the hole. The hole energy level spacing is known to be much smaller than the electron energy spacing, thus there is no energy mismatch problem in the relaxation process. The hole relaxes its energy by a phonons bath.

Pyridine coated CdSe nanocrystals have been prepared as a system to study the effect of electron-hole coupling on intraband relaxations. In this system, pyridine acts as an efficient hole acceptor, and as a result the electron-hole coupling is strong immediately after photoexcitation and is reduced dramatically after the hole is transferred to a capping group on the nanocrystal surface. This mechanism is expected to have a strong effect on electron intraband relaxation if it is mediated by electron-hole interactions.

Electron intraband dynamics can be monitored using a three-pulse femtosecond transient absorption experiment. In this experiment, the sample is excited by a sequence of two ultrashort pulses (one in the visible and another in the infrared spectral range) and is probed by a broad-band pulse of a femtosecond white light. Using this technique, the Klimov group compared the intraband electron dynamics of ZnS capped nanocrystals with that of pyridine capped nanocrystals [85]. The group found dramatic changes in the electron relaxation of pyridine capped nanocrystals. Electron intraband relaxations were slowed down by a factor of 10 in the pyridine samples because electron-hole coupling is reduced after hole transfer to the pyridine molecule. However, even in the charge separated system, electrons relax down to the ground state on a picosecond time scale, which is much faster than expected for phonon-dominated relaxation. This indicates that even in the case of significant spatial separation between an electron and a hole, Coulomb electron-hole interactions can be strong enough to provide an efficient channel for energy losses. This is possible because Coulomb coupling does not require a direct overlap between electron and hole wave functions and scales relatively slowly with the electron-hole separation.

In order to have a more accurate understanding of the intraband relaxations mechanisms, Nozik's group prepared and studied a system in which only carrier is present [48]. N-type nanocrystals represent a system in which intraband electron relaxations are studied in the absence of holes. Sodium biphenyl is a very strong reducing agent that is used to chemically

inject electrons into the conduction band of InP nanocrystals. After their chemical injection, electrons are present in the lowest unoccupied energy level, $1S_e$. This $1S_e$ electron may be excited to the $1P_e$ level with an infrared pump signal. The effect of hole on the electron intraband relaxation is understood by comparing the intraband electron dynamics of a neutral and n-type nanocrystals. Only the infrared pump is necessary to pump the $1S_e$-$1P_e$ transition in the n-type nanocrystals sample. The relaxation of electrons in the n-type sample is slowed by a factor of ten when compared to the neutral nanocrystals sample.

In n-type nanocrystals, no holes are present to facilitate relaxation through Auger-like electron-hole energy transfer. It is expected and experimentally observed that the fast time constant is absent from the relaxation dynamics. In the absence of a core-confined hole, intraband electron relaxations are slowed by an order of magnitude. The relaxation rate obtained is in agreement with relaxation rates assigned to electronic relaxation through the interaction with a surface localized holes. Therefore, electron-hole interactions are not important unless the surface is completely free of electron and hole traps. In very small nanocrystals, electron-hole interaction will not compete with mechanisms involving the surface. Surface defects are difficult to discard especially when studying ensembles of nanocrystals in solutions. In addition to defects and solution impurities, the capping materials, which are usually large organic molecules, can absorb some of the hot electrons energies in a few vibrations. Therefore, the interaction between the excited electrons and the capping molecules could lead to the relaxation of the excited electons.

To complement the optical measurements on semiconductor nanocrystals mentioned in this section, our BEES measurements on single gold nanocrystals show that hot electron relaxations are on the order of several picoseconds time scale. In metal nanocrystals, the density of states is much larger than semiconductors, therefore hot electrons relaxations are expected to be much faster than in semiconductors. However, since our gold nanocrystals are very small their energy level spacing is much higher than phonon energies at room temperatures, and relaxations through phonons are slowed down due to energy mismatch. In fact, optical measurements on these nanocrystals have shown molecular-like energy levels structure with a HOMO-LUMO energy gap [35]. Our measurements were performed on

single isolated nanocrystals, and thus solutions impurities, which usually work as electrons traps, are absent as compared to optically studied samples. Furthermore, in BEES studies, electrons are injected into the nanocrystals from an external source (STM tip). The presence of core-confined holes during our measurements is possible only if the first tunneling event takes place through discharge of the nanocrystal. This event creates a hole in the nanocrystal. As the voltage is increased, the second tunneling event would correspond to a transfer of an electron from the tip to the nanocrystal. The electron is transfered into an energy level above the Fermi level of the nanocrystal. This electron is coupled to the hole and may relax to a lower energy level through electron-hole interaction. On the other hand, if the first tunneling event corresponds to electron transfer from tip to the nanocrystal, then the nanocrystal is always charged. Therefore, there are no core-confined holes in the nanocrystals, and mechanisms other than electron-hole coupling are responsible for the relaxation. These mechanisms include the coupling of hot electrons to the capping organic molecules, where the coupling leads to the relaxation of excited electrons through the vibration of these molecules.

CHAPTER VI

CONCLUSION

6.1 Summary of System Designs

The first step of this research is rebuilding the low temperature STM and redesigning some of its features for better performance and for BEES measurements capabilities. Following are some of the redesigns introduced to the STM. First, an exchange gas cylinder is designed and mounted around the microscope can. The cylinder is designed to reduce the acoustic coupling of the microscope. In addition, the cylinder can electrically shield the microscope wires. During the cooling of the STM, the cylinder is filled with a few hundred millitorr of helium to enhance thermal cooling and is submerged in the cooling liquid. Second, the elevator guiding pin that was made out of sapphire is replaced with a new one made out of bronze. The bronze provides more stiffness and less friction with stainless steel. Third, the sample jig is machined to form two separate electrically isolated supports. The supports are wired and used in measuring both the tunneling and BEES current simultaneously. Fourth, a new sample holder is designed and machined for BEES measurements. The holder is designed to establish electrical contacts with both the top and bottom of the sample. The microscope performance initially is tested with gold on mica substrate. The atomic resolution and calibration of the STM are tested by imaging the 7×7-Si(111) surface reconstruction.

6.2 Summary of Results

Samples for BEES experiments are fabricated in the clean rooms successfully. Each sample consisted of thermally deposited $\sim 10\,\text{nm}$ gold film on a $\sim 400\,\mu\text{m}$ thick Si(111) substrate. The IV of the Schottky barrier of these samples is always tested before their transfer to the microscope chamber. Nanocrystals are deposited successfully from solution onto the

xylenedithiol SAM coated gold film. STM images of these nanocrystals at 77 k show immobile single isolated nanocrystals with different sizes.

Tunneling spectroscopy on 8 kDa gold nanocrystals using lock-in detection resolved two peaks on both sides of zero bias that are separated by about 190 meV. This separation is less than the charging energy, and therefore these peaks are attributed to tunneling through the energy levels of the nanocrystal. Free electron picture of metal with spin degeneracy results in about 170 meV for the average energy level spacing in the 8 kDa nanocrystals. Measurements of the dI/dV at different tip-nanocrystal separations show a decrease in the Coulomb blockade as the tip is retracted. The Coulomb blockade decreases since the tip-nanocrystal capacitance is smaller than the nanocrystal-substrate capacitance; and as the tip is retracted, energy levels become accessible at lower energy. In addition, the decrease in Coulomb blockade with tip retraction implies that the first tunneling event in our tunneling configuration corresponds to electron charging of nanocrystals. Therefore, electron relaxations are not mediated by electron-hole interaction.

A newly developed nanocrystals BEES technique is used successfully to characterize single nanocrystals. BEES spectrum taken on a single gold nanocrystal shows BEES current attenuation as compared with with BEES taken on a nanocrystal-free region. The attenuation is due to hot electron inelastic scattering and hence energy loss in the nanocrystals. In addition, BEES on a single 28 kDa gold nanocrystal shows a shift in threshold as compared with BEES on the substrate. The threshold shift is attributed to electron relaxation into an energy level below the Schottky barrier. On the other hand, BEES spectrum taken on a single 8 kDa gold nanocrystal shows threshold similar to that taken on the substrate. However, BEES on the 8 kDa nanocrystals rolls over at high voltages as compared with BEES on the substrate. The roll-over is possibly due to an increase in charging configurations that results in relaxation enhancement, hence electrons lose energy in the nanocrystal, and their transmission at the metal/semiconductor interface becomes lower.

A comparison of BEES and tunneling IV spectra taken on the same nanocrystal shows some interesting correlation. BEES current is enhanced at voltages corresponding to the position of charging peaks in the tunneling IV. Moreover, BEES current is attenuated for the

voltage range between charging peaks in the tunneling IV spectrum. Hot electron lifetimes in single Au nanocrystals are measured experimentally using the newly developed BEES technique. The estimated lifetimes from BEES measurements are ≤ 16 picoseconds.

6.3 Areas for Further Study

The work presented in this thesis represents first time implementation of BEES to study electron dynamics in a single nanocrystal. BEES measurements have been performed successfully as a proof of principle. Due to the nature of the tunneling barrier in nanocrystals spectroscopy, acquiring the BEES spectra at a constant current may affect the interpretation of the data. This effect is due to the change of the tip-nanocrystal capacitance as the tip is retracted due to change in voltage. A possible solution is to acquire the BEES spectrum at constant tip-nanocrystal separation. However, since BEES spectrum is acquired at large time constant, it may be difficult to hold the servo for a long time. A possible solution is to acquire BEES spectra at a small time constant and re-servo after each spectrum.

Due to the effect of the tunneling junction parameters on the BEES measurements, a better understanding of the electron dynamics in a single nanocrystal requires a control of these parameters. An interesting measurement is to acquire BEES spectra at different tip-nanocrystals separation. Such measurements could identify the operative mechanisms in the hot electron relaxation. For example the effect of electron-hole interaction can be tested by controlling the current onset on either of the junctions. Another possible experiment for extracting the energy distribution of the tunneling-out electrons is to acquire BEES spectra on both the substrate and on the nanocrystals using lock-in detection technique. The ratio of these two spectra multipled by the derivative of the tunneling IV on the substrate is proportional to electrons tunneling-out from the nanocrystals energy states.

So far, BEES has been used to study electron dynamics in single gold nanocrystals. BEES studies of semiconductor nanocrystals with different sizes and shapes should reveal valuable information about their electron dynamics. This is because of the following. First, semiconductor nanocrystals have large bandgap; therefore, the lowest excited state in the conduction band is well above the Schottky barrier. Second, through the control of the

tunneling junction parameters, it should be possible to switch the current onset between the two junctions. In this way the effect of electron-hole interaction on electron relaxation can be studied in a single nanocrystal.

In fact, during the course of my study, we tried to prepare and image samples of semiconductor nanocrystals. These samples included CdSe and CdS. However, due to the gold surface roughness and possibly the weak binding between the nanocrystals and the SAM, it was not possible to acquire good images of these samples.

REFERENCES

[1] E. D. Belotskii and P. M. Tomchuk. "Electron phonon interaction and hot-electrons in small metal islands." Surf. Sci. **239** (1-2), 143–155 (1990).

[2] E. D. Belotskii and P. M. Tomchuk. "Surface electron phonon energy exchange in small metallic particles." Int. J. Elect. **73** (5), 955–957 (1992).

[3] L. E. Brus. "Electron electron and electron-hole interactions in small semiconductor crystallitesthe size dependence of the lowest excited electronic state." J. Chem. Phys. **80** (9), 4403–4409 (1984).

[4] H. D. R. Bohren Craig F. *Absorption and Scattering of Light by Small Particles* (Wiley Science Paperback Series, New York, 1983).

[5] T. G. Schaaff, G. Knight, M. N. Shafigullin, R. F. Borkman, and R. L. Whetten. "Isolation and selected properties of a 10.4 kDa gold : Glutathione cluster compound." J. Phys. Chem. B **102** (52), 10 643–10 646 (1998).

[6] A. T. Johnson, L. P. Kouwenhoven, W. Dejong, N. C. Vandervaart, C. J. P. M. Harmans, and C. T. Foxon. "Zero-dimensional states and single electron charging in quantum dots." Phys. Rev. Lett. **69** (10), 1592–1595 (1992).

[7] V. J. Goldman, B. Su, and J. E. Cunningham. "Single-electron tunneling in double-barrier nanostructures." Intern. J. of Mod. Phys. B **6** (13), 2321–2343 (1992).

[8] M. J. Hostetler and R. W. Murray. "Colloids and self-assembled monolayers." Current Opinion in Colloid & Interface Science **2** (1), 42–50 (1997).

[9] A. P. Alivisatos. "Semiconductor clusters, nanocrystals, and quantum dots." Science **271** (5251), 933–937 (1996).

[10] U. Banin, Y. W. Cao, D. Katz, and O. Millo. "Identification of atomic-like electronic states in indium arsenide nanocrystal quantum dots." Nature **400** (6744), 542–544 (1999).

[11] D. Averin and K. K. Likharev. *Mesoscopic Phenomena in Solids*, chapter 6 (Elsevier, Amsterdam, 1991).

[12] M. H. D. Hermann Grabert, editor. *Single Charge Tunneling* (New York: Plenum, 1992).

[13] G. Binnig and H. Rohrer. "Scanning tunneling microscopy." Helvetica Physica Acta **55** (6), 726–735 (1982).

[14] L. E. Harrell and P. N. First. "An ultrahigh vacuum cryogenic scanning tunneling microscope with tip and sample exchange." Rev. Sci. Instrum. **70** (1), 125–132 (1999).

[15] L. E. Harrell. *Investigation of Gold Nanocrystals by Ultrahigh Vacuum Cryogenic Scanning Tunneling Microscopy.* Ph.D. thesis, Georgia Institute of Technology (1998).

[16] G. Binnig, H. Rohrer, C. Gerber, and E. Weibel. "7x7 reconstruction on Si(111) resolved in real space." Phys. Rev. Lett. **50** (2), 120–123 (1983).

[17] K. Takayanagi, Y. Tanishiro, M. Takahashi, and S. Takahashi. "Structural-analysis of Si(111)-7x7 by uhv-transmission electron-diffraction and microscopy." J. Vac. Sci. Technol. A Vac. Surf. Films **3** (3), 1502–1506 (1985).

[18] M. T. Reetz, W. Helbig, S. A. Quaiser, U. Stimming, N. Breuer, and R. Vogel. "Visualization of surfactants on nanostructured palladium clusters by a combination of stm and high-resolution tem." Science **267** (5196), 367–369 (1995).

[19] J. E. Coury, E. C. Pitts, R. Shorrosh, R. H. Felton, and L. A. Bottomley. "Characterization of zinc-sulfide nanoclusters via atomic-force and scanning-tunneling-microscopy." J. Vac. Sci. Technol. B **13** (3), 1167–1171 (1995).

[20] R. H. Terrill, T. A. Postlethwaite, C. Chen, J. E. Hutchison, C. Poon, A. Tarzis, A. Chen, M. R. Clark, C. S. Johnson, E. T. Samulski, J. M. Desimone, and R. W. Murray. "Monolayers in 3 dimensionselectron-transport dynamics in solid alkanethiol-stabilized gold colloids." Abs. of Pap. of the Amer. Chem. Soc. **210**, 380–INOR (1995).

[21] T. P. Bigioni, L. E. Harrell, W. G. Cullen, D. E. Guthrie, R. L. Whetten, and P. N. First. "Imaging and tunneling spectroscopy of gold nanocrystals and nanocrystal arrays." Eur. Phys. J. D **6** (3), 355–364 (1999).

[22] R. L. Whetten, J. T. Khoury, M. M. Alvarez, S. Murthy, I. Vezmar, Z. L. Wang, P. W. Stephens, C. L. Cleveland, W. D. Luedtke, and U. Landman. "Nanocrystal gold molecules." Adv. Mater. **8** (5), 428–& (1996).

[23] C. L. Cleveland, U. Landman, M. N. Shafigullin, P. W. Stephens, and R. L. Whetten. "Structural evolution of larger gold clusters." Zeitschrift Fur Physik D-Atoms Molecules And Clusters **40** (1-4), 503–508 (1997).

[24] M. Brust, M. Walker, D. Bethell, D. J. Schiffrin, and R. Whyman. "Synthesis of thiol-derivatized gold nanoparticles in a 2-phase liquid-liquid system." Chem. Commun. **7**, 801–802 (1994).

[25] J. A. Derose, T. Thundat, L. A. Nagahara, and S. M. Lindsay. "Gold grown epitaxially on micaconditions for large area flat faces." Surf. Sci. **256** (1-2), 102–108 (1991).

[26] R. P. Andres, J. D. Bielefeld, J. I. Henderson, D. B. Janes, V. R. Kolagunta, C. P. Kubiak, W. J. Mahoney, and R. G. Osifchin. "Self-assembly of a two-dimensional superlattice of molecularly linked metal clusters." Science **273** (5282), 1690–1693 (1996).

[27] S. Watanabe, N. Nakayama, and T. Ito. "Homogeneous hydrogen-terminated Si(111) surface formed using aqueous hf solution and water." Appl. Phys. Lett. **59** (12), 1458–1460 (1991).

[28] T. A. Fulton and G. J. Dolan. "Observation of single-electron charging effects in small tunnel-junctions." Phys. Rev. Lett. **59** (1), 109–112 (1987).

[29] S. Link, M. A. El-Sayed, T. G. Schaaff, and R. L. Whetten. "Transition from nanoparticle to molecular behavior: a femtosecond transient absorption study of a size-selected 28 atom gold cluster." Chem. Phys. Lett. **356** (3-4), 240–246 (2002).

[30] M. M. Alvarez, J. T. Khoury, T. G. Schaaff, M. N. Shafigullin, I. Vezmar, and R. L. Whetten. "Optical absorption spectra of nanocrystal gold molecules." J. Phys. Chem. B **101** (19), 3706–3712 (1997).

[31] K. K. Likharev. "Correlated discrete transfer of single electrons in ultrasmall tunnel-junctions." Ibm Journal Of Research And Development **32** (1), 144–158 (1988).

[32] M. N. D. Ashcroft, N .W. *Solid State Physics* (Saunders, Philadelphia, 1976).

[33] D. V. AVERIN and A. N. KOROTKOV. "Correlated single-electron tunneling via mesoscopic metal particles - effects of the energy quantization." J. Low Temp. Phys. **80** (3-4), 173–185 (1990).

[34] T. P. Bigioni, T. G. Schaaff, R. B. Wyrwas, L. E. Harrell, R. L. Whetten, and P. N. First. "Scanning tunneling microscopy determination of single nanocrystal core sizes via correlation with mass spectrometry." J. Phys. Chem. B **108** (12), 3772–3776 (2004).

[35] T. G. Schaaff, M. N. Shafigullin, J. T. Khoury, I. Vezmar, R. L. Whetten, W. G. Cullen, P. N. First, C. GutierrezWing, J. Ascensio, and M. J. JoseYacaman. "Isolation of smaller nanocrystal Au molecules: Robust quantum effects in optical spectra." J. Phys. Chem. B **101** (40), 7885–7891 (1997).

[36] W. Schottky. "Discrepencies in Ohm's laws in semiconductors." Physikalische Zeitschrift **41**, 570–573 (1940).

[37] R. H. Williams. "Metal-semiconductor interfaces." Surface Science **251**, 12–21 (1991).

[38] L. D. Bell and W. J. Kaiser. "Observation of interface band-structure by ballistic-electron-emission microscopy." Phys. Rev. Lett. **61** (20), 2368–2371 (1988).

[39] W. J. Kaiser and L. D. Bell. "Direct investigation of subsurface interface electronic-structure by ballistic-electron-emission microscopy." Phys. Rev. Lett. **60** (14), 1406–1409 (1988).

[40] D. K. Guthrie, L. E. Harrell, G. N. Henderson, P. N. First, T. K. Gaylord, E. N. Glytsis, and R. E. Leibenguth. "Ballistic-electron-emission spectroscopy of Au/Si and Au/GaAs interfaces: Low-temperature measurements and ballistic models." Phys. Rev. B **54** (23), 16 972–16 982 (1996).

[41] C. R. Crowell and S. M. Sze. "Electron-phonon collector backscattering in hot electron transistors." Solid-State Electron. **8** (8), 673–& (1965).

[42] J. Simmons. "Generalized formula for the electric tunnel effect between similar electrodes separated by a thin insulating film." J. Appl. Phys. **34** (6), 1793–1803 (1963).

[43] C. B. Duke. *Tunneling in Solids* (Academic Press, New YOrk, 1969).

[44] E. H. Rhoderick and R. H. Williams. *Metal-Semiconductor Contacts* (Clarendon Press, Oxford, 1988).

[45] S. M. Sze. *Physics of Semiconductor Devices* (Wiley, New York, 1981).

[46] M. E. Rubin, G. MedeirosRibeiro, J. J. OShea, M. A. Chin, E. Y. Lee, P. M. Petroff, and V. Narayanamurti. "Imaging and spectroscopy of single InAs self-assembled quantum dots using ballistic electron emission microscopy." Phys. Rev. Lett. **77** (26), 5268–5271 (1996).

[47] A. L. Efros, V. A. Kharchenko, and M. Rosen. "Breaking the phonon bottleneck in nanometer quantum dotsrole of Auger-like processes." Solid State Commun. **93** (4), 281–284 (1995).

[48] J. Blackburn, R. Ellingson, O. Micic, and A. Nozik. "Electron relaxation in colloidal inp quantum dots with photogenerated excitons or chemically injected electrons." J. Phys. Chem. B **107** (1), 102–9 (2003). ISSN 1089-5647.

[49] V. Klimov, S. Hunsche, and H. Kurz. *Colours of Nanometric Gold.* Ph.D. thesis, UCLA (1999).

[50] D. J. Norris and M. G. Bawendi. "Measurement and assignment of the size-dependent optical spectrum in CdSe quantum dots." Phys. Rev. B **53** (24), 16 338–16 346 (1996).

[51] D. J. Norris, A. Sacra, C. B. Murray, and M. G. Bawendi. "Measurement of the size-dependent hole spectrum in CdSe quantum dots." Phys. Rev. Lett. **72** (16), 2612–2615 (1994).

[52] H. Benisty, C. M. Sotomayortorres, and C. Weisbuch. "Intrinsic mechanism for the poor luminescence properties of quantum-box systems." Phys. Rev. B **44** (19), 10 945–10 948 (1991).

[53] U. Woggon, H. Giessen, F. Gindele, O. Wind, B. Fluegel, and N. Peyghambarian. "Ultrafast energy relaxation in quantum dots." Phys. Rev. B **54** (24), 17 681–17 690 (1996).

[54] V. I. Klimov and D. W. McBranch. "Femtosecond high-sensitivity, chirp-free transient absorption spectroscopy using kilohertz lasers." Optics Letters **23** (4), 277–279 (1998).

[55] M. A. Hines and P. Guyot-Sionnest. "Synthesis and characterization of strongly luminescing ZnS-Capped CdSe nanocrystals." J. Phys. Chem. **100** (2), 468–471 (1996).

[56] M. Danek, K. F. Jensen, C. B. Murray, and M. G. Bawendi. "Synthesis of luminescent thin-film CdSe/ZnSe quantum dot composites using CdSe quantum dots passivated with an overlayer of ZnSe." Chem. Mater. **8** (1), 173–180 (1996).

[57] V. M. Kreibig U. *Optical Properties of Metal Clusters* (Berlin, Springer, 1995).

[58] J. A. Creighton, C. G. Blatchford, and M. G. Albrecht. "Plasma resonance enhancement of raman-scattering by pyridine adsorbed on silver or gold sol particles of size comparable to the excitation wavelength." J. Chem. Soc., Faraday Trans. 2 **75**, 790–798 (1979).

[59] G. Mie. Ann Phys **25**, 329 (1908).

[60] M. Brust and C. J. Kiely. "Some recent advances in nanostructure preparation from gold and silver particles: a short topical review." Colloids and Surfaces A-Physicochemical and Engineering Aspects **202** (2-3), 175–186 (2002).

[61] U. Kreibig. "Kramers kronig analysis of optical properties of small silver particles." Zeitschrift Fur Physik **234** (4), 307–& (1970).

[62] U. Kreibig and Vonfrags.C. "Limitation of electron mean free path in small silver particles." Zeitschrift Fur Physik **224** (4), 307–& (1969).

[63] L. Anisimov, B. L. Kapeliovich, and T. L. Perelman. Soviet Phys. JETP **39**, 375 (1975).

[64] C. K. Sun, F. Vallee, L. Acioli, E. P. Ippen, and J. G. Fujimoto. "Femtosecond investigation of electron thermalization in gold." Phys. Rev. B **48** (16), 12 365–12 368 (1993).

[65] C. K. Sun, F. Vallee, L. H. Acioli, E. P. Ippen, and J. G. Fujimoto. "Femtosecond-tunable measurement of electron thermalization in gold." Phys. Rev. B **50** (20), 15 337–15 348 (1994).

[66] S. Link, C. Burda, Z. L. Wang, and M. A. El-Sayed. "Electron dynamics in gold and gold-silver alloy nanoparticles: The influence of a nonequilibrium electron distribution and the size dependence of the electron-phonon relaxation." J. Chem. Phys. **111** (3), 1255–1264 (1999).

[67] T. S. Ahmadi, S. L. Logunov, and M. A. El-Sayed. "Picosecond dynamics of colloidal gold nanoparticles." J. Phys. Chem. **100** (20), 8053–8056 (1996).

[68] Y. Hamanaka, N. Hayashi, A. Nakamura, and S. Omi. "Ultrafast relaxation dynamics of electrons in silver nanocrystals embedded in glass." J. Lumin. **76-7**, 221–225 (1998).

[69] A. Stella, M. Nisoli, S. DeSilvestri, O. Svelto, G. Lanzani, P. Cheyssac, and R. Kofman. "Size effects in the ultrafast electronic dynamics of metallic tin nanoparticles." Phys. Rev. B **53** (23), 15 497–15 500 (1996).

[70] N. Del Fatti, C. Flytzanis, and F. Vallee. "Ultrafast induced electron-surface scattering in a confined metallic system." Appl. Phys. B-Lasers and Optics **68** (3), 433–437 (1999).

[71] B. A. Smith, J. Z. Zhang, U. Giebel, and G. Schmid. "Direct probe of size-dependent electronic relaxation in single-sized Au and nearly monodisperse Pt colloidal nanoparticles." Chem. Phys. Lett. **270** (1-2), 139–144 (1997).

[72] R. H. M. Groeneveld, R. Sprik, and A. Lagendijk. "Femtosecond spectroscopy of electron-electron and electron-phonon energy relaxation in Ag and An." Phys. Rev. B **51** (17), 11 433–11 445 (1995).

[73] J. H. Hodak, A. Henglein, and G. V. Hartland. "Electron-phonon coupling dynamics in very small (between 2 and 8 nm diameter) Au nanoparticles." J. Chem. Phys. **112** (13), 5942–5947 (2000).

[74] M. Nisoli, S. Stagira, S. DeSilvestri, A. Stella, P. Tognini, P. Cheyssac, and R. Kofman. "Ultrafast electronic dynamics in solid and liquid gallium nanoparticles." Phys. Rev. Lett. **78** (18), 3575–3578 (1997).

[75] L. E. Harrell, T. P. Bigioni, W. G. Cullen, R. L. Whetten, and P. N. First. "Scanning tunneling microscopy of passivated au nanocrystals immobilized on Au(111) surface." J. Vac. Sci. Technol. B **17** (6), 2411–2416 (1999).

[76] V. Klimov, P. H. Bolivar, and H. Kurz. "Hot-phonon effects in femtosecond luminescence spectra of electron-hole plasmas in CdS." Phys. Rev. B **52** (7), 4728–4731 (1995).

[77] K. Shum, W. B. Wang, R. R. Alfano, and K. M. Jones. "Observation of the 1p excitonic states in Cd(S,Se)-glass quantum dots." Phys. Rev. Lett. **68** (26), 3904–3907 (1992).

[78] V. Klimov, S. Hunsche, and H. Kurz. "Biexciton effects in femtosecond nonlinear transmission of semiconductor quantum dots." Phys. Rev. B **50** (11), 8110–8113 (1994).

[79] T. Inoshita and H. Sakaki. "Electron relaxation in a quantum dotsignificance of multiphonon processes." Phys. Rev. B **46** (11), 7260–7263 (1992).

[80] P. Landsberg. *Recombinations in Semiconductors* (Cambridge Univ. Press, 1991).

[81] J. L. Pan. "Reduction of the Auger rate in semiconductor quantum dots." Phys. Rev. B **46** (7), 3977–3998 (1992).

[82] V. I. Klimov, A. A. Mikhailovsky, D. W. McBranch, C. A. Leatherdale, and M. G. Bawendi. "Quantization of multiparticle Auger rates in semiconductor quantum dots." Science **287** (5455), 1011–1013 (2000).

[83] S. Hunsche, T. Dekorsy, V. Klimov, and H. Kurz. "Ultrafast dynamics of carrier-induced absorption changes in highly-excited cdse nanocrystals." Appl. Phys. B-Lasers and Optics **62** (1), 3–10 (1996).

[84] P. Guyot-Sionnest and M. A. Hines. "Intraband transitions in semiconductor nanocrystals." Appl. Phys. Lett. **72** (6), 686–688 (1998).

[85] V. I. Klimov. "Optical nonlinearities and ultrafast carrier dynamics in semiconductor nanocrystals." J. Phys. Chem. B **104** (26), 6112–6123 (2000).

VITA

Sameh Dardona was born in Palestine in 1976. He attended Birzeit University in the West Bank for his undergraduate studies and graduated from Birzeit with a major in Physics and a minor in Computer Science in 1998. During his senior year at Birzeit University, Mr. Dardona was awarded a summer research scholarship from The Thomas Jefferson National Accelerator Facility in Newport News, Virginia. In May, 2002, he received his master's degree in Physics from Temple University in Philadelphia, Pennsylvania. While at Temple, Mr. Dardona worked on the growth and optical characterization of MgS:Eu nanoparticles for high density optical data storage application. He then attended The Georgia Institute of Technology where he received his Ph.D. in Physics in August, 2006.